Fermilab

FERMILAB-THESIS-1998-02

Observation of Diffractive W-Boson Production at the Tevatron

A thesis presented to the faculty of

The Rockefeller University

in partial fulfillment of the requirements for

the degree of Doctor of Philosophy

by

Suren Bagdasarov

1997

Observation of Diffractive W-Boson Production at the Tevatron

by
Suren Bagdasarov

Abstract

The first observation of diffractively produced W-bosons in $\bar{p}p$ collisions at $\sqrt{s} = 1.8$ TeV is presented. In a sample of $W \to e\nu$ events collected by the Collider Detector at Fermilab, an excess is found of events with a forward rapidity gap, which is attributed to diffraction. The probability that this excess is consistent with non-diffractive production is 1.1×10^{-4} (3.8σ). The relatively low fraction of $W + Jet$ events observed within this excess implies that mainly quarks from the pomeron, which mediates diffraction, participate in diffractive W production. The diffractive to non-diffractive production ratio is measured to be $R_W = (1.15 \pm 0.55)\%$. From a comparison of diffractive W-boson and dijet production rates the hard-gluon and hard-quark fractions of the pomeron structure are extracted.

Acknowledgements

I would like to take this opportunity to express my gratitude to the entire Rockefeller University Experimental High Energy Physics Group. Especially, I would like to thank my research advisor, Professor Konstantin Goulianos, who entrusted me with this experiment and directed towards its successful completion. I gratefully acknowledge his guidance and assistance in all aspects of the research. I consider myself fortunate for having had the opportunity to meet such colleagues as Giorgio Apollinari, Anwar Bhatti, Tim Cox, Luc Demortier, Nikos Giokaris, David Khazins, Phil Melese, Steve Moulding and Roger Rusack. From working with them I have learned a great deal of experimental physics and professionalism. I have benefitted very much from discussions with Jose Montanha, in particular on the theoretical aspects of Regge phenomenology. My special thanks are due to Kirsten Borras for her extremely careful reading of the manuscript and numerous important corrections, which made this thesis less painful to a reader. I thank my fellow graduate students Alexander Akopian, Arthur Maghakian, Christina Mesropian and Alexey Titov for sharing with me the unforgettable experience of being a graduate student in Big Apple. I am grateful to The Rockefeller University for hospitality and for providing me with the exceptional research opportunity. This thesis would not have been possible also without the dedicated effort of the entire CDF collaboration. All of the people involved have my sincerest thanks.

Finally, my most important acknowledgement is for the love, support and encouragement of my family – my parents, wife and daughter.

Contents

List of Figures

List of Tables

Chapter 1

Introduction

Among the wide variety of interactions involving elementary particles, there is a class of processes, called diffraction dissociation, that play a very important role in fundamental particle dynamics. Approximately 15% of the high energy inelastic $p\bar{p}$ collisions are due to single diffraction dissociation, a process in which one of the incident particles escapes intact with small transverse momentum and a fraction $x_F > 0.9$ of its initial forward momentum. More than 35 years ago a well-defined mathematical formalism, called Regge theory [1], was developed, which describes the general features of single diffraction dissociation and also a variety of other interesting phenomena, such as the shrinking of forward elastic scattering peaks and the rise of total cross sections with energy [2, 3]. Experimental studies have shown that the leading role in diffractive processes is played by the pomeron trajectory, commonly referred to as the *pomeron*, which carries the quantum numbers of the vacuum. Until today no particle has been unambiguously associated with the pomeron trajectory.

Although strong interaction processes with pomeron exchange have been studied for many years, still understanding the pomeron remains one of the big challenges of QCD, the theory of strong interactions. The relation of high energy elastic

and diffractive phenomena to the underlying theory is still not understood. In recent years, interest in this subject has increased significantly. The reason for this interest is connected with ideas which either directly address the problem of the pomeron in QCD or require the understanding of strong-interaction diffractive phenomena as backgrounds for discovery-physics processes involving electroweak boson exchanges [4].

Until recently, the study of diffractive processes was restricted to low momentum transfers, where it was not possible to probe the structure of the pomeron. With higher energies becoming available in accelerators worldwide, it was suggested [7] that it would be valuable to study high momentum transfer diffractive processes, where the interaction takes place on the parton level. Among the questions about the nature of the pomeron that had to be answered were: What is the partonic structure of the pomeron? Does it contain only quarks, or only gluons, or does it consists of both quarks and gluons? How many valence partons does the pomeron have, and is its momentum divided equally between constituent partons or are there leading partons and others that are less energetic? If the pomeron consisted of only two partons that equally share its momentum, it would be expected to have a *hard* structure. Contrary, if the pomeron was made of many partons, then each of the constituent partons would carry a smaller fraction of the pomeron momentum making its structure *soft*. Finally, does the pomeron have a unique partonic structure like real hadrons do, or is it represented by colorless combinations of quark and(or) gluon exchanges between interacting hadrons?

The partonic structure of the pomeron was first investigated by the UA8 experiment [8, 9], which studied diffractive dijet production at the CERN $S\bar{p}pS$ collider at $\sqrt{s} = 630$ GeV, and more recently by the H1 [10, 11] and ZEUS [12, 13] experiments in diffractive deep inelastic scattering (DIS) [10, 11, 12] and dijet pho-

toproduction [13] in ep collisions at $\sqrt{s} \approx 300$ GeV at HERA. All experiments find that a substantial fraction of the pomeron structure is *hard*, i.e. consists of partons carrying a large fraction of the pomeron momentum. From the diffractive DIS experiments, which probe directly the quark component of the pomeron, the hard-quark component is estimated to account for approximately 20-30% of the pomeron momentum.

At the Fermilab Tevatron $\bar{p}p$ collider, a hard-quark pomeron structure would result in detectable diffractive W-boson production [14], which to leading order occurs through the subprocess $q'\bar{q} \to W$. For a hard-gluon dominated pomeron, W production can take place through $qg \to Wq'$, but at a rate lower by order α_s and predominantly in association with a jet.

In this thesis, we present the first observation of diffractive W-boson production in $p\bar{p}$ collisions at $\sqrt{s} = 1.8$ TeV using the Collider Detector at Fermilab (CDF). Chapter 2 contains a brief overview of some theoretical aspects of diffraction, including a model of hard diffraction dissociation in hadron-hadron collisions. Chapter 3 describes the theoretical aspects of diffractive W-boson production and the method of data analysis used in extracting the diffractive W signal from the data. In Chapter 4, components of the Collider Detector at Fermilab are described, paying more attention to those that are relevant to this analysis. Monte Carlo studies of the underlying event distributions, which are important for the calculation of the diffractive acceptance, are presented in Chapter 5. The data collection, trigger requirements, lepton selection criteria, and the central electron W sample are described in Chapter 6. This chapter also describes the details of the procedure used for the extraction of the diffractive W signal, the evaluation of the statistical significance of the observed excess of rapidity gap events, corrections and systematic uncertainties, and the analysis of diffractive W events with jets. In Chapter 7, the final result — the

ratio of diffractive to non-diffractive W-boson production — is discussed and compared with Monte Carlo predictions and with results from other experiments. From a comparison of the diffractive W-boson and dijet production rates, the hard-quark and hard-gluon components of the pomeron structure are evaluated.

Chapter 2

Regge Phenomenology

Diffraction phenomena are well known in classical physics, where they play a fundamental role in the interference of scattered waves. This can be traced to the fact that classical wave functions obey a linear differential equation and therefore satisfy the principle of superposition. In optics the intensity of the light scattered off an absorbing disk, which is a close analogy to an absorbing hadron, as a function of the scattering angle θ is given by

$$\frac{I}{I_0} = \frac{[2J_1(x)]^2}{x} \cong 1 - \frac{r^2}{4}(k\theta)^2 \tag{2.1}$$

where k is the wave number of the photons, r is the radius of the aperture and $x = kr\sin\theta \simeq kr\theta$.

Similar diffraction patterns appear in the quantum mechanical description of interacting particles. In the probabilistic interpretation of quantum mechanics, diffraction is an intrinsic property of the propagation of probability waves and a consequence of the principle of superposition for probability amplitudes. For pp elastic scattering

$$\frac{\mathrm{d}\sigma/\mathrm{d}t}{(\mathrm{d}\sigma/\mathrm{d}t)_{t=0}} = e^{bt} \cong 1 - b(\mathrm{p}\theta)^2, \tag{2.2}$$

where p is the momentum of the incident proton and t is the four-momentum transfer squared. Comparing Eqs. (2.1) and (2.2) we obtain a relation between the radius of interaction and the slope parameter: $b = r^2/4$. For $r = 1/m_\pi$, which is the typical radius of strong interactions, $b = 12.5$ $(\mathrm{GeV/c})^{-2}$. This agrees approximately with the measured values of the slope parameter for pp elastic scattering at high energies [2].

The optical picture of high-energy elastic scattering leads to a semiclassical approach that is very different from the quantum-field treatment used, for instance, in electrodynamics, where the two interacting particles exchange quanta of the field they are coupled to, the photon. In the Yukawa theory of strong interactions, the basic interaction between two colliding hadrons is pion exchange. However, the large coupling constant of strong interactions does not allow the perturbative expansion to be used. The exchange picture is even more complicated by the large number of mesons that can be exchanged. Still, Regge theory [1] provides a relatively simple exchange picture for the description of hadron collisions.

Figure 2.1a is the one-particle exchange Feynman diagram for the two-body inelastic process

$$a + b \longrightarrow c + d \tag{2.3}$$

where the exchanged particle is characterized by internal quantum numbers, such as spin J, isospin I and its third component I_z, strangeness S, and baryon number B. The corresponding diagram for the same process in Regge theory is shown in Figure 2.1b. Regge theory is based on the concept of an exchange of a Regge trajectory between the interacting particles, once a reaction can be characterized as proceeding through the exchange of a particular set of quantum numbers. As is shown in Figure 2.1b, the Regge trajectory transfers four-momentum t and internal quantum numbers I, I_z, S, and B from the upper vertex to the lower vertex. In this respect it

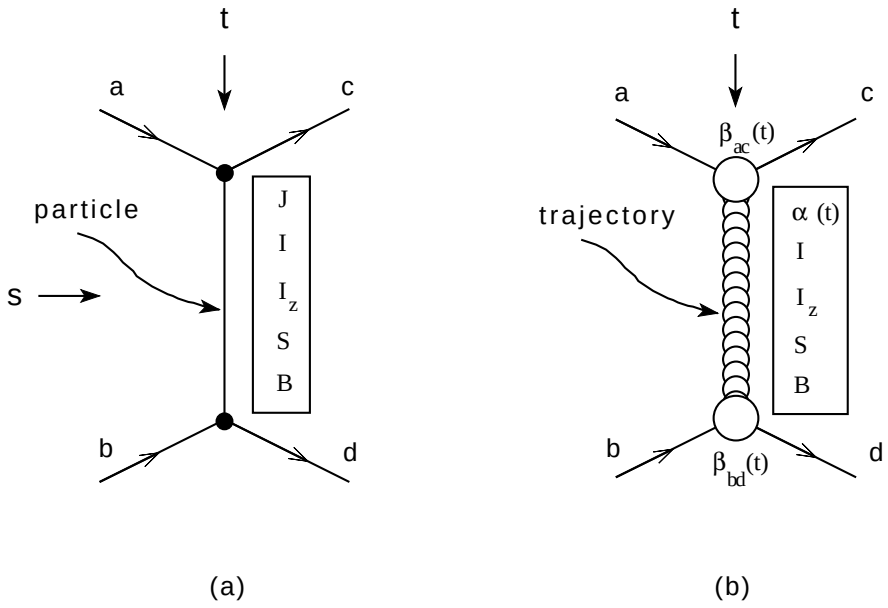

Figure 2.1: *(a) The t-channel one-particle exchange and (b) the t-channel Regge trajectory exchange mechanisms in two-body inelastic reactions.*

acts as a virtual elementary particle with that four-momentum and those quantum numbers. However, the Regge trajectory differs from the virtual particle in that the latter has a fixed intrinsic angular momentum J, while the Regge trajectory does not. The Regge trajectory carries a variable angular momentum $\alpha(t)$. The dependence of α on t defines the Regge trajectory and fixes the spin of the hadrons that lie on it. In this picture, the Lorentz invariant scattering amplitude for the process (2.3) can be described by

$$A(s,t) = \sum_i \beta_i^{ac}(t)\, \beta_i^{bd}(t)\, \eta_i(t)\, \left(\frac{s}{s_0}\right)^{\alpha_i(t)} \tag{2.4}$$

where s is the square of the center of mass energy of the initial hadron states. Each term of the sum relates to the exchange of a Regge trajectory. Thus, by analogy

with one-particle exchange, the term

$$\eta_i(t) \ \left(\frac{s}{s_0}\right)^{\alpha_i(t)} \tag{2.5}$$

corresponds to the propagator of a virtual particle. The spin J and the mass m of the exchanged particles are connected through the relation $J = \alpha(m^2)$ illustrated on the Chew-Frautschi plot in Figure 2.2. It is this trajectory, continued from positive argument (m^2) to negative (t), that fixes the phase and the energy dependence of the amplitude. The factors $\beta_i^{ac}(t)$ and $\beta_i^{bd}(t)$ may be interpreted as coupling constants of the trajectory with the lines describing the transitions $a \to c$ and $b \to d$, respectively. Note that the form of functions $\alpha(t)$, $\beta^{ac}(t)$, and $\beta^{bd}(t)$ is not fixed by Regge theory and must be determined experimentally. The function $\eta(t)$ is called the signature factor. It has the form

$$\eta(t) = \frac{\tau + e^{-i\pi\alpha(t)}}{\sin \pi\alpha(t)} \tag{2.6}$$

and brings in the amplitude poles due to the vanishing of the denominator for even (odd) integer values of $\alpha(t)$ according to the value $+1$ or (-1) taken by the signature τ. This effect of the signature factor is consistent with field theory, where the exchange of a particle gives rise to a pole in the amplitude. The scale parameter s_0 in Eqn. (2.4) is introduced for dimensional convenience and is usually set to 1 GeV^2, the hadron mass scale.

Experiment finds that the trajectories $\alpha(t)$ appear, at least roughly, to be linear in t, and that for the meson families of ρ, ω, f and a, the trajectories coincide within errors, as illustrated in Figure 2.2. Parameterization of the meson trajectories by the form $\alpha(t) = \alpha_0 + \alpha' t$ gives $\alpha_0 \approx 0.5$ and $\alpha' \approx 0.9$ GeV^{-2}.

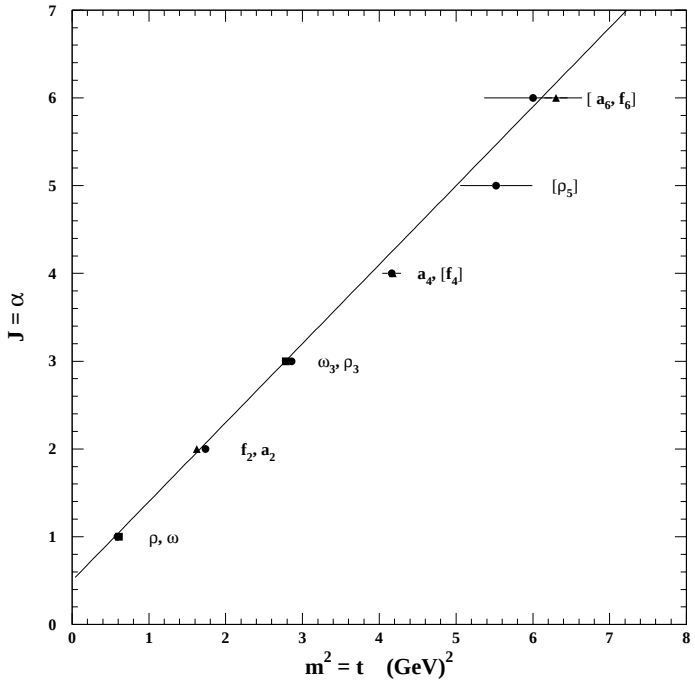

Figure 2.2: *The ρ, ω, f and a trajectories.*

2.1 Total Cross Section and Elastic Diffraction

From the optical theorem, the total cross section ($ab \to$ anything) is related to the imaginary part of the forward elastic ($ab \to ab$) amplitude by

$$\sigma_{\rm T} = \frac{1}{s}\,{\rm Im}\,A_{ab\to ab}(s, t=0) \tag{2.7}$$

Using Eqn. (2.4), the total cross section becomes

$$\sigma_T = \beta_{I\!P}^{aa}(0)\,\beta_{I\!P}^{bb}(0)\,{\rm Im}|\eta_{I\!P}(0)|\left(\frac{s}{s_0}\right)^{\alpha_{I\!P}(0)-1} + \sum_i \beta_i^{aa}(0)\,\beta_i^{bb}(0)\,{\rm Im}|\eta_i(0)|\left(\frac{s}{s_0}\right)^{\alpha_i(0)-1} \tag{2.8}$$

where the sum represents the contribution of the meson trajectories. For ρ, ω, f, a exchanges $\alpha(0) \approx 0.5$ (see Figure 2.2), so that these exchanges contribute approximately the power of $1/\sqrt{s}$. The first term was introduced when it was found experimentally that the total cross section appeared to level off at high energies. A

constant cross section could be obtained with $\alpha_{I\!P}(0) = 1$. This contribution is by construction the same for particle and antiparticle scattering off the same target (it is even under C conjugation). Hence, it satisfies the Pomeranchuk theorem, which states that the cross section of a particle and antiparticle off the same target are asymptotically equal. For this reason, the trajectory with the intercept $\alpha(0) = 1$ is called the *pomeron* ($I\!P$) trajectory.

When total cross sections were measured at still higher energies, it was found that they actually rise with s (see Figure 2.3). In order to give a slowly-increasing contribution to $\sigma_{\rm T}$, the pomeron trajectory must be such that $\alpha_{I\!P}(0) = 1 + \epsilon$, where ϵ is a small number. If one parameterizes the pomeron trajectory as

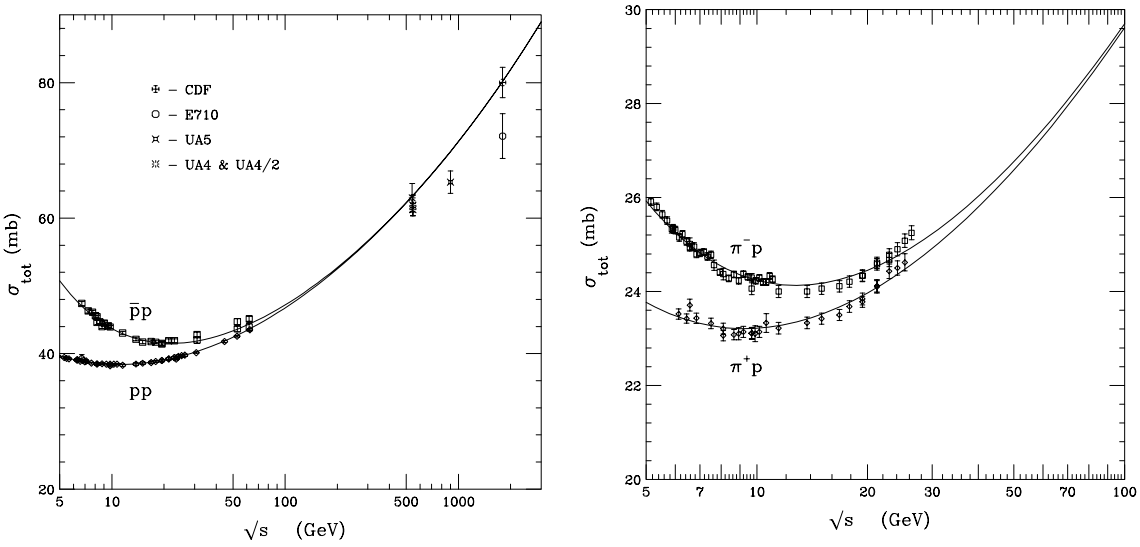

Figure 2.3: *Total cross section for $p^{\pm}p$ and $\pi^{\pm}p$ collisions.*

$$\alpha_{I\!P}(t) = 1 + \epsilon + \alpha' \, t$$

where α' is the slope of the pomeron trajectory determined experimentally from elastic scattering, the total $\bar{p}p$ cross section at high energies becomes

$$\sigma_{\rm T}^{\bar{p}p} = \beta_{I\!P}^{pp}(0) \, \beta_{I\!P}^{\bar{p}\bar{p}}(0) \left(\frac{s}{s_0}\right)^{\epsilon} = \sigma_0^{\bar{p}p} \left(\frac{s}{s_0}\right)^{\epsilon} \tag{2.9}$$

and the differential elastic cross section is given by

$$\frac{d\sigma_{\rm el}^{\bar{p}p}}{dt} = \frac{1}{16\pi s^2}\,|A(s,t)|^2 = \frac{1}{16\pi}\left[\beta_{I\!P}^{pp}(t)\,\beta_{I\!P}^{\bar{p}\bar{p}}(t)\right]^2\left(\frac{s}{s_0}\right)^{2[\alpha_{I\!P}(t)-1]} = \frac{\left(\sigma_{\rm T}^{\bar{p}p}\right)^2}{16\pi}\left(\frac{s}{s_0}\right)^{2\alpha' t}F^4(t) \tag{2.10}$$

where $F(t)$ is the nucleon form factor.

The most recently determined value of ϵ, obtained from a global fit to $p^{\pm}p$, $\pi^{\pm}p$ and $K^{\pm}p$ total cross sections [5], is $\epsilon = 0.104 \pm 0.002$. The value of α' obtained from elastic scattering data is $\alpha' \approx 0.25$ GeV^{-2}.

In the small-t region, the t-dependence of elastic scattering is represented well by $F^4(t) \approx e^{b_{0,\rm el}t}$. This gives

$$\frac{{\rm d}\sigma_{\rm el}}{{\rm d}t} \approx \frac{\left(\sigma_{\rm T}^{\bar{p}p}\right)^2}{16\pi}\,e^{b_{\rm el}(s)t} \tag{2.11}$$

where $b_{\rm el}(s) = b_{0,\rm el} + 2\alpha'\ln(s/s_0)$. However, this simple exponential dependence underestimates the cross section at large t. In the fits of Figure 2.3, the ratio of the strengths of pomeron exchange in $\pi^{\pm}p$ and $p^{\pm}p$ scattering is $10.83/16.79 \approx 2/3$. This suggests that the pomeron couples to single valence quarks in a hadron, like an isoscalar photon [15]. Hence, it was suggested [15] that the appropriate form factor for elastic and diffractive scattering is the isoscalar form factor measured in electron-nucleon scattering

$$F_1(t) = \frac{4m^2 - 2.8t}{4m^2 - t}\left[\frac{1}{1 - t/0.7}\right]^2, \tag{2.12}$$

where m is the proton mass.

2.2 Inelastic Diffraction

Let us consider the process

$$p + \bar{p} \to p + X \tag{2.13}$$

where X denotes "anything". In a diffractive event the incident proton goes through the collision nearly unchanged; it is quasi-elastically scattered with a small momentum transfer squared, $t = (P_1 - P_3)^2$, and a fraction $x_F = 2p_{3L}/\sqrt{s}$ of its initial momentum, p_0, while the antiproton dissociates into a multi-particle hadronic state X of mass M_X, as depicted in Figure 2.4. P_1 and P_3 denote here the four-momenta of the incident and scattered proton, respectively; p_{3L} is the longitudinal momentum of the outgoing proton; and $s = (P_1 + P_2)^2$ is the square of the center of mass energy of the initial $\bar{p}p$ system. Diffractive processes can be rather well tagged by their

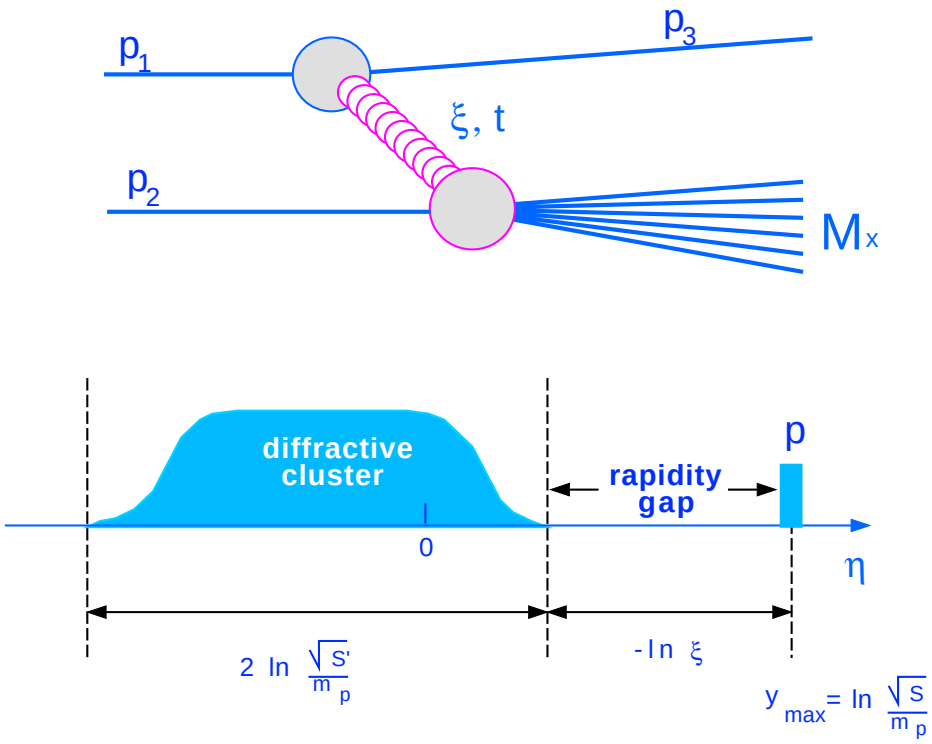

Figure 2.4: *Diffractive kinematics.*

specific kinematical configurations. For $|t| \ll M_X^2$, which is the case considered here,

the mass M_X is related to the Feynman scaling variable x_F of the recoil proton by $\xi = M_X^2/s \simeq 1 - x_F$. As a result of the interaction, a specific rapidity configuration is obtained. The rapidity y of a particle produced in a high-energy collision is defined as

$$y = \frac{1}{2} \ln \frac{E + p_L}{E - p_L}, \tag{2.14}$$

where E is the total energy of the particle. For relativistic particles

$$y \approx \ln[(p + p_L)/(p - p_L)]/2 \simeq -\ln \tan(\theta/2),$$

where θ is the polar angle of a particle with respect to the direction of the incident proton. This last quantity, named "pseudorapidity", is usually denoted by η. We will use rapidity and pseudorapidity interchangeably throughout this analysis.

In the process (2.13) the rapidity distribution of the final-state particles exhibits a gap (absence of particles) between the rapidity of the quasi-elastically scattered proton and the rapidities of all other particles. This situation is very different from what is known for a typical multi-particle configuration, with the full rapidity interval nearly uniformly populated. A quasi-elastically scattered proton imposes such a rapidity gap. Due to the kinematics of the process, the secondaries resulting from the dissociation of the antiproton into a system X appear on the rapidity plot in Figure 2.4 as a cluster centered at $y \approx \ln(1/\xi)/2$. The overall rapidity difference between the center of the cluster and the quasi-elastically scattered proton is $\ln(s/M_X m_p)$, and the width of the rapidity gap is given by $-\ln(\xi)$.

2.3 Diffraction Dissociation Cross Section

We can now extend the formalism described in section 2.1 to inelastic diffractive scattering. The pseudo two-body amplitude for the process (2.13) is shown

in Figure 2.5a. Assuming s large, ξ small and $t \ll s$, the process can be represented [6] by the exchange of a Regge pole $\alpha(t)$ in the t channel (Figure 2.5b). Here $\alpha(t)$ refers to the dominating pomeron trajectory. The inelastic diffractive cross section is

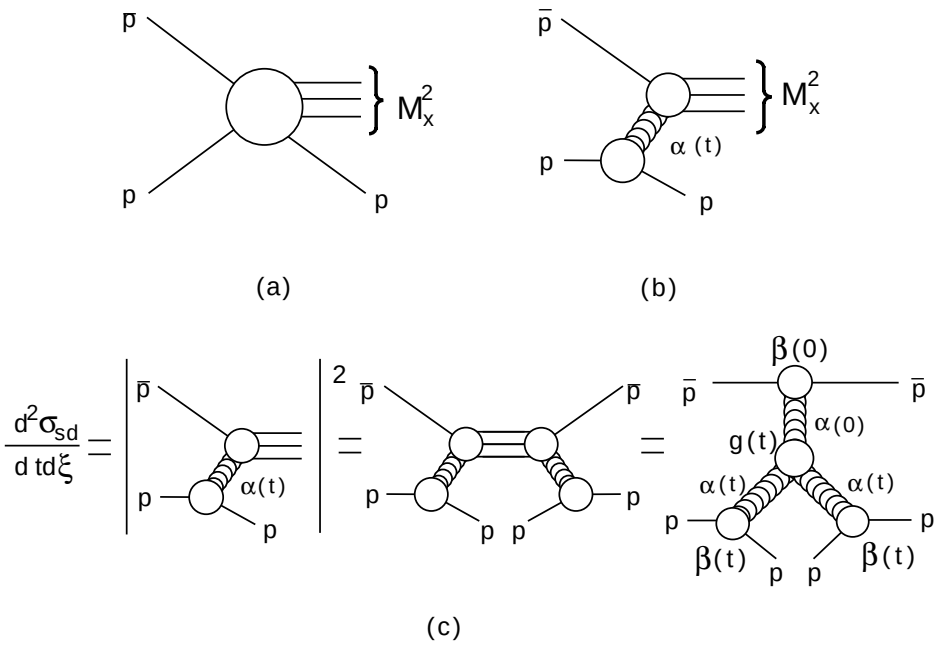

Figure 2.5: *(a) Pseudo two-body amplitude of inelastic diffraction. (b) Regge approximation of the amplitude for large s, small ξ, and $t \ll s$. (c) Triple Regge diagram of differential single diffraction cross section.*

obtained by squaring the amplitude diagram in Figure 2.5b. Figure 2.5c represents pictorially the derivation of the Triple Regge diagram responsible for the process of single diffraction dissociation. The differential single diffraction $\bar{p}p$ cross section is given by

$$\frac{\mathrm{d}^2\sigma_{\mathrm{sd}}^{p\bar{p}}}{\mathrm{d}t\mathrm{d}\xi} = \frac{\beta_1^2(t)}{16\pi}\,\xi^{1-2\alpha(t)}\left[\beta_2(0)g(t)\left(\frac{\hat{s}}{\hat{s}_0}\right)^{\alpha(0)-1}\right] \tag{2.15}$$

where the subscripts 1 and 2 refer to p and $\bar{p}$, $g(t)$ is the triple-pomeron coupling, $\hat{s} = \xi s$ the squared center of mass energy in the $I\!P\bar{p}$ reference frame, and $\hat{s}_0$ is the constant determining the energy scale.

For $\xi \approx 0.1$, one must add for the process (2.13) a contribution from the Reggeon trajectory $(\rho, \omega, \ldots)$, and even from the pion trajectory. These exchanges can also result in large rapidity gaps, although, as they correspond to smaller powers of $1/\xi$ than pomeron exchange, they become relatively less important as ξ decreases.

2.4 The Pomeron Flux Factor

The pomeron exchange amplitude is proportional to the product of the coupling constants at each vertex $(\beta_{I\!P}^{aa} \cdot \beta_{I\!P}^{bb})$. This factorization hypothesis leads to scaling relations between diffraction dissociation, elastic scattering and total cross section. For example, the ratio of diffraction dissociation to elastic scattering is expected to be a constant independent of the target particle. Experiment has shown that in "soft diffraction" processes the ratio of the differential cross section for $p+a \to X + a$ to that for $p + a \to p + a$, where a denotes a proton or a deutron, does not depend on a [2]. The factorization property makes pomeron exchange look like particle exchange, and therefore in (2.15) the term in the square brackets is interpreted as the $I\!P\bar{p}$ total cross section. Then, the differential single diffraction cross section becomes

$$\frac{\mathrm{d}^2\sigma_{\mathrm{sd}}^{p\bar{p}}}{\mathrm{d}t\mathrm{d}\xi} = f_{I\!P/p}(\xi, t)\ \sigma_T^{I\!P\bar{p}}(\hat{s}, t) \tag{2.16}$$

This interpretation allows to consider the single diffraction cross section as a process in which pomerons "carried" by the proton interact with the antiproton. A so-called pomeron flux factor is defined as

$$f_{I\!P/p}(\xi, t) = \frac{\mathrm{d}^2\sigma_{\mathrm{sd}}/\mathrm{d}\xi\mathrm{d}t}{\sigma_T^{I\!P\bar{p}}(\hat{s}, t)} = \frac{\beta_1^2(t)}{16\pi}\xi^{1-2\alpha(t)} = K\ \xi^{1-2\alpha(t)}\ [F_1(t)]^2, \tag{2.17}$$

where $K = \sigma_0^{p\bar{p}}/16\pi$ is a constant.

For the numerical evaluation of the pomeron flux factor, we use the param-

eterization of the pomeron trajectory obtained from the CDF results [17, 18, 19]:

$$\alpha_{I\!P}(t) = 1 + \epsilon + \alpha' t = 1 + 0.115 + 0.26\ t \tag{2.18}$$

Using the value (80.03 ± 2.24) mb for the $p\bar{p}$ total cross section at $\sqrt{s} = 1800$ GeV measured in CDF, we obtain $K = 0.73$ GeV^{-2}.

2.5 Hard Diffraction

According to Regge theory, high-energy, small-t processes are believed to be controlled by single-pomeron exchange [2]. While this approach is phenomenologically successful, there is not yet real understanding of what the pomeron is, i.e. how it is generated within the fundamental quantum field theory of the strong interaction.

In QCD, interactions between hadrons arise through the interactions of their quark and gluon components. Quarks and gluons experience and transmit strong forces. It is known that the strong interactions of quarks and gluons occur due to the quantum characteristic called *color* (also known as "strong charge") carried by them. Only colored particles can emit or absorb a gluon. Because of color, the strong forces transmitted by gluons differ significantly from the electromagnetic forces transmitted by photons. For example, gluons can couple directly to other gluons whereas photons cannot couple to each other. A fundamental aspect of QCD is asymptotic freedom. This feature accounts for the tendency of hadrons to behave like collections of pointlike constituents, also called *partons*, when probed at short distances, and determines the applicability of the perturbation expansion formalism in the calculation of observables in parton-parton scattering. The most crucial consequence of strong forces is color confinement, which means that neither quarks nor gluons can appear in isolation. They can only exist within colorless (color-neutral)

composite hadrons. The three quark (*baryons*) and quark-antiquark (*mesons*) colorless configurations made of six different types (*flavors*) of quarks, also called *valence* quarks, form the existing variety of hadrons with their unique quantum numbers. In addition, a fluctuating cloud (or *sea*) of virtual gluons and neutral $q\bar{q}$ pairs is present in each hadron. This sea does not affect the hadron's quantum numbers but can play an important role in high energy collisions.

Since diffractive processes involve a strong interaction, it is natural to ask whether the pomeron can be understood as an object composed of partons. Hadron interactions proceeding through the exchange of a particular combination of quarks and gluons that preserve the quantum numbers of the initial hadron states lead to either elastic scattering of the initial hadrons, or to diffraction dissociation of one (single diffraction dissociation) or both (double diffraction dissociation) hadrons in the final state into multi-hadron system(s). In QCD, such a combination of quarks and gluons would be a colorless construct which has the quantum numbers of the QCD vacuum and which does not radiate as it separates in space from the parent hadron, leading to events with a rapidity gap. Such a hypothetical parton state in QCD could be associated with the pomeron. Colorless configurations can also be made out of gluons alone. QCD studies suggest that such hadrons (*glueballs*) may exist [20], but none have yet been conclusively identified.

Until recently, there has not been much overlap between Regge theory and perturbative QCD. Diffraction, which is intimately connected with confinement, since it displays the basic property of hadrons behaving as objects of finite size and definite quantum numbers, is concentrated at small momentum transfers and appears as a large distance phenomenon, dominated by non-perturbative effects. Hence, it is not calculable by perturbative QCD. There are, however, perturbative models in which the pomeron is considered as a colorless two-gluon bound state [21, 22, 23]. Such

models are used to calculate hard processes associated with diffraction.

A suggestion was made [7] to probe the exchanged pomeron (or pomeron-like object) in a hard scattering process. If the pomeron had a partonic structure it should manifest itself in high-mass diffractive scattering through the appearance of jets, or heavy quarks [24], or W and Z-bosons [14]. An approach in calculating the cross section for such process is based on extending the concept of factorization of the diffractive cross section in "soft diffraction" processes, described in section 2.4, to hard pomeron-hadron collisions by treating the pomeron flux factor as a flux of particle-like pomerons with a unique partonic structure. In this model the diffraction dissociation process proceeds in two steps. In the first step, a pomeron is emitted from the (anti)proton at the upper vertex in Figure 2.4 with a small squared momentum transfer, and with a forward momentum fraction ξ smaller than ~ 0.1. The upper bound for ξ follows from the condition for coherence in diffractive processes [2]. In the second step, this pomeron interacts with the proton in a large momentum transfer process between the constituent partons. In the analysis presented here this approach is used for the simulation of diffractive W-boson production.

Chapter 3

Diffractive W-boson Production

At Tevatron energies, a hard-quark pomeron structure of the type

$$\beta Q(\beta) \sim \beta(1-\beta), \tag{3.1}$$

where β is the fraction of the pomeron momentum carried by the scattered parton, could result in detectable diffractive W production [14], which to leading order occurs through the subprocess $q'\bar{q} \to W$. The diagram for the process $p + \bar{p} \to p + W + X$ is shown in Figure 3.1. Assuming factorization, the diffractive W-boson production cross section is given by

$$\sigma_W = \sum_{a,b} \int_{\xi^{\min}}^{\xi^{\max}} d\xi \int_{x_b^{\min}}^{1} dx_b f_{I\!P/p}(\xi) f_{I\!P}(x_b) f_{a/\bar{p}}(x_a) |V_{ab}|^2 \frac{1}{x_b \xi s} \left[\sqrt{2}\frac{\pi}{3} G_F M_W^2\right], \tag{3.2}$$

where $x_b \equiv \beta$ is the momentum fraction of the parton in the pomeron, $x_a = M_W^2/x_b\xi s$ is the momentum fraction of the parton in the antiproton, M_W is the W-boson mass, G_F is the Fermi constant, and V_{ab} is the relevant Cabibbo-Kobayashi-Maskawa matrix element. The minimum value of x_b is determined as $x_b^{\min} = M_W^2/\xi s$. The factorization scale is set to the W-boson mass and the scale dependence is suppressed.

In W events only an $e^{\pm}$ from $W^{\pm} \to e^{\pm}\nu$ is registered and available for the analysis, while the neutrino is not detected. Therefore, it is useful to consider

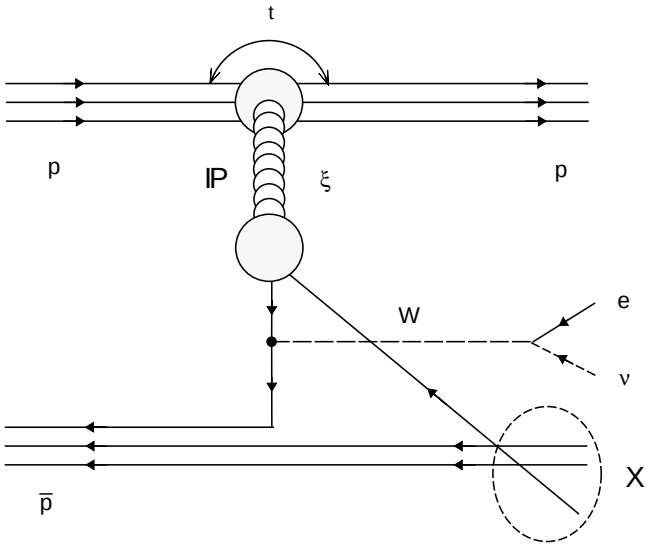

Figure 3.1: *Diagram of diffractive W-boson production assuming a hard-quark pomeron structure.*

distributions of the observed charged lepton. At lowest order (see Figure 3.1) there is no gluon contribution. For the specific process $p + \bar{p} \rightarrow p + (W^- \rightarrow e^- \tilde{\nu}) + X$, using the narrow width approximation, we have

$$\frac{d\hat{\sigma}^l_{ab}}{d\hat{t}} \simeq \frac{G_F^2}{6M_{W}\,,\,{}_{W}} |V_{ab}|^2\, \delta(x_a x_b s - M_W^2)\hat{u}^2, \tag{3.3}$$

where $\hat{t} = (P_a - P_{e^-})^2$, , ${}_W$ is the width of the W-boson, and $\hat{u}$ is given by

$$\hat{u} = -x_b \xi \sqrt{s} E_T\, e^{-y}.$$

The rapidity y is defined as

$$y = \frac{1}{2} \ln \left(\frac{x_a}{x_b \xi} \right) + \hat{y},$$

with

$$\hat{y} = -\ln \tan(\hat{\theta}/2),$$

where $\hat{\theta}$ is the c.m. scattering angle in the $(e^- \tilde{\nu})$ rest frame.

The differential electron cross section is given by

$$\frac{d\sigma^l}{dy} = \sum_{a,b} \int_{\xi^{\min}}^{\xi^{\max}} \frac{d\xi}{\xi} \int_{E_T^{\min}}^{E_T^{\max}} dE_T f_{I\!P/p}(\xi) f_{I\!P}(x_b) f_{a/\bar{p}}(x_a) |V_{ab}|^2 \left[\frac{\hat{u}^2 G_F^2}{6s,\, _W [(M_W/2E_T)^2 - 1]^{1/2}} \right], \tag{3.4}$$

where x_a and x_b are now given by

$$\begin{aligned} x_a &= \frac{M_W\, e^{-y}}{\sqrt{s}} \left[\frac{M_W}{2E_T} + \sqrt{\left(\frac{M_W}{2E_T}\right)^2 - 1} \right], \\ x_b &= \frac{M_W^2}{s} \frac{1}{x_a \xi} \end{aligned} \tag{3.5}$$

A similar expression holds for W^+ production.

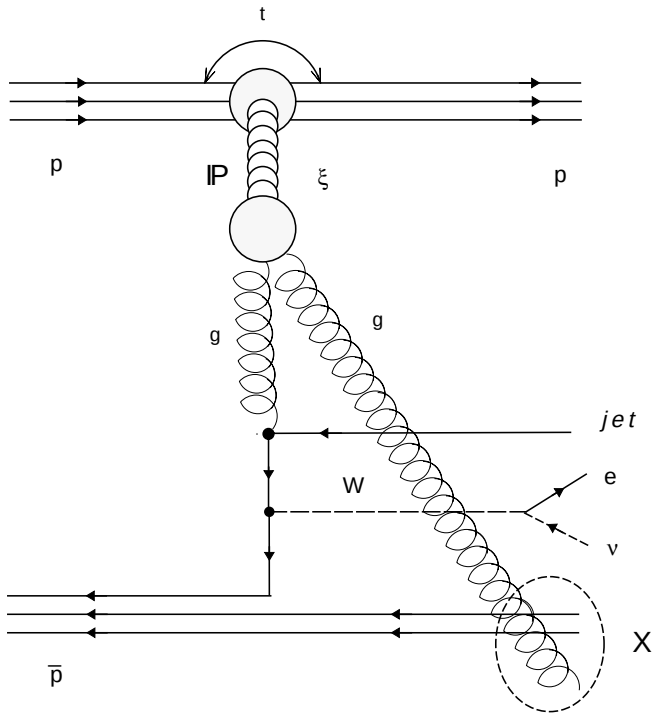

Figure 3.2: *Diagram of diffractive W-boson production assuming a hard-gluon pomeron structure.*

For a hard-gluon dominated pomeron with a parton density of the form

(3.1), W production can occur through $qg \rightarrow Wq'$, but at a rate lower by order α_s and always in association with a jet (Figure 3.2).

The cross sections for producing diffractive W-bosons with a soft-quark or a soft-gluon pomeron structure are expected to be significantly smaller. Taking into account previous experimental results revealing a hard parton content in the pomeron [9, 10, 12], only hard-quark and hard-gluon structures for the pomeron are considered in this analysis.

3.1 Analysis Method

3.1.1 Correlations and Asymmetries

Rapidity gaps appear naturally in diffractive W events, but at the $\sim 1\%$ level are also present in non-diffractive (ND) W events from fluctuations in the underlying event multiplicity (Figure 3.3). Therefore, a sample of events with a rapidity gap is expected to contain a mixture of diffractive and non-diffractive events. In order to separate the diffractive signal from the non-diffractive background in the sample of W events with a rapidity gap, we use the following expected characteristic features of diffractive W events: angle-gap, charge-gap, and angle$\otimes$charge correlations.

Angle-gap correlation From the kinematics of single diffraction dissociation, in a diffractive $W^{\pm} \rightarrow e^{\pm}\nu$ event produced in a $\bar{p}$ collision with a pomeron emitted by the proton (see Figure 3.3), the rapidity gap is expected to be at positive η (p-direction) and the electron, or the positron, boosted towards negative η, creating a correlation between the angle of the electron(positron) and the sign of the rapidity gap. These events, for which the relationship $\eta_e \times \eta_{\rm gap} < 0$ is satisfied, are named angle-gap correlated, in contrast to angle-gap anticorrelated events with $\eta_e \times \eta_{\rm gap} > 0$. This

gap-angle correlation is a consequence of the kinematics of the hard process and is expected to be modeled well by Monte Carlo simulations.

Charge-gap correlation Because of the low c.m. energy of the pomeron-$\bar{p}$ collision and large W-boson mass, mainly valence quarks from the $\bar{p}$ participate in producing the W. Since the pomeron is quark-flavor symmetric, while the $\bar{p}$ has two $\bar{u}$ and one $\bar{d}$ quarks, approximately twice as many electrons as positrons are expected (charge-gap correlation). Thus, events in which the electron(positron) charge, C_e, and pseudorapidity of the gap, $\eta_{\rm gap}$, satisfy the relationship $C_e \times \eta_{\rm gap} < 0$ are classified as charge-gap correlated, in contrast to charge-gap anticorrelated events for which $C_e \times \eta_{\rm gap} > 0$. These correlations can be seen in the Monte Carlo generated distributions of Figure 3.3. The opposite correlations are, of course, expected for $p - I\!P$ collisions with the pomeron emitted by the $\bar{p}$.

Angle⊗Charge correlation For diffractive events with $\eta_e \times C_e > 0$ there is a higher probability that the rapidity gap is on the side satisfying $\eta_e \times \eta_{\rm gap} < 0$. We call these events (angle⊗charge)-correlated, and the ones with $\eta_e \times \eta_{\rm gap} > 0$ (angle⊗charge)-anticorrelated. A sample of doubly correlated and anticorrelated W events is more sensitive to the diffractive signal, and therefore we use these events in this analysis for measuring the ratio of diffractive to non-diffractive W-boson production.

3.1.2 Asymmetry Analysis

The expected asymmetry between the numbers of correlated and anticorrelated diffractive W events is used as an analyzer to determine the fraction of diffractive events from the corresponding asymmetry observed in the data sample.

The asymmetry, A, between the numbers of correlated and anticorrelated rapidity gap events is given by

$$A = \frac{N^{\rm c}_{\rm gap} - N^{\overline{\rm c}}_{\rm gap}}{N^{\rm c}_{\rm gap} + N^{\overline{\rm c}}_{\rm gap}}, \tag{3.6}$$

where $N^{\rm c}_{\rm gap}$ and $N^{\overline{\rm c}}_{\rm gap}$ are the numbers of correlated and anticorrelated rapidity gap events, respectively. Then, the fraction F_D of diffractive W events in the sample of events with a rapidity gap is determined by

$$F_D = \frac{A_{\rm data} - A^{MC}_{ND}}{A^{MC}_{D} - A^{MC}_{ND}}, \tag{3.7}$$

where $A_{\rm data}$ is the measured asymmetry in the data sample, and A^{MC}_{D} (A^{MC}_{ND}) is the expected asymmetry for diffractive (non-diffractive) events obtained from Monte Carlo simulations. In non-diffractive W events, where rapidity gaps arise from fluctuations in the particle multiplicity, Monte Carlo simulations show that there are no significant angle-gap or charge-gap correlations ($A^{MC}_{ND} \approx 0$). Hence, the fraction of diffractive events in the data sample of correlated and anticorrelated W events is determined just by the ratio of the measured asymmetry, $A_{\rm data}$, and the expected asymmetry, A^{MC}_{D}, for diffractive W events:

$$F_D = \frac{A_{\rm data}}{A^{MC}_{D}}. \tag{3.8}$$

Multiplying the fraction F_D by the total number of correlated and anticorrelated rapidity gap W events in the data sample, yields the number of diffractive W events with a gap:

$$N^{\rm gap}_{D} = F_D \cdot (N^{\rm c}_{\rm gap} + N^{\overline{\rm c}}_{\rm gap}) \tag{3.9}$$

Dividing this number by the total number of W events in the sample, N_W, and correcting for acceptances, one obtains the ratio of diffractive to non-diffractive W production

$$R = \frac{N^{\rm gap}_{D}/(a^{\rm gap}_{D} \cdot f^{\rm ce}_{D})}{N_W / f^{\rm ce}_{ND}}, \tag{3.10}$$

where $a_D^{\rm gap}$ is the gap acceptance for correlated and anticorrelated diffractive W events, and $f_D^{\rm ce}$ ($f_{ND}^{\rm ce}$) is the fraction of diffractive (non-diffractive) W events with a central electron or positron.

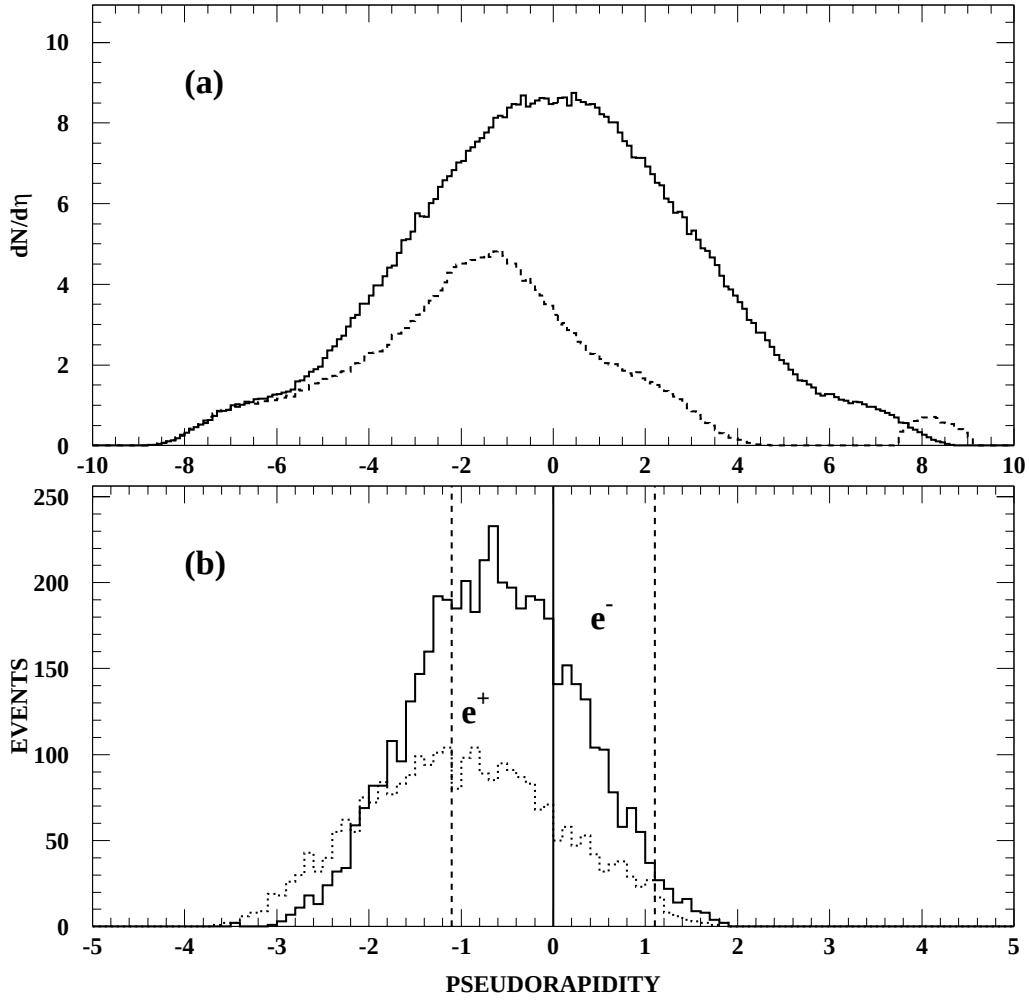

Figure 3.3: *Monte Carlo generated $dn/d\eta$ distributions: (a) particle densities for non-diffractive (solid) and for diffractive (dashed) W events for pomerons of beam momentum fraction $\xi = 0.03$ emitted by protons (at positive η); (b) electrons and positrons from diffractive $W^{\pm} \rightarrow (e^{\pm}\nu)$ events for all pomerons of $\xi < 0.1$ emitted by protons (the vertical dashed lines define the boundaries of the region of the $e^{\pm}$ measurement in this analysis).*

Chapter 4

Accelerator and Detector

4.1 The Tevatron Collider

The main experimental facility at the Fermi National Accelerator Laboratory (Fermilab), is the Tevatron — currently the world's most powerful particle collider. It is a superconducting synchrocyclotron, which accelerates protons and antiprotons in opposite directions and brings them into head-on collisions (Figure 4.1). The Tevatron is the last stage of an acceleration chain that involves several individual accelerators.

The Cockcroft-Walton electrostatic accelerator provides the first stage of acceleration. Inside this device, electrons are added to hydrogen atoms. The resulting negative ions, each consisting of two electrons and one proton, are attracted to a positive voltage and accelerated to an energy of 750 KeV. After leaving the Cockcroft-Walton, negative hydrogen ions enter a linear accelerator called the Linac, which is approximately 500 feet long. The linear accelerator increases the energy of the negative hydrogen ions from 750 KeV to 400 MeV before injecting them into the Booster accelerator. Before entering the Booster, the ions pass through a carbon

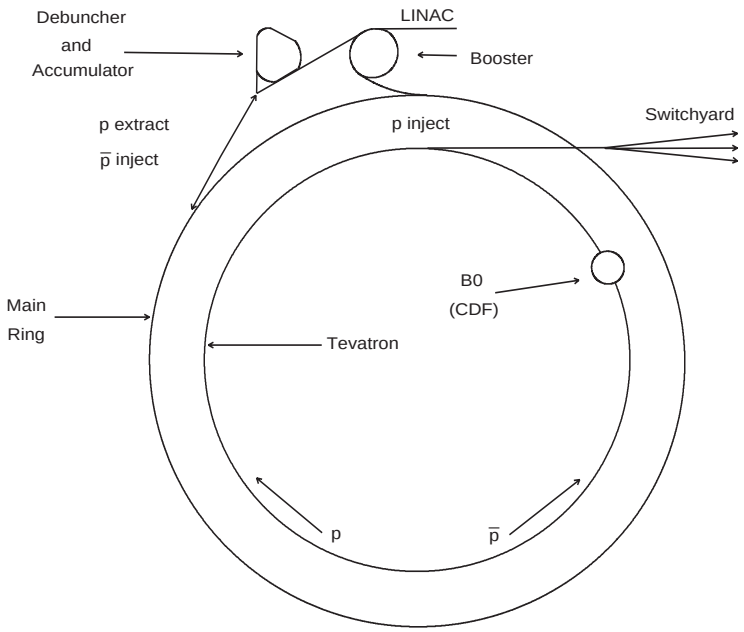

Figure 4.1: *Schematic view of the Fermilab $\bar{p}p$ collider.*

foil which removes the electrons, leaving only the protons. Located nearly 20 feet below ground, the Booster is a rapid cycling synchrotron 500 feet in diameter. The protons travel around the Booster about 20,000 times and their energy is raised to 8 GeV. The Booster normally cycles twelve times in rapid succession, loading twelve pulses, or bunches, of roughly 10^{11} protons, into the Main Ring, the next stage of the acceleration process. The Main Ring is another proton synchrotron, which is four miles in circumference, that uses conventional magnets and can achieve a maximum energy of 400 GeV per beam particle. Under current operating modes, the Main Ring accelerates protons to 150 GeV and is used to boost protons for the Tevatron, and also to provide primary protons to the antiproton source. To produce antiprotons, the protons are accelerated to 120 GeV in the Main Ring, and then directed onto a beryllium fixed target, producing approximately 10^7 antiprotons per bunch. These are selected and transported to the Debuncher Ring where the cross

section of the antiproton beam is reduced in size by a process known as stochastic cooling. Subsequently, they are transferred to the Accumulator ring for storage. Finally, when $\sim 10^{10}$ antiprotons have been produced, they are reinjected into the Main Ring and after acceleration up to 150 GeV they are injected into the Tevatron, where they are accelerated simultaneously with a counterrotating beam of protons to an energy of nearly 1 TeV. Quadrupole magnets are used in order to focus the beams at the B0 collision hall. At the B0 collision point, where the CDF detector is placed, the beams are approximately circular in cross section with a radius of 45μm at 1 σ. Longitudinally, the beam bunches have roughly Gaussian shape with a width of $\pm$30 cm.

The number of collisions per second, N, is given by

$$N = \sigma \cdot L, \tag{4.1}$$

where σ is the cross section of the colliding particles and L is the luminosity. To maximize N, the luminosity, which is given by

$$L = \frac{N_p \cdot N_{\bar{p}} \cdot f}{4\pi\sigma^2} \tag{4.2}$$

is made as large as possible. Here N_p and $N_{\bar{p}}$ are the number of protons and antiprotons per bunch, respectively, f is the frequency of the bunch crossings, and σ is the r.m.s. width of the beam transverse profile at the interaction point. Focusing the beams with quadrupole magnets results in an increase of the luminosity.

4.2 The CDF Detector

The Collider Detector at Fermilab (CDF) is the first general purpose detector built at the Tevatron to study 2 TeV $\bar{p}p$ collisions. Event analysis in CDF

is based on charged particle tracking, magnetic momentum analysis and charge determination, and measurement of the particle position and energy deposition in a calorimeter. The detector features approximate cylindrical symmetry. A perspective view and a schematic side view of CDF are shown in Figures 4.2 and 4.3.

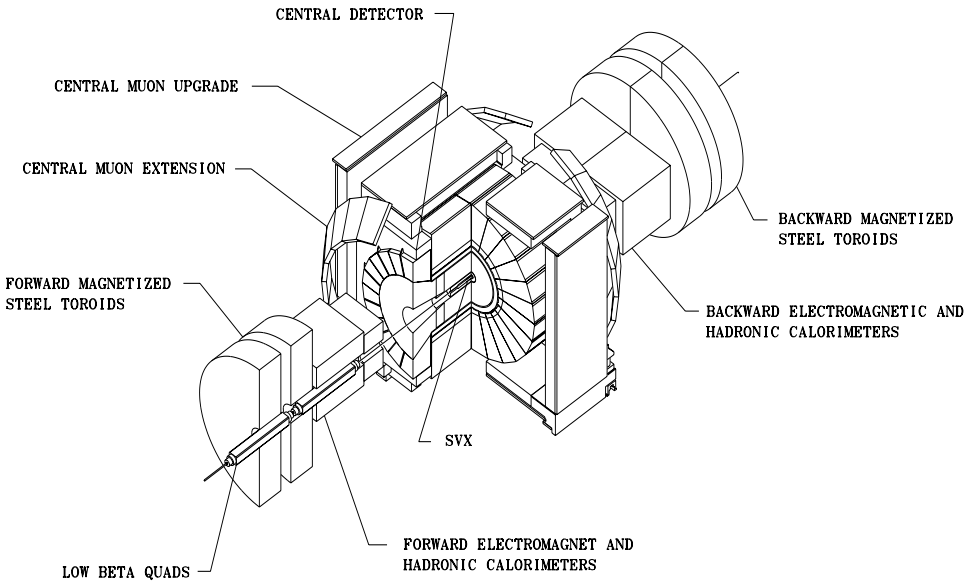

Figure 4.2: *Perspective view of the CDF detector.*

The coordinates used with the CDF detector are the direction of the proton beam z, the azimuthal angle ϕ, and the pseudorapidity $\eta = -\ln(\tan(\theta/2))$, where θ is the polar angle. The CDF detector is described in detail elsewhere [25]. Here we give a brief overview of the detector and discuss in more detail the detector components that are essential to this study.

4.3 Tracking

There are four separate tracking systems in the CDF detector. The closest to the interaction point are the Vertex Time Projection Chamber (VTX) [34] and

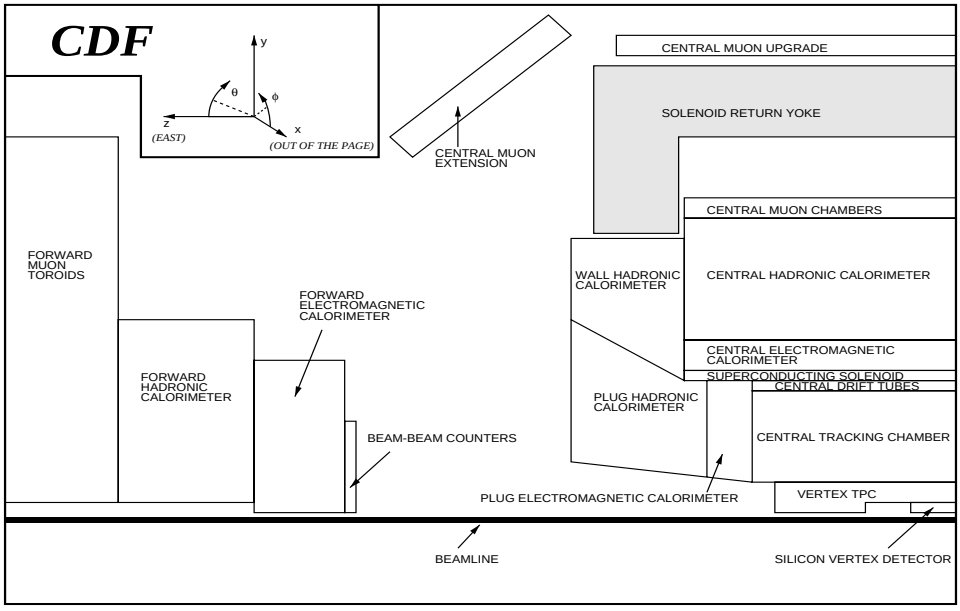

Figure 4.3: *Schematic side-view cross section of 1/4 of the CDF detector displaying main detector components.*

the Silicon Vertex Detector (SVX), which are located right after the 1.9 cm radius beryllium beam pipe. These detectors are used as stand-alone tracking systems for reconstruction of the primary $\bar{p}p$ interaction vertex; the SVX is also used for locating secondary decay vertices. In addition, the VTX and SVX information complements measurements obtained with the Central Tracking Chamber (CTC) for reconstruction of tracks of charged particles.

The VTX consists of eight time projection chambers mounted end-to-end along the beam direction. The chambers cover about eight units in pseudorapidity. Each octagonal VTX module has a central high voltage grid that divides it into two drift regions of 15.25 cm long. The electrons drift from the central grid to a cathode grid and enter one of the two proportional chamber endcaps, which are divided into octants, with 24 sense wires and 24 cathode pads in each octant. Measurement of the arrival times of the electrons at the sense wires provides a picture of the event in the $r - z$ plane. The VTX ϕ reconstruction uses pad data. An approximate r is

determined by the pad row. The combined $r - z - \phi$ information locates complete three-dimensional tracks. The minimum resolvable ϕ corresponds to one pad spacing of 1.4 cm. The z resolution varies with polar angle θ from 420 μm at 90° to 1100 μm at 11°.

The inner section of the VTX has a cavity built into it that contains the SVX. Four layers of the SVX silicon strip detectors extend ± 25 cm in z and surround the beam pipe at a distance 2.9 to 7.9 cm. The SVX consists of two barrels, mounted end-to-end at $z = 0$. Each barrel is segmented into 12 wedges, each of which covers 30° in ϕ.

The central tracking chamber of the CDF detector [35], which surrounds the VTX, occupies most of the volume of the superconducting, solenoidal 1.5 T magnet. The most important goal of the CTC is to provide a measurement of the track parameters of high P_T particles at both the trigger level and in the offline data reduction. The CTC is a cylindrical wire chamber with 84 layers of sense wires arranged into 9 superlayers. An end view of the CTC is shown in Figure 4.4. In five superlayers the wires are parallel to the beam line and are grouped into 12 sense wire layers. These five superlayers are interleaved with four superlayers of stereo wires, in which the angle between the sense wires and the beam line alternates between $\pm 3°$. Each stereo superlayer contains six sense wire layers. The axial superlayers provide the $r - \phi$ view, while the stereo superlayers provide the $r - z$ information.

There are in total 6156 sense wires and $\approx$ 2500 field shaping wires that establish a drift field of $\approx$ 1350 V/cm. Both axial and stereo superlayers are divided into cells so that ionized electrons reach the nearby sense wire within 800 ns of drift time, which corresponds to a maximum drift distance of 40 nm. The Lorentz angle of the electrons drifting in this electric field is 45° relative to the radial direction at magnetic fields of 1.5 T. In order to maintain linearity of the time-to-distance

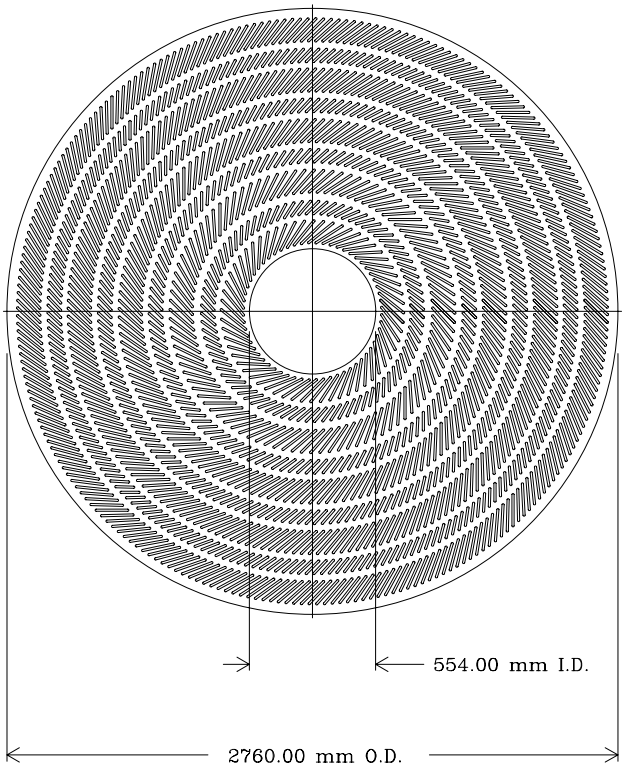

Figure 4.4: *End view of the Central Tracking Chamber.*

relationship the wire cells are tilted so that the drift trajectories are approximately azimuthal.

The CTC provides highly efficient charged particle track reconstruction in the pseudorapidity region $|\eta| < 1.1$ and measures particle momentum from the curvature of the track with a resolution of $\delta P_T/P_T^2 \leq 0.002$ $(\mathrm{GeV/c})^{-1}$. In the present analysis the CTC information was used for reconstruction of tracks of high-P_T electrons from W-boson decay and of the underlying event charged particles in the central pseudorapidity region.

The Central Drift Tube (CDT) array [38] is the fourth charged particle tracking system of CDF detectors. Three layers of 672 3 m long, 1.27 cm diameter drift tubes oriented parallel to the beam pipe surround the CTC at a radius of 1.4 m.

Each tube contains a 50 μm diameter stainless steel anode wire. The CDT, which operates in the limited stream mode, provides accurate $r-z-\phi$ information. The $r-z$ view of the CDT array is accomplished via charge division along the anode wires. Drift-time measurements in three layers of the CDT provide tracking information in the $r-\phi$ view.

4.4 Calorimetry

In the event analysis calorimeters are used for measuring the energy and the direction of particles and jets. Momenta and trajectories of charged particles are determined more precisely by tracking chambers in magnetic fields. However, calorimeters provide the most affordable way to measure parameters of all high energy particles, including neutral, which are "invisible" to tracking chambers.

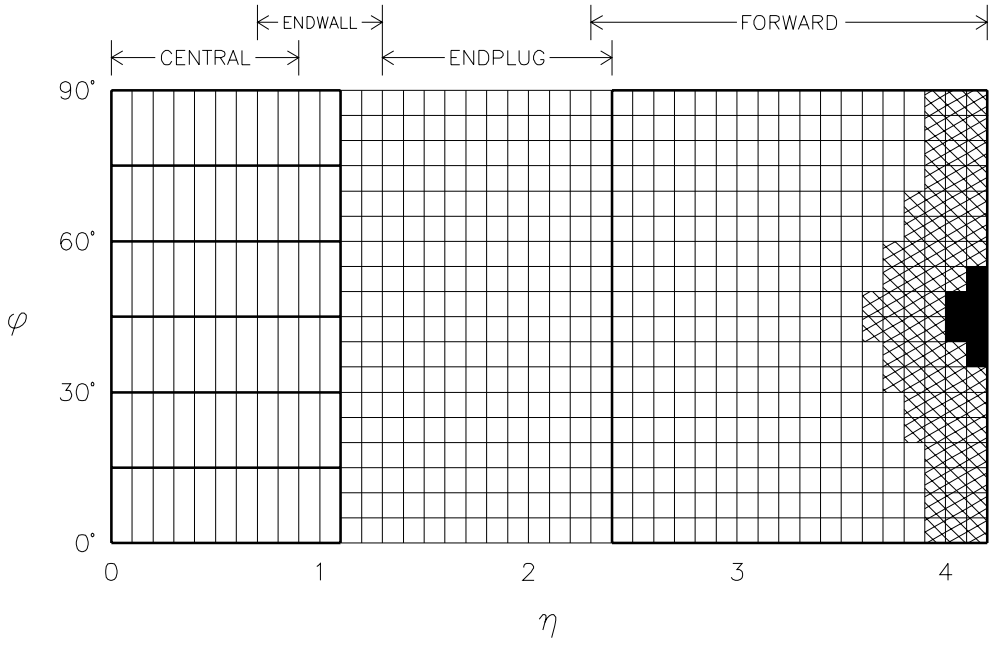

Figure 4.5: *Schematic $\eta-\phi$ segmentation of the CDF calorimeters. The shaded region represents partial depth coverage to accommodate the low-β quadrupole magnets; the black region has no calorimetric coverage.*

CDF is equipped with electromagnetic and hadronic calorimeters that cover the pseudorapidity range $-4.2 < \eta < 4.2$ and provide full coverage in ϕ (Figure 4.5). CDF employs sampling calorimeters, which in contrast to homogeneous calorimeters, detect only a fraction of the energy deposited by an incident particle. Layers of sampling material are interspersed with layers of absorber. A primary particle interacts with the material of the absorber producing a shower of secondary particles. Particles from the shower deposit a fraction of their energy in the active medium of the sampling layers, which is summed over all sampling layers. The true energy of the initial particle is determined by calibrating the calorimeter response to particles of known energy in test-beam measurements.

All CDF calorimeters have projective tower geometry, i.e. each tower points to the nominal interaction region.

4.4.1 Central Electromagnetic Calorimeter

The central electromagnetic calorimeter (CEM) [26] uses a hybrid design with scintillator and wavelength shifter for energy measurement and an embedded strip chamber for position determination. The CEM is arranged in 48 (24 at positive and 24 at negative z) separate modules, called wedges, each covering 15° in ϕ. Each wedge consists of ten towers, with each tower covering approximately 0.1 units in η. The layout of a wedge is shown in Figure 4.6. The CEM tower is a stack of 30 3.2 mm thick lead layers clad on each side with 0.38 mm of aluminum interleaved with 31 5 mm thick layers of polystyrene. This lead-scintillator sandwich has a thickness of approximately 18 radiation lengths for electromagnetic showers, which corresponds to one interaction length for hadronic showers. Constant radiation length and sampling fraction as a function of the polar angle θ are maintained by substituting acrylic layers for lead layers, increasing the number of acrylic layers with increasing $|\eta|$. The

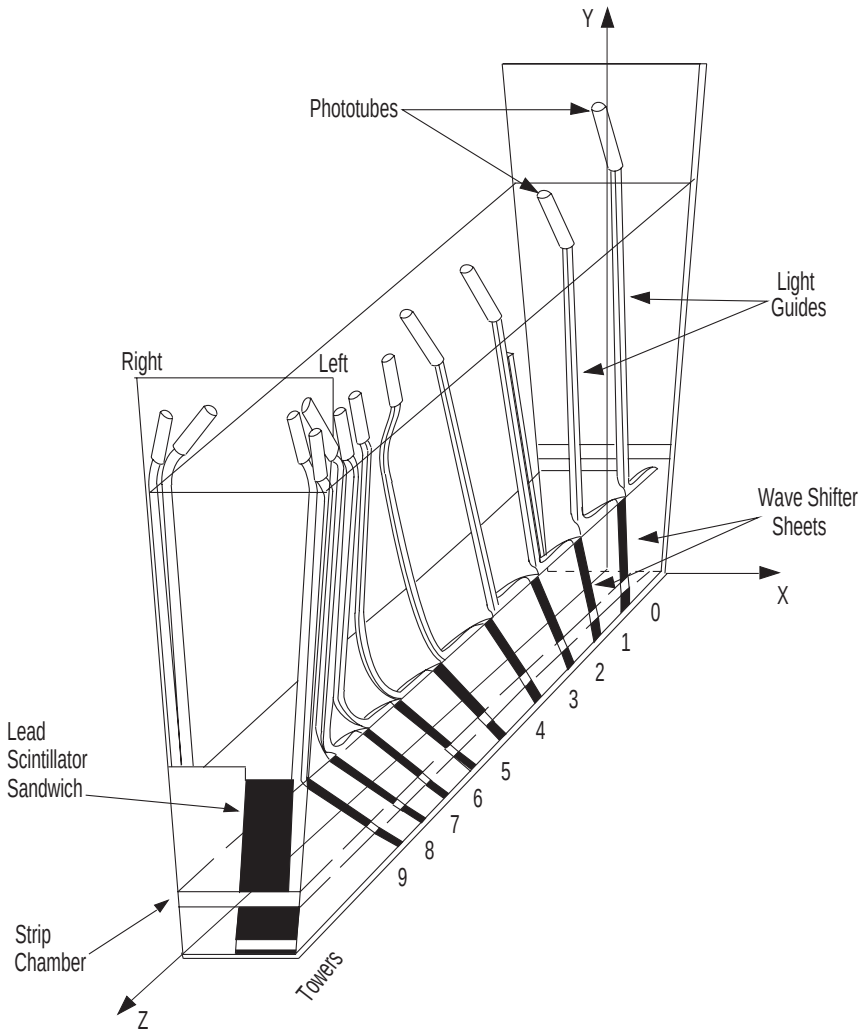

Figure 4.6: *Layout of the CEM light-gathering system in a single wedge of the CEM and CHA calorimeters.*

sides of scintillator behind acrylic are painted black, so that only scintillator layers behind lead sheets contribute to the observed signal.

The process of signal collection is the same for each tower of each module. The blue light from the scintillator is collected by wavelength shifters and transmitted by rectangular lightguides. The rectangular lightguides are glued to rectangular-to-round transition pieces, which pass the green waveshifted light to two photomultiplier tubes (PMT) per tower. Reading each tower with two PMT's on each side of the tower (Figure 4.6) is very effective in rejecting unphysical signals. The PMT's also receive calibration light signals.

Each tower was initially calibrated with 50 GeV electrons. The energy and position resolutions were measured in the electron beam energy range between 10 and 100 GeV. The electron energy resolution was $\sigma/E = 0.135/\sqrt{E \sin\theta} \pm 0.005$. All modules were also tested with cosmic rays [27].

Maintaining of the initial calibration was provided by three independent calibration systems [28]. In the first system, a computer controlled device, moves a Cs^{137} gamma point sources across the towers of each module. Currents in photomultiplier tubes are recorded as the point source moves through the towers in a module. The resulting current profiles for each tower reflect the combined response of the scintillator, wavelength shifters, light guides, and phototubes. Source runs are repeated periodically throughout the experiment.

In another calibration system, flashes of light produced by a xenon bulb illuminate a scintillator rod in each module. PIN diods monitor the light output of the scintillator rod, which is connected with quartz fibers to acrylic prisms mounted on the wavelength shifters. The ratio of PMT output to PIN diode output measures the response of wavelength shifters, lightguides, and PMT.

The third system uses flashes of green light from three LED's into quartz

fibers which are connected to the transition pieces between the light guides and PMT's. PIN diodes monitor the output of the LED's. The ratio of PMT output to PIN diode output measures the response of the PMT's.

A proportional strip chamber (CES) is inserted inside the stack between the eighth lead layer and the ninth scintillator layer, at the depth corresponding to the maximum average transverse shower development. The strip chamber improves position resolution for electrons and photons.

4.4.2 Central and Endwall Hadron Calorimeters

The central hadron calorimeter (CHA) is constructed directly outside the CEM in the same physical modules (see Figure 4.6). The CHA together with the endwall hadron calorimeter (WHA) [29] form a hadron calorimeter that covers polar angles between 30° and 150° ($|\eta| < 1.3$). Each calorimeter module is divided into projective towers, covering approximately 0.1 units in η and 15° in ϕ. For each 15° azimuthal slice there are 24 towers, of which 12 are in the central calorimeter, 6 in the wall calorimeter, and 6 are shared. The signal for the latter is the sum of the signals from the CHA and WHA.

The CHA and WHA are steel-scintillator sandwiches. The CHA consists of 32 layers of 2.5 cm thick steel plates interleaved with 1 cm thick plates of acrylic scintillator (PMMA) forming 4.7 absorbtion lengths. The WHA contains 15 layers of 5.0 cm thick steel plates perpendicular to the beam separated with 1 cm thick plates of acrylic scintillator (4.5 absorbtion lengths).

The method used for signal collection from the CHA and WHA is practically the same as for the CEM. The difference is that the CEM has a wavelength shifter on the constant ϕ side of each tower, while the CHA and WHA have wavelength shifter on the constant θ side. The light from the wavelength shifter strips is transmitted

by light guides, which are collected to form two square arrays at the azimuthally opposite sides of the tower, to "right" and "left" PMT's.

The CHA and WHA modules were tested and primarily calibrated in the test-beam and with cosmic rays. In addition to the primary calibration at the tower center, some preliminary studies of the calorimeter uniformity were also performed. The modules were mounted on a specially fabricated carriage, which automatically swept them through the beam in both polar and azimuthal directions.

Initially, each tower of two CHA modules was calibrated with 50 GeV charged pions, and the gains were adjusted to yield 2 pC/GeV. Then all CHA modules were calibrated with 50 GeV charged pions. Only two WHA modules were calibrated in the test beam. A system that longitudinally moves a Cs^{137} point source along the tower was used to transfer the test beam calibration to the rest of the WHA modules.

Good linearity of the CHA and WHA response to charged pions in the energy range 10-150 GeV was found for events where the primary pion didn't interact in the CEM. However, some non-linearity ($\sim$ 10% at 10 GeV) was observed when the pion shower started in the CEM.

The average energy resolution, which depends on the particular tower, for towers 1 to 5 of the CHA is $\sigma/E \approx 0.5/\sqrt{E} + 0.04$. The resolution for tower 10 of the WHA is $\sigma/E \approx 0.5/\sqrt{E} + 0.05$.

The calibration maintenance systems for the CHA and WHA consist of several source systems and a laser system. Like the CEM, the CHA and WHA have a line source system, which simultaneously illuminates all scintillators of a calorimeter tower and allows to monitor the response of the complete system of scintillators, wavelength shifters, light pipes, and PMT's. The system uses a linear Cs^{137} gamma source with a total strength of 3 mCi. The CHA employs also a computer controlled

source system that is capable of moving 3 mCi point-like γ sources into each module at a fixed longitudinal depth. The WHA uses 1.3 mCi sources. The system measures the product of the response of the scintillators and the gain of the PMT's. The direct measurement of the phototube gain is performed by the manual insertion of point-like β sources into the coupling blocks between the light guides and the phototubes. The laser system, based on a nitrogen laser, maintains the calibration of the CHA and WHA PMT's. A laser beam is split into six beams, which are transported through six optical fibers to light distribution scintillator disks. The light uniformly illuminates the ends of a set of optical fibers, which carry the light to the phototubes.

To correct the energy scale for long term variations, CEM and CHA Cs^{137} point source calibrations were performed every 2-4 weeks and WHA line source calibrations every few months. To correct for short term variations in the PMT's response, laser calibrations of the CHA and WHA were performed every few days.

4.4.3 Plug Electromagnetic Calorimeter

The plug electromagnetic calorimeter (PEM) [30] is a gas calorimeter that contains a mixture of 50% argon and 50% ethane gas with a small addition of alcohol. Two 2.5 m diameter and 50 cm deep round-shaped calorimeters cover the forward and the backward opening of the central detector system of CDF. The PEM is azimuthally arranged in eight 90° quadrants, four quadrants at positive z and four quadrants at negative z. Along the beam axis, the angular coverage is from 10° to about 36° in the polar angle θ, or $1.1 < \eta < 2.4$. The PEM projective towers cover 5° in ϕ, and there are sixteen towers segmented in η. In the polar angle the segmentation is $\Delta\eta = 0.09$ for 11 towers between 2.4 and 1.41 in η. The next four towers are 0.045 units of η each, with two towers per standard projective tower. The remaining tower, closest to 36°, is a standard tower of ~ 0.1 units of η. In the offline

analysis, the four small PEM towers are usually combined to form two standard towers, giving a total of fourteen standard towers at positive and likewise at negative η.

Each of the PEM quadrants consists of 34 layers of proportional tube arrays interleaved with 2.7 mm thick lead absorber panels. The proportional tubes are made of conductive plastic tubes of a square inner cross section of 7 mm $\times$ 7 mm with 0.8 mm thick walls. Each proportional tube contains a 50 micron gold-plated tungsten anode wire centered in a conductive plastic tube. The conductive plastic tubes were extruded out of polystyrene loaded with fine grain carbon powder. The surface resistance was chosen to be in a range of 60 to 100 KΩ/square. Each plane of the tube arrays in a quadrant consists of 156 tubes laid side by side perpendicular to the beam axis. The tubes are sandwiched by a pair of 1.6 mm thick copper clad G-10 panels. The copper on one side of the panel is segmented into pads with boundaries defined by the polar coordinates η, ϕ, and z. On the other side of the G-10 panel, the cathode signals from the pads are brought radially to the outer circular edge of the panel by etched strip lines. Summing the pad signals longitudinally gives a single tower signal. Longitudinal segmentation is achieved by ganging the necessary number of connectors at the same ϕ in three depth segments. The first segment contains the first five layers, the second the next twenty four, and the third the last five, respectively. The total thickness for electromagnetic and hadronic showers in the PEM is $18.2/\cos\theta$ radiation lengths and $1.0/\cos\theta$ interaction lengths, respectively.

All towers of the PEM were calibrated with 100 GeV electron beam. The PEM response was studied with electrons in the energy range from 20 to 200 GeV. The energy resolution was measured to be $\sigma/E \approx 0.3/\sqrt{E}$.

4.4.4 Plug Hadron Calorimeter

The plug hadron calorimeter (PHA) [31] is a gas calorimeter that consists of a sandwich of steel and gas-filled proportional tube layers. The PHA is azimuthally arranged in 24 30° sectors, twelve sectors at positive η and twelve at negative η. At the positive beam direction, the PHA covers the angular range $30° < \theta < 10°$ $(1.1 < \eta < 2.4)$. The PHA is segmented in towers of 5° in ϕ and 0.09 units of η.

Each gas proportional tube consists of a 50 μm diameter gold plated tungsten wire in a resistive plastic tube of rectangular cross section. The tube has the same dimensions as the PEM tubes. The PHA tubes are laid side by side, sandwiched by a copper ground plane and copper cathode plane. The cathode plane consists of electrically distinct pads on the inner side and is connected to the outer side via a plated through hole. Copper traces on the outer side of the plane carry the cathode signal to the edge of the chamber. Each chamber consists of 72 pads, 12 rows by 6 columns. Twenty proportional tube layers are sandwiched by twenty-one steel plates to form a single sector of the hadron calorimeter. The signals from each chamber in the sector are ganged together longitudinally to form twelve towers, seventy-two towers per sector. The cathode tower signals are then amplified and digitized. In addition, the common anode signal of all the tubes in a single chamber is picked off the HV supply line. The anode signal for each chamber is separately amplified and digitized, providing information on longitudinal shower development. Longitudinal information from the anode signal, and electromagnetic energy in the PEM, helped distinguish real energy from "cable noise".

Each of the seventy-two pads were calibrated with Cd^{109} sources. The proportional tubes under each pad were exposed to 8 KeV copper fluorescence x-rays, and the signals on both the cathode pad and anode wire were recorded. The

anode signals from a standard chamber were also recorded during the calibration of each chamber.

The PHA was calibrated with charged pions between 20 and 230 GeV. The response was linear and the energy resolution was measured to be $\sigma/E \approx 0.86/E + 0.04$.

4.4.5 Forward Electromagnetic Calorimeter

The forward electromagnetic calorimeters (FEM) [32] are located approximately 6.5 m from the interaction point and enclose the beam pipe at either end of CDF. The FEM is azimuthally arranged in 90° quadrants, four quadrants at positive

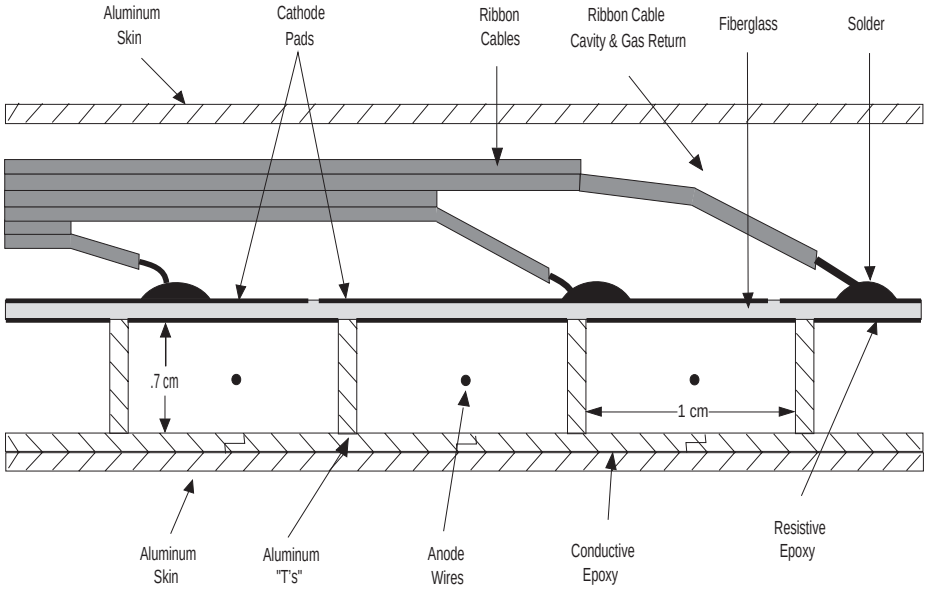

Figure 4.7: *Cross section of a FEM chamber.*

η and four quadrants at negative η. The FEM is segmented into projective towers in ϕ and η. The FEM towers span 5° in ϕ, and there are twenty towers in η. The first tower is of 0.03 units of η, the next nineteen divisions are normal sized towers, each 0.1 units of η. At the positive beam direction, the nineteen normal towers cover the

angular range $11^\circ > \theta > 2^\circ$ ($2.3 < \eta < 4.2$). These towers are shown in Figure 4.5. Each calorimeter consists of 30 sampling layers. Each layer is made of a lead sheet and a chamber of gas proportional tubes with cathode and readout. A cross section of a chamber is shown in Figure 4.7. One side of each proportional chamber in this calorimeter consists of an aluminum channel plate which forms three walls of the 124 proportional tubes. The channel plate is manufactured by attaching aluminum channels having "T" profile to a large aluminum sheet. Then fiberglass is glued with resistive epoxy to the aluminum channels to form a series of rectangular proportional tubes. The resistive epoxy forms the mechanical bound and serves as a resistive path to ground for positive ions resulting from electron avalanches. A 50 μm gold-plated tungsten wire in the center of each tube is used as the anode, and copper pads on the outer side of the fiberglass are the divided cathode. There are 1440 pads per layer, resulting in a total of 5760 tower segments. A complete chamber is an aluminium box about 1.5 m on a side and about 1.6 cm thick. Cathode signals are carried to the edge of the chamber by ribbon cables. The pads are ganged longitudinally into towers with two depth segmentations, both of which are fifteen layers thick. The anode wires are strung vertically and are ganged together in five sectors per chamber. These sectors are read out independently for each layer, and provide a longitudinal profile of the energy deposition for each sector.

Four quadrants of the FEM were calibrated with electron beams from 20 to 200 GeV. The calorimeter response as a function of incident electron energy was found linear in the energy range from 20 to 160 GeV. The electron energy resolution was $\sigma/E \approx 0.25/E + 0.005$.

4.4.6 Forward Hadron Calorimeter

The CDF Forward Hadron Calorimeter (FHA) [33] is a sandwich constructed of proportional tube chambers and steel plates. The FHA is azimuthally segmented into 90° sections stacked around the beam pipe, four sections at positive z and four sections at negative z. Each calorimeter segment is composed of 27 (213 cm$\times$ 213 cm $\times$ 5 cm) steel plates and 27 (204 cm$\times$ 196 cm $\times$ 2.5 cm) ionization chambers which are located between a pair of steel plates. The construction of the ionization chambers is similar to the FEM, but the tubes are about 1.5 times larger. The total assembly contains 400 tons of steel plates and 216 ionization chambers, which adds up into $8/\cos\theta$ interaction lengths for hadronic showers. The cathode surface of each chamber is segmented into 19 bins in η ($\Delta\eta = 0.1$) and 18 bins in ϕ ($\Delta\phi = 5°$) forming a projective towers that cover the angular range $11° > \theta > 2°$ ($2.3 < \eta < 4.2$) (see Figure 4.5). The sum of the signals from each chamber pad at fixed η and ϕ forms the total signal for a given projective tower. In addition to the cathode pad information, the signals from 50 μm anode wires segmented into six sections per chamber are used for monitoring the longitudinal shower development.

The FHA was calibrated with charged pion beams in the energy range 20-200 GeV/c. The calorimeter response was linear up to 200 GeV/c with no evidence for saturation. The energy resolution of the calorimeter is $\sigma/E \approx 1.4/\sqrt{E}$.

4.5 Muon Detectors

There are two muon detection systems in CDF. The central muon system covers the pseudorapidity region $|\eta| < 0.6$ and consists of two sets of muon chambers. The Central Muon detector (CMU) [36] is located around the outside of the CHA at a distance of 347 cm from the beam axis. There are about five interaction lengths

of material between the CMU and the beam axis. The CMU is segmented in ϕ into 12.6° wedges, each of which is segmented further into tree modules of 4.2° each. Each module in a wedge consists of four layers of four rectangular drift cells. A stainless steel resistive 50 μm sense wire is located at the center of the cell. Four sense wires, one from each layer, form a muon tower. To resolve an ambiguity as to which side of the sense wires in ϕ a track passes, two wires of the tower are offset by 2 mm at the midpoint of the chamber, and the difference in arrival times of the drift electrons is measured. Behind an additional eight interaction lengths of steel is located the Central Muon Upgrade detector (CMUP). The CMU and CMUP provide 85% and 80% azimuthal coverage, respectively. In addition, two pairs of conical arches of drift chambers in the pseudorapidity range $0.6 < |\eta| < 1.0$ form the Central Muon Extension detector (CMX).

The CDF Forward Muon system (FMU) [37] consists of a pair of magnetized iron toroids, which cover the pseudorapidity range $2 < \eta < 3.6$. Each toroid is instrumented with three sets of drift chambers and two planes of scintillation counters. The FMU is used for measuring muon position and momentum. In addition, a forward muon trigger allows to select high-P_T muon events.

4.6 Beam-Beam Counters

The CDF detector is equipped with a plane of scintillation counters on the front face of the forward calorimeter on east and west sides of the detector. These scintillator hodoscopes, called the beam-beam counters (BBC) [39], are primarily used to provide a "minimum bias" (MB) trigger for the detector and also to estimate the luminosity. Each BBC consists of a plane of sixteen scintillator counters, located close to the beam pipe, at a distance of 582 cm from the interaction point. The

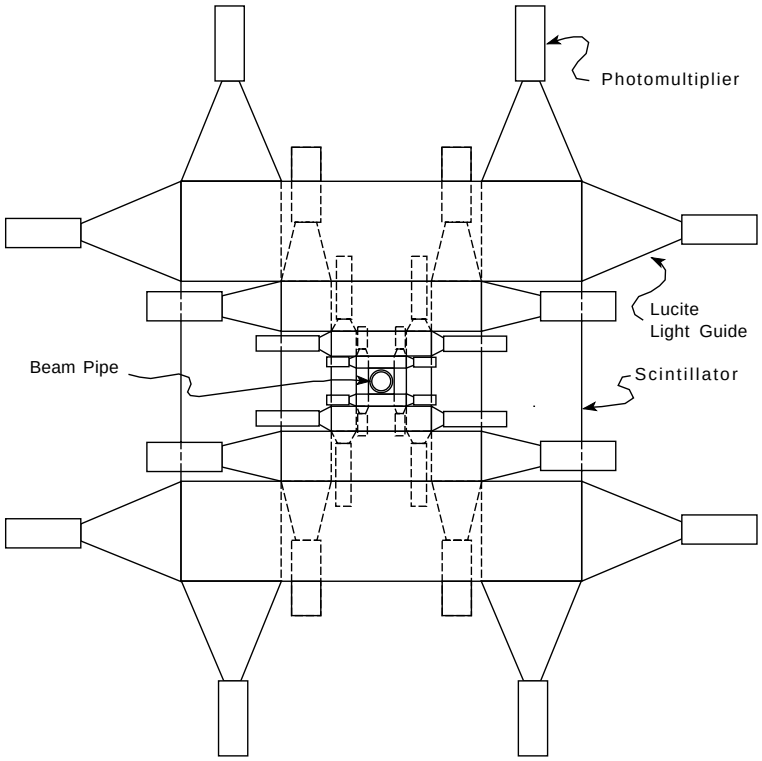

Figure 4.8: *Front view of one of the Beam-Beam Counter planes.*

counters are arranged in a criss-cross grid around the beam pipe, forming four concentric squares, as shown in Figure 4.8, covering the angular range $4.5^\circ > \theta > 0.32^\circ$ ($3.2 < \eta < 5.9$). The counters have excellent timing properties ($\sigma < 200$ ps), providing the best measurement of the time of the interaction. A coincidence between the counters on each side of the interaction point, within a fifteen nanosecond gate centered twenty nanoseconds after the beam crossing, forms the minimum bias trigger. The minimum bias trigger rejects unwanted triggers, i.e. collisions between the beam and residual gas in the beam pipe (beam-gas), beam halo, and cosmic rays.

The integrated luminosity is measured as a number of BBC east-west coincidences divided by the fraction of the $p\bar{p}$ total cross section accepted by the BBC's. The total, elastic and single-diffractive $p\bar{p}$ cross sections were measured in CDF

[17, 18, 19], and the total cross section accepted by the BBC's was found to be 51.2 ± 1.7 mb [49].

In the analysis of this thesis, the beam-beam counters play a key role in measuring the charged particle multiplicity in the forward region and are used, together with the adjacent forward calorimeter, for tagging events with a forward rapidity gap.

4.7 Trigger System

One beam crossing at the Tevatron occurs every 3.5 μs. Therefore, with a luminosity of $L \approx 10^{31}$ cm^{-2}s^{-1} at least one interaction is expected at every beam crossing, yielding ~ 250 KHz event rate. The rate at which events can be written to tape is ≈ 6 Hz. A three-level CDF trigger system [39] is used to perform the data flow reduction and to determine which event is to be accepted and saved to tape. The trigger is designed to exploit both electromagnetic and hadron calorimeter towers, which are grouped into $\Delta\phi = 15^\circ$ and $\Delta\eta = 0.2$ trigger towers. The signals are weighted by $\sin\theta$ to represent the transverse energy, E_T.

Typical Level 1 trigger criteria are that the sum of E_T for all calorimeter trigger towers be greater than 30-40 GeV, or that there is a single tower above some preprogrammed threshold, or a signal from the muon chamber, or a beam-beam counter coincidence, etc. Various combinations of the above criteria form different Level 1 triggers.

After a Level 1 trigger decision to accept an event, the Level 2 trigger uses the same 42×24 array of towers in $\eta - \phi$ to search for clusters of electromagnetic or total energy above some predefined threshold. Electromagnetic and hadronic energies of all towers identified as being a cluster are summed separately, digitized

and passed to a fast hardware Level 2 processor. For each cluster, the fast hardware tracking processor matches tracks found in the CTC. The result of the Level 2 trigger processing is identification of electron, photon, muon, and jet candidates.

The Level 3 trigger, based on a Silicon Graphics CPU farm of 48 1000 MIP parallel processors, receives an event from the Level 2 processor and performs a complete event reconstruction. The Level 3 event reconstruction procedure is virtually the same as in offline analysis. The only differences are that at the Level 3 event reconstruction E_T is calculated relative to the $z = 0$ point rather than to the z position of the actual event vertex and that the final data base constants for tracking and calorimetry are not available at that stage.

4.8 Data Acquisition System

The CDF detector has a total of $\sim 100,000$ electronic channels of photomultiplier tubes; strip, wire, and pad chambers; drift chambers; drift chambers with current division readout; and silicon strip detectors. Due to a very large dynamic range, $\sim (0.001 - 100)$ GeV, required by the calorimetry readout, a special Redundant Analog Bus-Based Information Transfer (RABBIT) [40] system was developed at Fermilab to meet this requirement. The RABBIT system, which consists of 129 crates mounted on the detector, service the calorimetry, which has about 60000 channels. The rest of the channels, which are mostly those of the drift chambers, are read out by a commercial FASTBUS [40] system. The CDF data acquisition process is controlled by the multilevel FASTBUS network [41]. After an event is accepted by both Level 1 and Level 2 triggers, data from the front-end RABBIT and FASTBUS crates are digitized and read by scanner modules. This step in the DAQ pipeline is managed by the Trigger Supervisor (TS) FASTBUS module. When the scanner

modules have finished reading and buffering data for one event, the TS sends a FASTBUS message to the Buffer Manager (BFM), which supervises dataflow from scanners to host VAX computers, indicating that an event is available in a specified buffer. The BFM initiates the dataflow by sending a FASTBUS message to a group of FASTBUS modules, called Event Builder (EVB), to read the event from the scanner buffer. When the EVB has finished reading and reformatting the event data from the scanner buffer, it sends a message to the BFM, which in turn notifies the TS that the buffer is ready for a new Level 1/Level 2 trigger. The BFM then sends the event data to the Level 3 trigger system. After the Level 3 selection, accepted events can be logged to disk or tape and accessed in real time by consumer processes executing on both host and remote computers.

Chapter 5

Monte Carlo Studies

This analysis is based on the rapidity gap method (see section 3.1). Therefore, for correct evaluation of the acceptance of events with a gap, it is important to understand well and correctly simulate the underlying event distributions. In this chapter we examine the Monte Carlo programs that were used for calculation of the diffractive and non-diffractive acceptances.

Diffractive W-boson production is simulated using the POMPYT 1.0 Monte Carlo program [43], which is based on the model for hard diffraction [7] described in section 2.5. We use a hard-quark pomeron structure given in Eqn. (3.1) and a flux factor of the type (2.17) with parameters [45] $\alpha(t) = 1.115 + 0.26\,t$ and $K = 0.73$ GeV^{-2}. POMPYT 1.0 makes use of the PYTHIA 5.6 program [42] to simulate a wealth of hard scattering processes, and employs JETSET 7.3 for hadronization to give an observable hadronic final state. The POMPYT, PYTHIA, and JETSET parameter settings for simulation of diffractive W production are presented in Appendix A.

PYTHIA 5.6 and JETSET 7.3 are also used for simulation of non-diffractive W-boson production. Parameter settings for simulation of non-diffractive W production are given in Appendix B.

5.1 Comparison between PYTHIA and MBR Minimum Bias Events

In order to investigate the underlying event simulation by PYTHIA and JETSET, we first compare PYTHIA minimum bias (MB) events with MB events generated using the MBR Monte Carlo program [16], which has been developed at CDF and used in simulations in connection with the measurements of total, elastic and single diffraction cross sections [17, 18, 19]. The MBR Monte Carlo represents well the MB $dn/d\eta$ distributions in the CDF measurements, except that the average track multiplicities were found to be about 10% higher than the MBR predictions.

Figure 5.1 shows the total and charged particle $dn/d\eta$ distributions generated by PYTHIA (solid) and by MBR (dotted) for $\sqrt{s}$ = 200, 312 and 1800 GeV. The low energies were chosen to correspond to the diffractive mass region to which we are sensitive (312 GeV corresponds to $\xi = 0.03$). The shapes of the distributions agree well, however PYTHIA gives about 10% higher integrated multiplicity than MBR. Therefore, we conclude that PYTHIA provides a good representation of the CDF data, better than that of the MBR.

5.2 Comparison between PYTHIA Non-Diffractive W and Minimum Bias Events

A comparison of the $dn/d\eta$ distributions of particles produced by interactions of the spectators in W events (W underlying event) and particles from minimum bias production, simulated with PYTHIA at $\sqrt{s}$ = 200, 312 and 1800 GeV, is presented in Figure 5.2. The W underlying event is obtained by removing from an event

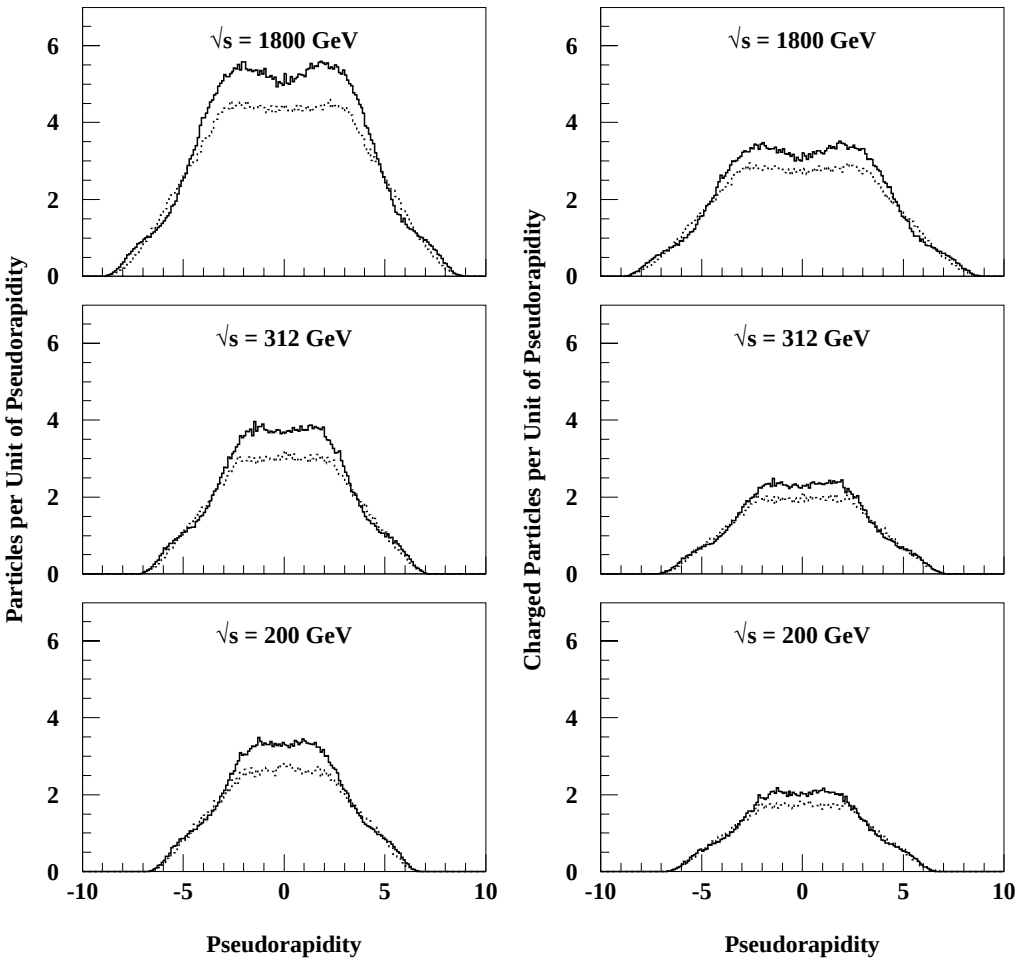

Figure 5.1: *Total (left) and charged (right) particle $dn/d\eta$ distributions for* PYTHIA *(solid) and MBR (dotted) minimum bias events.*

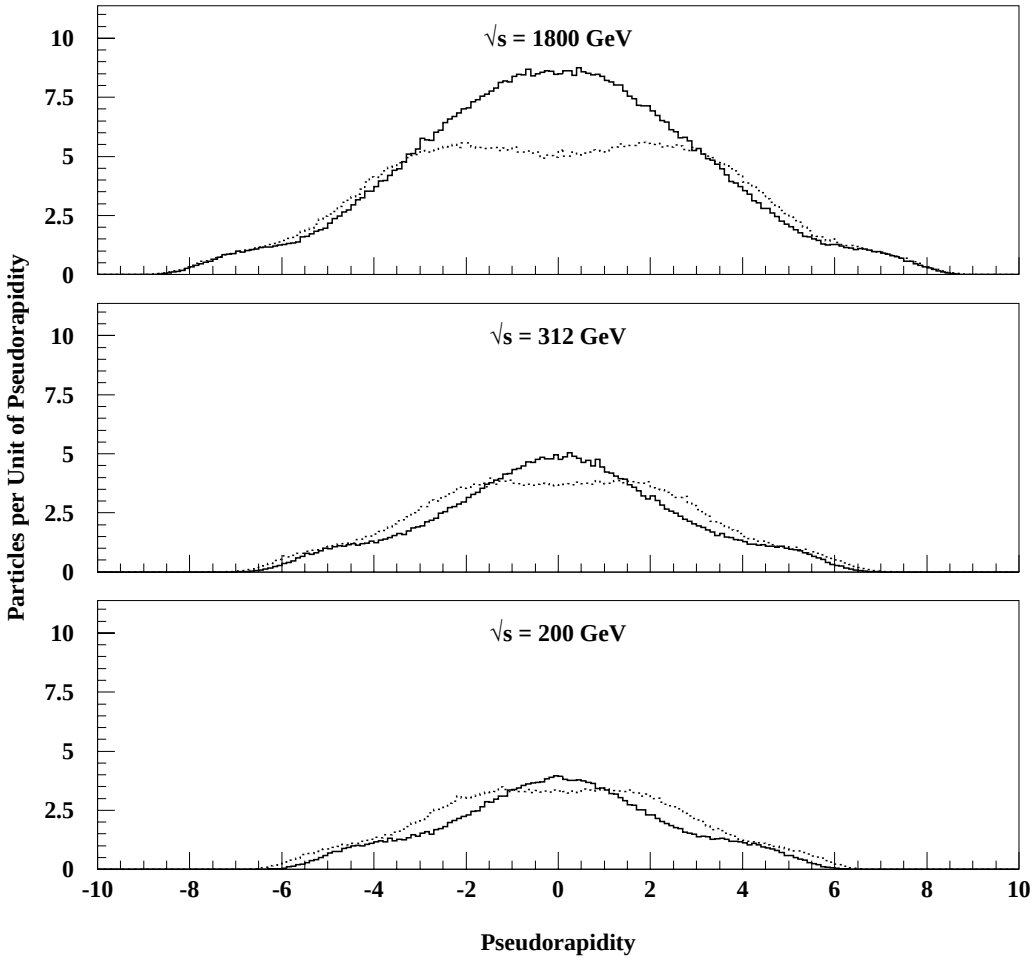

Figure 5.2: *Comparison of the $dn/d\eta$ distributions for the underlying event in W-boson production (solid), and for minimum bias events (dotted), simulated with the* PYTHIA *Monte Carlo program for $\bar{p}p$ collisions at 200, 312 and 1800 GeV.*

the electron(positron) from the W decay. At 1800 GeV, the $dn/d\eta$ distribution for W production is higher in the central region by a factor of about 1.5. However, the wings of the two distributions for $|\eta| >\sim 3$ are practically identical. At 200 and 312 GeV, the W and MB distributions are similar.

5.3 Comparison of PYTHIA with POMPYT

In Figure 5.3 we compare the $dn/d\eta$ distributions of the underlying event in W production simulated with POMPYT (solid) and with PYTHIA (dotted). In POMPYT, a pomeron with a hard-quark structure emitted by the proton collides with an antiproton at a $I\!P - \bar{p}$ c.m. energy of 312 or 200 GeV. PYTHIA was run for non-diffractive $p\bar{p}$ collisions at $\sqrt{s}$ = 312 and 200 GeV and the distributions were boosted appropriately. The POMPYT and PYTHIA distributions differ slightly in the pomeron direction, presumably due to the difference between the pomeron and the proton parton densities. However, the overall shape and normalization of the distributions are nearly the same.

Figure 5.4 shows POMPYT (with a hard-quark pomeron) and PYTHIA MB $dn/d\eta$ distributions (the POMPYT W distributions of Fig. 5.3 are superimposed for comparison). The PYTHIA MB distributions are boosted appropriately. The effect of the hard structure of the pomeron is seen clearly as peaking of the $dn/d\eta$ distributions in the pomeron direction. At 200 GeV, the rapidity gap in diffractive W events is larger than that of the MB events, presumably due to the effect of the W mass.

From the above comparisons we conclude that PYTHIA and JETSET provide a consistent representation of the underlying event distributions for diffractive and non-diffractive events at the generation level and, after taking into account the detector effects, can be used in the gap acceptance calculations for diffractive and

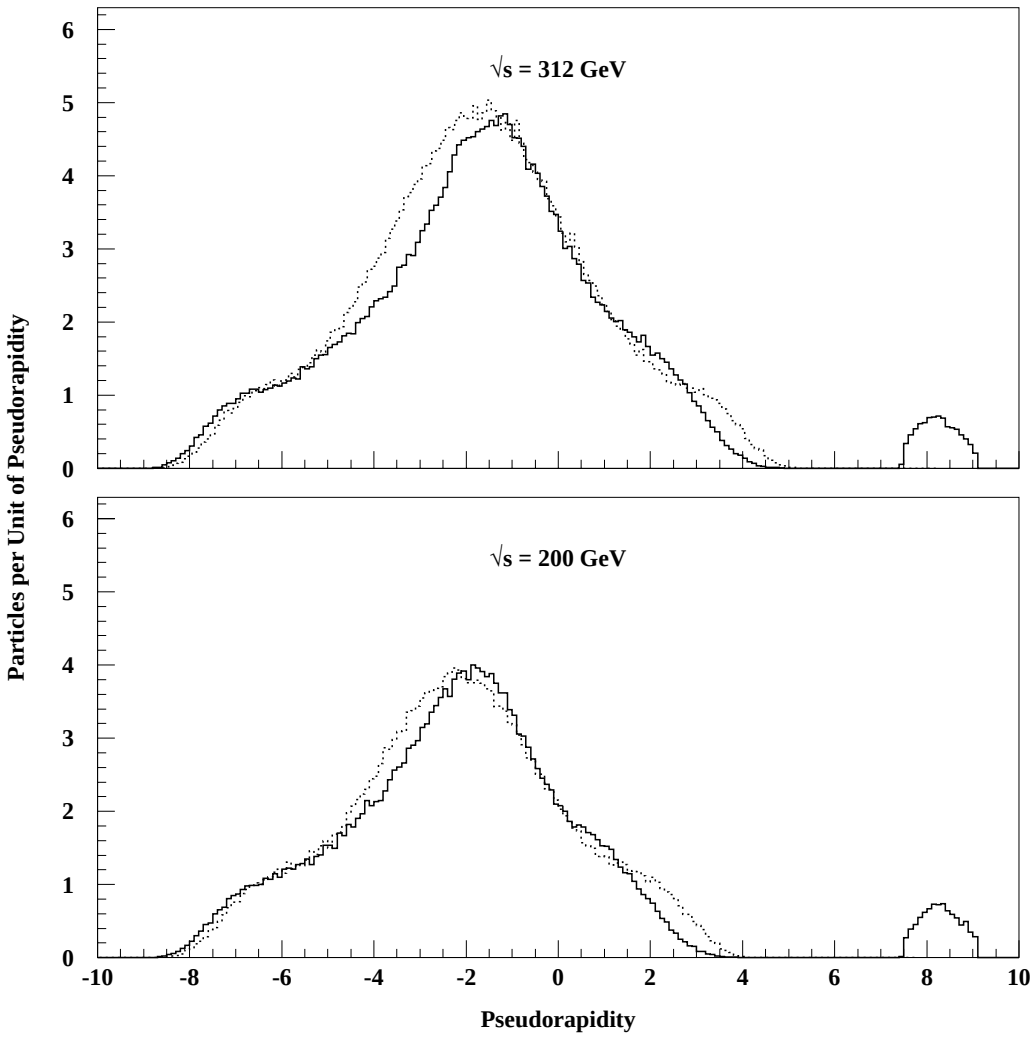

Figure 5.3: *$dn/d\eta$ distributions of the underlying event in W production obtained with* POMPYT *(solid) and* PYTHIA *(dotted).*

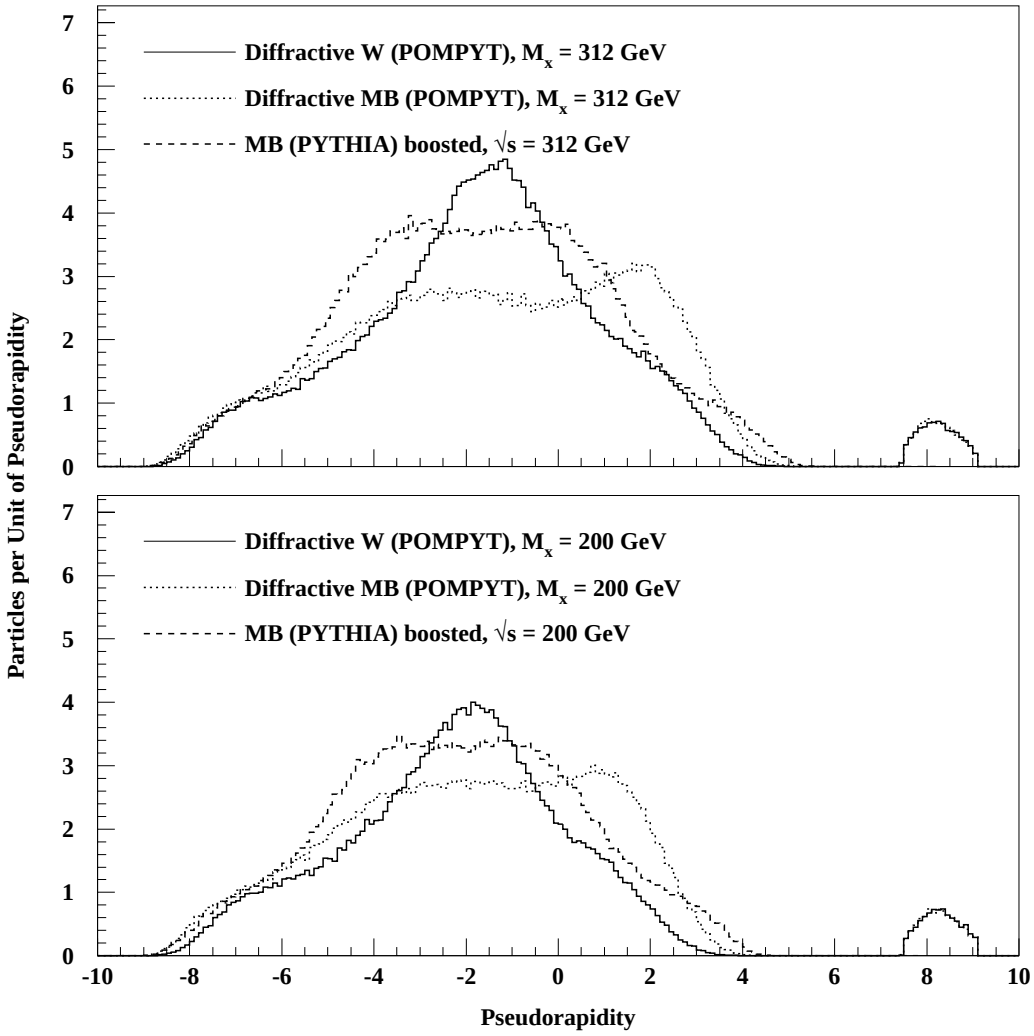

Figure 5.4: *Comparison of the $dn/d\eta$ distributions for the underlying event in diffractive W production (solid) (*POMPYT *with a hard-quark pomeron), for diffractive minimum bias events (dotted) (*POMPYT *with a hard-quark pomeron), and for* PYTHIA *minimum bias (dashed) events (boosted).*

non-diffractive W events.

Chapter 6

Data

The data were taken during the Tevatron collider runs which started in 1992 and continued through 1995. In run 1A (1992-1993), the CDF collaboration gathered 19.6 ± 0.7 pb^{-1} of data. From the start of run 1B in 1994 to February 1995, the Tevatron Collider had delivered over 100 pb^{-1} of collisions and the integrated luminosity recorded at CDF in run 1B was 100.6 pb^{-1}.

Two data samples, from runs 1A and 1B, collected by the CDF experiment have been used here for measuring diffractive W-boson production.

6.1 Analysis of Diffractive W-boson Production

6.1.1 W Sample

The W data sample was obtained by triggering CDF on a high transverse momentum, $P_T = P \sin\theta_e$, central electron/positron candidate in the central pseudorapidity region ($|\eta| < 1.1$). No information was required in the trigger that would bias the search for forward rapidity gaps. However, only a part of the run 1A sample was suitable for the purposes of this analysis, namely the part in which the require-

ment for the BBC coincidence was removed from the trigger. The total integrated luminosity of that subsample is ~ 6.7 pb^{-1}. The BBC trigger requirement was not present in run 1B, and therefore the whole high-P_T central electron/positron sample corresponding to ~ 86 pb^{-1} was considered in the analysis.

The high-P_T central electron/positron sample was then used to select W events by requiring large missing transverse energy in an event. The missing transverse energy, $\not\!\!E_T$, is defined as the magnitude of the vector that balances the vector sum of E_T in all calorimeter cells within $|\eta| < 3.6$.

It is necessary to note here that the central muon W sample was not considered in this analysis because of the following reasons. The effective pseudorapidity coverage for central muons is restricted to $|\eta| < 0.6$, as compared to $|\eta| < 1.1$ for central electrons/positrons. As a result, the analysing power of the angle correlation asymmetry for muons is rather poor. As for the charge correlation asymmetry, this is also problematic for the muons, because there is a rather substantial (several percent) systematic asymmetry in the measurement of the muon charge, which would increase the systematic uncertainty of the overall result.

Trigger Requirements

The first level of the central electron/positron trigger requires that at least one calorimeter trigger cell with $\Delta\eta \times \Delta\phi = 0.2 \times 0.26$ has greater than 6 GeV of electromagnetic energy.

At the second trigger level, central calorimeter towers are combined in clusters of three towers in pseudorapidity and one tower in azimuth. The energy of a central electron/positron candidate is reconstructed from the sum of the energies measured in a cluster of towers in the CEM. For each tower, the geometric mean of the charge from the two phototubes, one on each side in azimuth, is used as the

measure of the tower energy. The geometric mean is used to reduce the dependence of the energy measurement on the local shower position due to light attenuation in the scintillator. To construct clusters of energy, seed towers are chosen from an event as the towers with the largest transverse energy. The two towers on either side of a seed tower in the z direction ("shoulder towers") are included in the cluster. Once a tower is used as a shoulder, it cannot be used as a seed. Individual clusters continue to be identified in this way until no towers above the seed tower threshold of 8 GeV remain. At the Level 2 trigger, for a cluster to be associated with an electron/positron candidate, there must be a CTC track extrapolating to the CEM cluster with P_T greater than 12 GeV/c, the ratio of the hadronic energy summed over the towers in the cluster to the electromagnetic energy in the cluster, HAD/EM, must be less than 12.5%, and the transverse energy of the cluster be greater than 16 GeV.

At the third trigger level, additional electron/positron selection variables are used to discriminate against charged hadrons. A comparison of the lateral shower profile in the calorimeter cluster with that of test beam electrons is used by considering energy sharing between the towers in a cluster, L_{shr}. The distance between the position of the extrapolated track and the shower position in the CES is measured in the $r-\phi$ and z views: Δx and Δz. A χ^2 comparison of the CES shower profiles with those of test beam electrons is made by using $\chi^2_{\rm strip}$. The Level 3 trigger selects high-P_T central electron/positron candidates by increasing the cluster E_T cut to 18 GeV, the track P_T cut to 13 GeV/c, and requiring $L_{shr} < 0.2$, HAD/EM < 0.125, $\Delta x < 3.0$ cm, $\Delta z < 5.0$ cm, $\chi^2_{\rm strip} < 10$.

Lepton Selection Cuts

The selected high-P_T central electron/positron candidate sample is processed further in the offline analysis by applying the set of standard CDF isolated electron/positron quality cuts, after the central electron/positron energy is corrected using the CDF standard CEMFIX routine.

- The electromagnetic energy sharing between towers in a cluster, L_{shr}, is required to be less than 0.2.

- The χ^2_{strip} for the comparison of the shower profile from the strip chambers with that of the test beam electrons must be smaller than 10.

- The ratio of the hadronic energy summed over the towers in the cluster to the electromagnetic energy in the cluster, HAD/EM, has to be less than $(0.055 + 0.00045E)$, where E is the total energy of the cluster.

- An isolation requirement is applied by demanding that the transverse energy in a cone with $R = \sqrt{(\Delta\eta)^2 + (\Delta\phi)^2} = 0.4$ around the electron cluster excluding the transverse energy of the electron cluster be less than 10% of the electron cluster's E_T.

- The ratio of the cluster energy and the track momentum, E/P, must be in the range $0.5 < E/P < 2.5$ in order to separate it from minimum ionizing particles on one side and to ensure consistency between the electron energy measured in CEM and its momentum measured with CTC on the other side.

- A beam-constraint fit is applied in measuring parameters of the track associated with a tower cluster by adding to the fitted points the coordinates of the beam stored in each beam crossing.

- After implementing the beam-constraint fit the z-position of the closest approach of the electron/positron track to the beam axis is required to be within ± 60 cm of the origin of the detector coordinates. This value corresponds to 2σ deviation from the mean of the event $z_{\rm vertex}$ distribution.

- For matching of the extrapolated track position with the shower position in CES, it is required that $\Delta x < 1.5$ cm and $\Delta z < 3.0$ cm.

- The impact parameter, D0, determined as the minimum distance of the reconstructed track from the beam line, must be less than 0.2 cm.

- The distance between z-coordinates of the track and the closest reconstructed primary vertex shall not exceed 2 cm.

- To avoid possible misidentification of the lepton charge, which is determined by the curvature of a track, the curvature significance, defined as the fitted curvature divided by its error from the fit, is required to be less than 2.

- The electron/positron candidate must be confined within a fiducial volume to avoid uninstrumented regions.

- The electrons/positrons from γ conversions are filtered using the CDF standard CONVERT routine.

- At the end of the central electron/positron selection procedure, the beam constraint P_T of the electron/positron candidate track is required to be greater than 15 GeV/c, and the corrected E_T greater than 20 GeV.

Central Electron/Positron W Sample

In diffractive W events, a second minimum bias interaction could rise the multiplicity on the rapidity gap side of the event. In order to eliminate events with

more than one interactions during the same beam-beam crossing, the one-vertex requirement is imposed. This is done by selecting events with only one VTVZ bank and requiring that the primary vertex be contained within ± 60 cm from the nominal vertex position along the z axis.

The W events are tagged by demanding that the $\not\!\!E_T$ in an event be greater than 20 GeV. There can be only one electron that passes all the selection cuts. The electron must be contained in the pseudorapidity region $|\eta| < 1.1$. To reduce possible non-W background, the W transverse mass, defined as

$$M_T^W = \sqrt{2 \cdot E_T^e \cdot \not\!\!E_T (1 - \cos(\phi_{e\nu}))}, \tag{6.1}$$

where E_T^e is the electron/positron transverse energy and $\phi_{e\nu}$ is the azimuthal angle between directions of the electron/positron and the $\not\!\!E_T$ vector, has to be in the region $40 < M_T^W < 120$ GeV/c^2.

We note here that the presence of non-W background in the event sample, if any, is not crucial for this analysis. If present, it is not expected to be angle-gap or charge-gap correlated. Hence, it can contribute only to the denominator of the ratio in Eqn. (3.10) and reduce it in direct proportion. It has been estimated that the non-W background, after the described selection procedure, is expected to be less than a few percent, which is much smaller than the precision of our measurement.

For the data of run 1B, a systematic shift of the event $z_{\rm vertex}$ distribution relative to the center of the detector by an average $\sim$ 1.5 cm was observed. However, this small shift did not affect the analysis. A more serious problem was an asymmetry observed in the $z_{\rm vertex}$ distribution for events from the first part of the run ($55627 <$ run# < 61739).

Figure 6.1 shows the $z_{\rm vertex}$-distribution for W(central electron/positron) events from run 1B: (dotted line) events from $55267 <$ run # < 61739; (solid line)

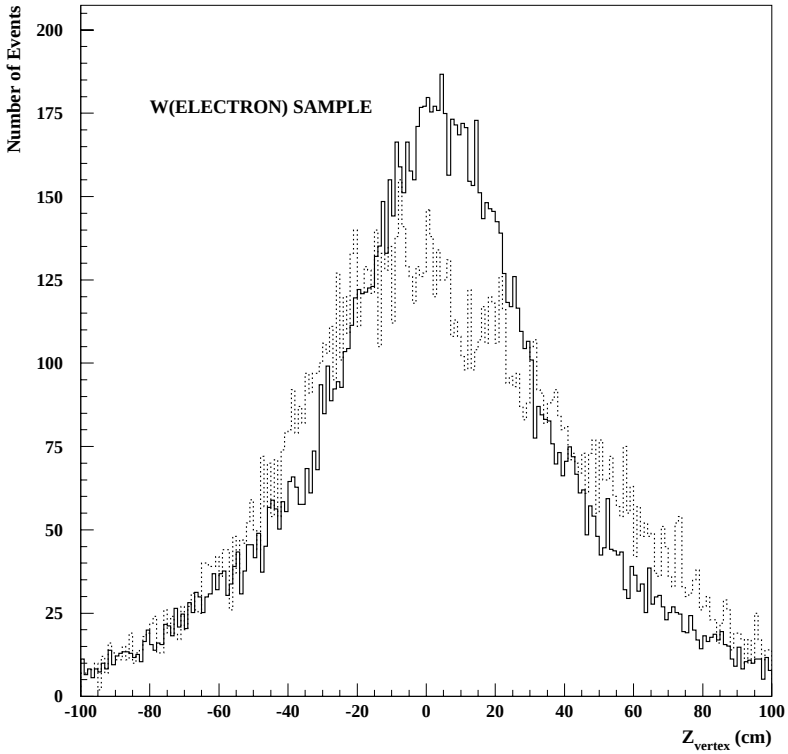

Figure 6.1: $z_{\rm vertex}$-*distribution for W (central electron) events from run 1B: (dotted line) events from* $55267 <$ run $\# < 61739$; *(solid line) events from* $61739 <$ run $\# < 71023$.

events from 61739 < run # < 71023. An asymmetric $z_{\rm vertex}$ distribution in combination with a left-right asymmetry of CTC tracking efficiency and left-right calorimeter efficiency (due to cracks) for vertex-shifted events creates a net charge-gap and angle-gap correlation asymmetry. In view of the fact that this problem was characteristic only of a localized subset of the data, i.e. runs with 55267 < run # < 61739, these runs were excluded from the analysis.

Table 6.1 summarizes the W(central electron/positron) selection cuts with the numbers of accepted events for the run 1A and 1B samples.

		Accepted Events	
No.	Cut	Run 1A	Run 1B
1	All processed events	39616	222568
2	Events from good runs	39616	222188
3	1 vertex	11836	44972
4	$\lvert z_{\rm vertex}\rvert < 60$ cm	11331	38516
5	$\mathrm{L_{shr}} < 0.2$	9897	23696
6	$\chi^2 < 10.0$	9547	19353
7	HAD/EM $< 0.055 + 0.00045E$(corrected)	8436	18679
8	$\mathrm{Isolation}_{(R=0.4)} < 0.1$	4587	16596
9	$0.5 < E/P < 2.5$	4516	15509
10	$\lvert DX\rvert < 1.5$ cm	4516	15509
11	$\lvert DZ\rvert < 3.0$ cm	4504	15309
12	$\lvert D0\rvert$ (beam constraint) < 0.2 cm	4504	13987
13	$\lvert z_{\rm event} - z_e\rvert < 5$ cm	4502	13972
14	$\lvert z0\rvert$ (beam constraint) < 60 cm	4502	13967
15	Curvature Significance > 2.0	4502	13967
16	Fiducial volume	4042	12476
17	Gamma conversion	2965	11991
18	Only 1 good electron	2817	11961
19	P_T (beam constraint) > 15 GeV/c	2097	9680
20	E_T (corrected) > 20 GeV	1904	9672
21	$\not\!\!E_T > 20$ GeV	1368	9636
22	$\lvert\eta_e\rvert < 1.1$	1363	9596
23	$40 < M_T^W < 120$ GeV/c^2	1350	9527
24	61739 < run # < 71023		6896

Table 6.1: *Runs 1A and 1B W Central Electron/Positron Selection.*

6.1.2 Detector Effects

Energy Threshold Selection

Since we detect particles by measuring deposited energy in the calorimeter above a certain threshold, by "rapidity gap" we do not mean a region of rapidity without any particles, but a region without particles as defined for the purpose of this analysis. The term "particle" is defined as a calorimeter tower or a cluster of towers above a given energy threshold. The energy threshold for calorimeter towers was chosen as low as possible in order to maintain a low level of non-diffractive background in the sample of rapidity gap events, but high enough to eliminate contribution from noise. The tower threshold was studied using a totally unbiased beam-beam crossing sample of events recorded in the same runs as the W sample.

Calorimeter Noise

A sample of ~ 98000 trigger-unbiased events was obtained by triggering on beam-beam crossings only. Events with no-vertex were chosen using the same vertex definition as in the W sample. Figure 6.2 shows the electromagnetic transverse energy of calorimeter towers as a function of η. The η-binning on the plot ($\Delta\eta = 0.1$) corresponds to the η-segmentation of the CDF calorimeters. Similar distributions for the hadronic and total tower E_T are presented in Figures 6.3 and 6.4. In order to choose the appropriate tower E_T threshold, we studied the fraction of events with tower hits above a given E_T threshold for each type of the CDF calorimeters. Table 6.2 shows the results of the measurement for five different tower E_T thresholds. As follows from the table, the 200 MeV tower E_T cut, where the fraction of events with tower hits above the threshold in the forward region falls to the level of a few percent, represents the best choice. While the transverse energy is an important

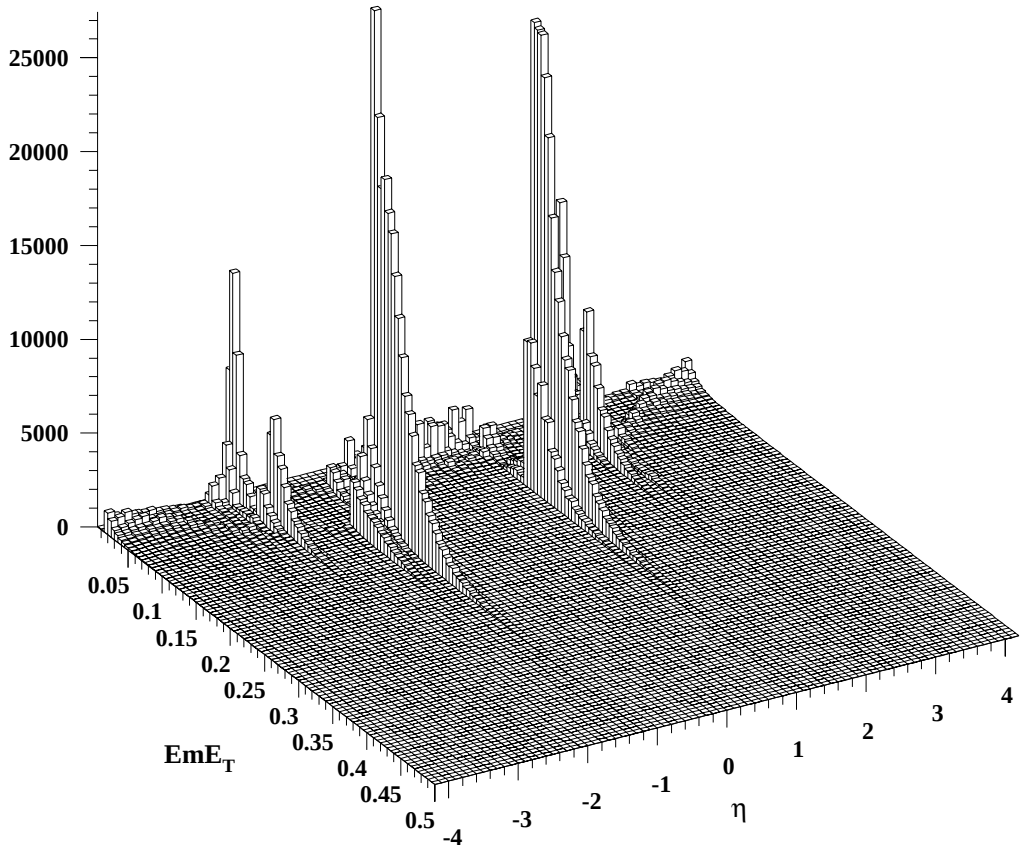

Figure 6.2: *Electromagnetic tower E_T versus η.*

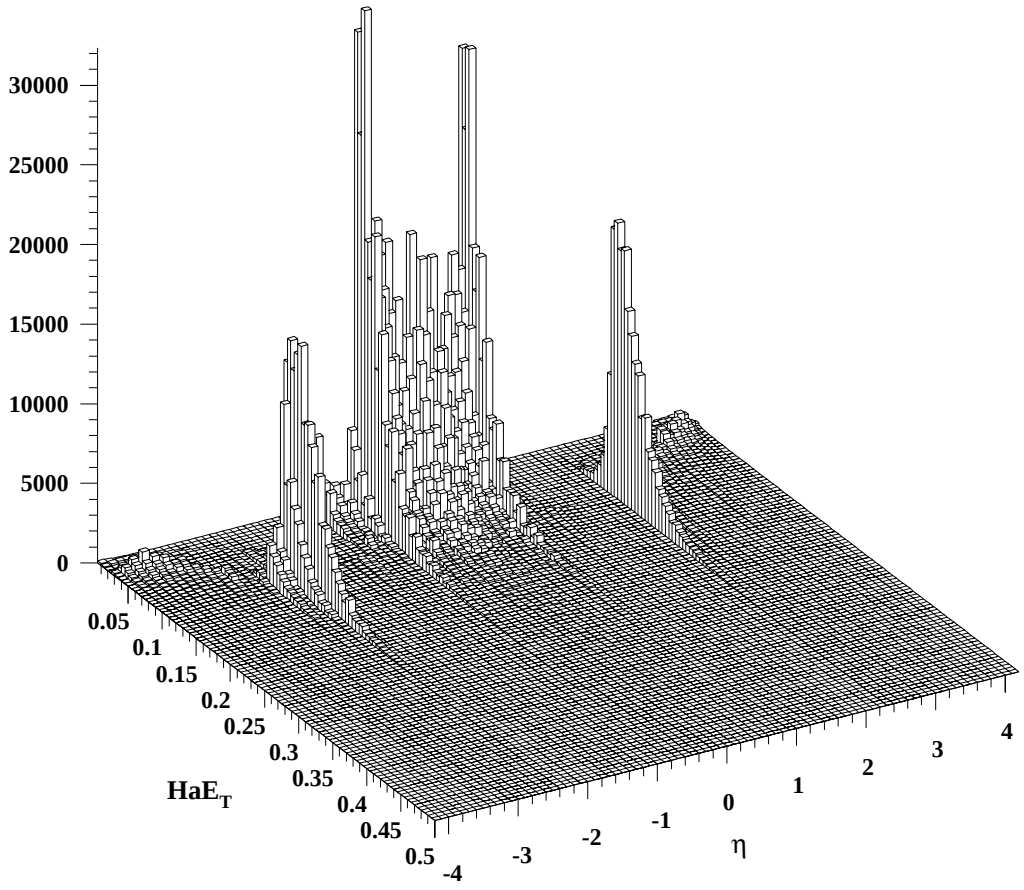

Figure 6.3: *Hadronic tower E_T versus η.*

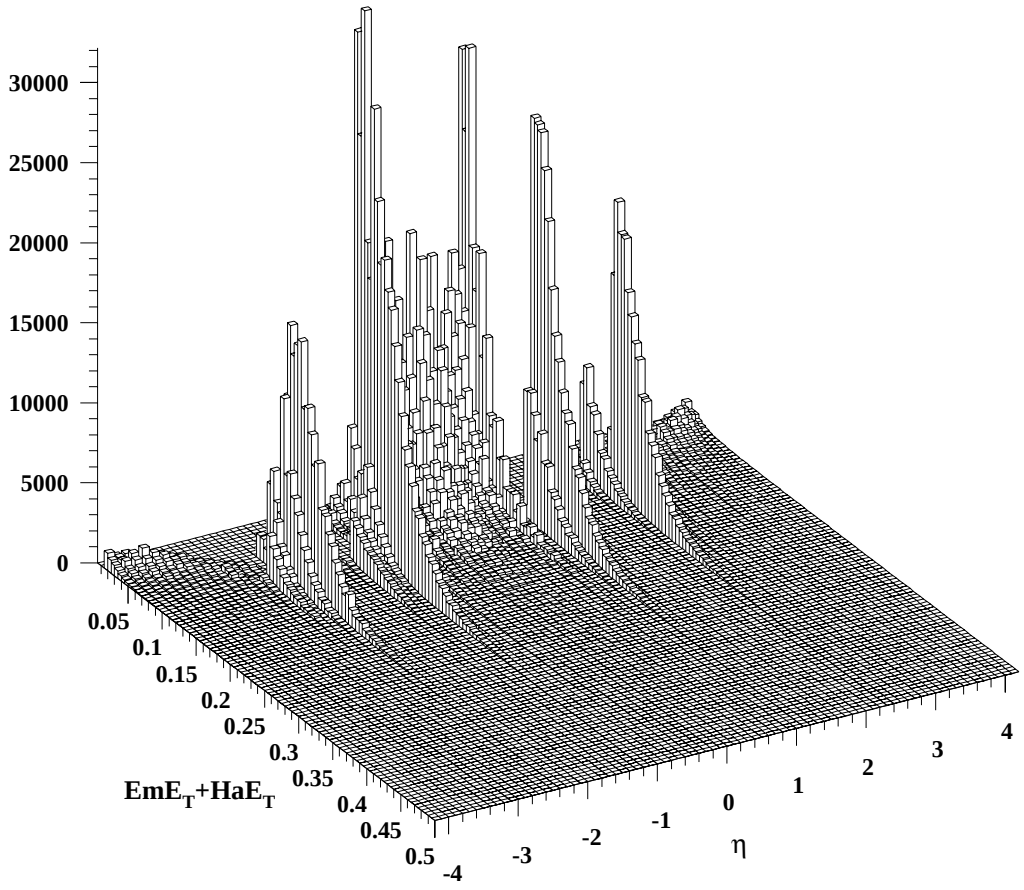

Figure 6.4: *Tower E_T versus η.*

system	tower type	η-region	fraction of events with tower hits above E_T threshold, (%)				
			100 MeV	150 MeV	**200 MeV**	250 MeV	300 MeV
CEM	0	[-0.72 , 0.00]	2.4	0.8	**0.8**	0.5	0.5
	0	(0.00 , 0.72]	1.3	1.3	**0.8**	0.3	0.3
	1	[-0.92 ,-0.72)	0.0	0.0	**0.0**	0.0	0.0
	1	(0.72 , 0.92]	0.5	0.3	**0.3**	0.3	0.3
	2	[-1.10 ,-0.92)	52.9	11.6	**2.9**	0.8	0.3
	2	(0.92 , 1.10]	73.7	24.2	**6.6**	1.6	0.3
PEM	3	[-1.20 ,-1.10)	91.6	48.4	**11.8**	2.9	0.5
	3	(1.10 , 1.20]	93.6	50.5	**14.5**	2.4	0.3
	4	[-1.32 ,-1.20)	24.5	1.3	**0.5**	0.3	0.3
	4	(1.20 , 1.32]	38.7	5.3	**0.5**	0.3	0.3
	5	[-1.41 ,-1.32)	10.0	1.8	**0.8**	0.8	0.3
	5	(1.32 , 1.41]	14.5	1.1	**0.0**	0.0	0.0
	6	[-2.22 ,-1.41)	6.8	0.8	**0.0**	0.0	0.0
	6	(1.41 , 2.22]	9.2	2.1	**0.8**	0.8	0.5
	7	[-2.31 ,-2.22)	3.2	0.5	**0.0**	0.0	0.0
	7	(2.22 , 2.31]	3.7	0.5	**0.0**	0.0	0.0
	8	[-2.40 ,-2.31)	1.6	1.1	**0.8**	0.5	0.5
	8	(2.31 , 2.40]	3.4	2.1	**1.3**	1.3	0.8
FEM	9	[-4.20 ,-2.40)	7.4	5.3	**4.2**	2.1	1.8
	9	(2.40 , 4.20]	7.9	5.8	**4.5**	3.4	1.6
CHA	0	[-0.72 , 0.00]	49.2	27.4	**17.1**	10.3	6.1
	0	(0.00 , 0.72]	43.9	24.4	**15.8**	10.5	5.8
	1	[-0.92 ,-0.72)	20.5	6.1	**3.2**	2.1	1.1
	1	(0.72 , 0.92]	19.7	7.6	**3.2**	1.3	0.8
	2	[-1.10 ,-0.92)	2.4	1.1	**0.3**	0.0	0.0
	2	(0.92 , 1.10]	5.3	1.6	**0.8**	0.5	0.3
WHA	3	[-1.20 ,-1.10)	2.1	1.3	**0.8**	0.8	0.3
	3	(1.10 , 1.20]	1.3	0.8	**0.5**	0.5	0.5
	4	[-1.32 ,-1.20)	1.6	0.5	**0.3**	0.3	0.0
	4	(1.20 , 1.32]	1.3	0.5	**0.0**	0.0	0.0
PHA	5	[-1.41 ,-1.32)	2.1	0.5	**0.5**	0.5	0.5
	5	(1.32 , 1.41]	3.2	0.8	**0.3**	0.3	0.3
	6	[-2.22 ,-1.41)	2.1	1.8	**1.8**	1.1	0.8
	6	(1.41 , 2.22]	3.4	2.6	**1.6**	1.6	0.8
	7	[-2.31 ,-2.22)	—	—	—	—	—
	7	(2.22 , 2.31]	—	—	—	—	—
	8	[-2.40 ,-2.31)	45.8	20.0	**3.9**	1.6	1.3
	8	(2.31 , 2.40]	57.4	14.2	**5.3**	1.8	0.5
FHA	9	[-4.20 ,-2.40)	35.5	9.8	**5.8**	3.9	3.2
	9	(2.40 , 4.20]	38.4	13.9	**9.2**	6.3	4.2

Table 6.2: *Fraction of events with tower hits above a given E_T threshold for different CDF calorimeters and tower types.*

characteristic of a high-energy process, calorimeter noise is characterised by the total energy rather than E_T. As a result, the E_T at a constant noise level decreases with increasing η. This is clearly seen in Figure 6.5, where the plot of Figure 6.4 is shown as a box-diagram. The dashed lines drawn in the regions confined by $2.4 < |\eta| < 4.2$ correspond to a constant energy of 1.5 GeV. The constant energy threshold for forward calorimeter towers leads to an overall smaller E_T cut, thus increasing the discrimination against non-diffractive "gaps" and thereby rendering the technique for tagging diffraction more sensitive. The actual tower E_T threshold used in this analysis as a function of η is represented by the solid curve in Figure 6.5. The curve corresponds to a constant 200 MeV E_T threshold for most of the central and plug calorimeter towers, while taking into account more noisy edge cells. The forward calorimeter tower E_T threshold is defined by a two-line approximation of the η-dependence of the constant energy noise, $E \approx 1.5$ GeV, which also takes into account the higher noise level in the calorimeter cells close to the beam pipe ($|\eta| > 3$). Presumably, this higher noise is due to the fact that the beam-beam crossing sample may also contain beam-gas events, interactions of the beam halo with the beam pipe, or low multiplicity diffractive and double-diffractive events without reconstructed vertex occurring during the beam crossing time. The exact definition of the described tower E_T cut is given in Table 6.3.

η region	E_T threshold (GeV)
$\lvert\eta\rvert < 1.1$	$E_T = 0.2$
$1.1 < \lvert\eta\rvert \leq 1.5$	$E_T = 0.45 * \sin(2\arctan(\exp(-\eta)))$
$1.5 < \lvert\eta\rvert \leq 2.3$	$E_T = 0.2$
$2.3 < \lvert\eta\rvert \leq 3.0$	$E_T = -0.143\lvert\eta\rvert + 0.579$
$3.0 < \lvert\eta\rvert \leq 4.2$	$E_T = -0.0625\lvert\eta\rvert + 0.3375$

Table 6.3: *The definition of the tower E_T cut.*

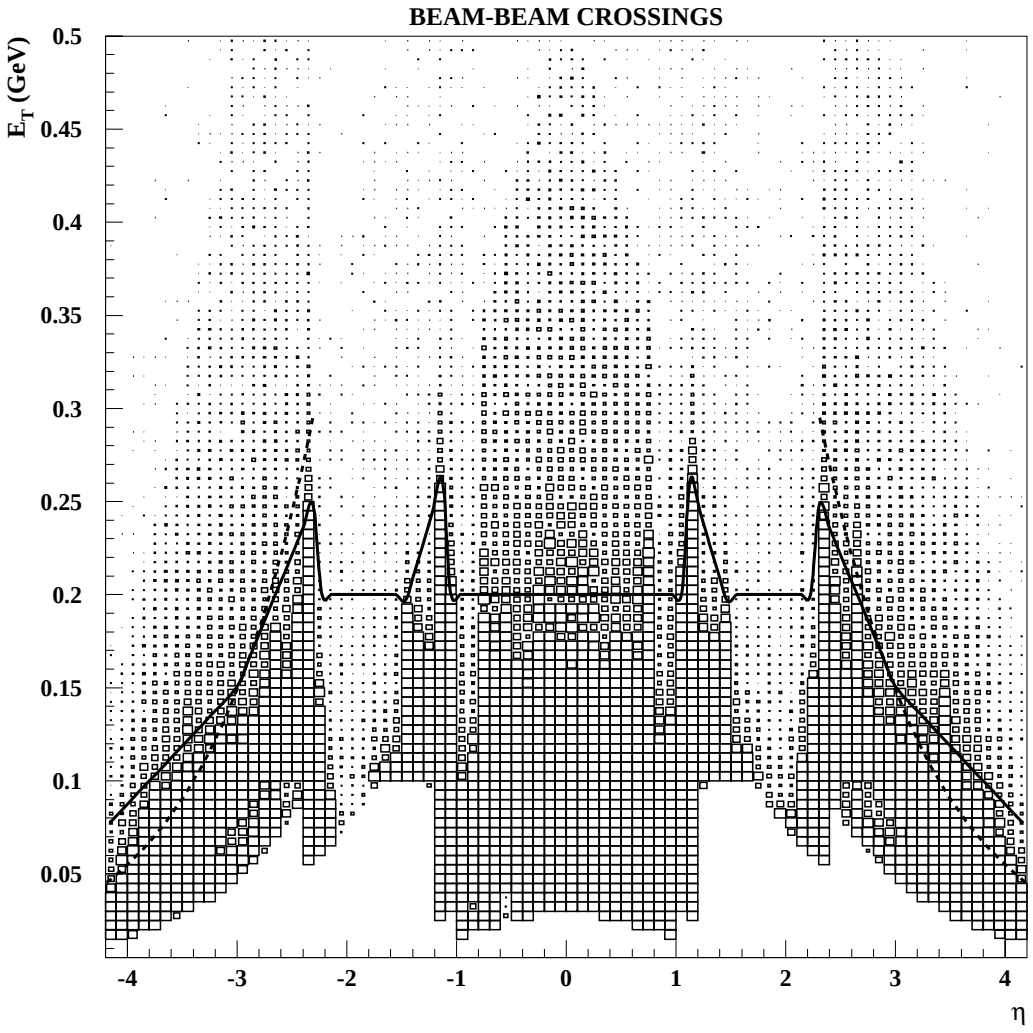

Figure 6.5: *The E_T threshold used in the analysis (solid line) as a function of η, superimposed on a scatter plot of E_T versus η for beam-beam crossings; the dashed lines in the regions $2.4 < |\eta| < 4.2$ represent the E_T versus η for fixed energy $E = 1.5$ GeV.*

Gap Survival Probability

The rapidity gap of a diffractive W event would not survive if a tower in the gap region happened to be above threshold. Using the beam-beam crossing sample, the gap survival probability was studied by calculating the fraction of events with forward calorimeter towers ($2.4 < |\eta| < 4.2$) above the E_T threshold.

Figure 6.6 shows the probability distribution for the number of forward calorimeter towers above the E_T threshold in the regions $-4.2 < \eta < -2.4$ (top plot) and $2.4 < \eta < 4.2$ (bottom plot). The average gap survival probability evaluated from the first bins of these distributions was found to be 87.5%.

6.1.3 Simulation of Detector Response

For simulation of the detector response to high-P_T central electrons/positrons from a W-boson decay we use the QFL detector simulation program [50], which has been proven to work well for high-P_T particles and jets. However, it is well known within CDF that the energy calibration of the calorimeters does not hold for low-P_T particles. In the central region, where the calorimetric energy of charged particles can be compared with the momentum measured by the CTC, it was found that for momenta of about 1 GeV and below the value obtained from the calorimeters is about 60% of the CTC measured momentum [51]. In addition to this non-linearity, energy loss in the cracks of the calorimeters clearly lowers the measured energy in these areas. Since a "rapidity gap" is defined as a region of rapidity with no particles above a given threshold, the detector must be well calibrated if comparisons with MC simulations are to be meaningful. In this analysis, the calculated acceptance becomes smaller if the energy threshold used in the MC simulation is smaller than that applied to the data, which is the case if the "detector energy" is smaller than

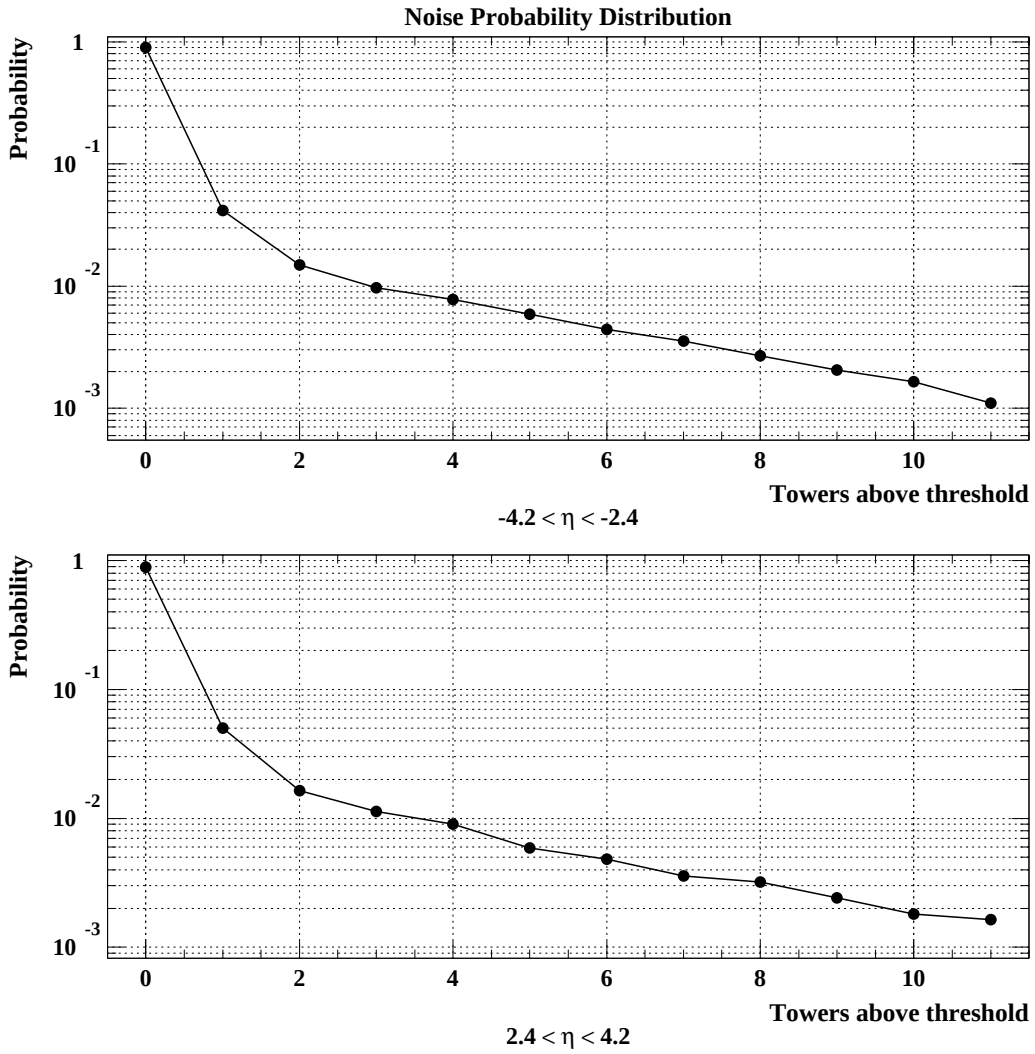

Figure 6.6: *The probability distribution for the number of towers above the E_T threshold in the regions $-4.2 < \eta < -2.4$ and $2.4 < \eta < 4.2$ for the beam-beam crossing event sample.*

the actual energy of the particle. This smaller acceptance yields a larger diffractive to non-diffractive W production ratio. Below, in a series of steps, we present the method that we developed for simulation of the detector response to low-P_T particles from the underlying event in W production and the results we obtained.

We start from the comparison of the E_T, $dn/d\eta$ and multiplicity distributions for the data and non-diffractive W MC events after applying the E_T cut described in section 6.1.2. Figure 6.7 shows that the E_T-distribution for data towers is sharper than for MC particles and that the data and the MC $dn/d\eta$ distributions do not match. The peculiar shape of the E_T distributions below 200 MeV is the result of the constant energy threshold applied to the forward calorimeter towers. From the study of the trigger-unbiased events we find that the noise level is too small to explain the difference in the spectrum between data and MC. Figure 6.8 shows that the data (towers) and MC (particles) multiplicity distributions also do not match. The fraction of events with a gap in data is larger than in the MC sample.

We note here that since a particle can deposit energy above the E_T threshold in more than one calorimeter tower, especially in the forward region where the granularity of the towers for the constant $\Delta\eta$ segmentation becomes finer, the calorimeter towers have to be clustered in order for the comparison between data and MC to be valid.

Clustering of Calorimeter Towers

The adjacent calorimeter towers were clustered with an algorithm using a radius of 15 cm around a "seed" tower. Prior to clustering, calorimeter towers to be included in a cluster were required to be above the tower E_T threshold. The cluster radius was chosen to correspond approximately to the average transverse dimension of a hadron shower in the calorimeter medium. Figures 6.9 and 6.10 compare the

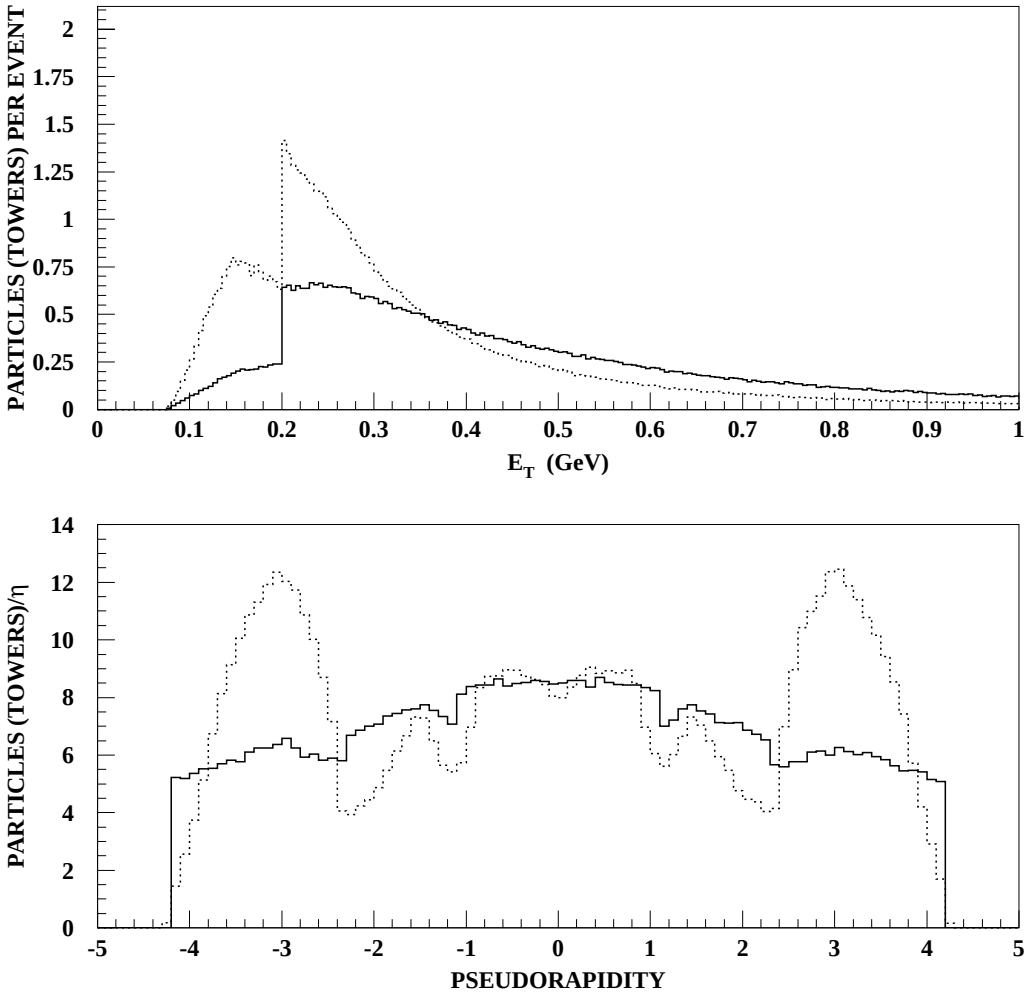

Figure 6.7: *E_T and η-distributions for data towers (dotted) and MC particles (solid).*

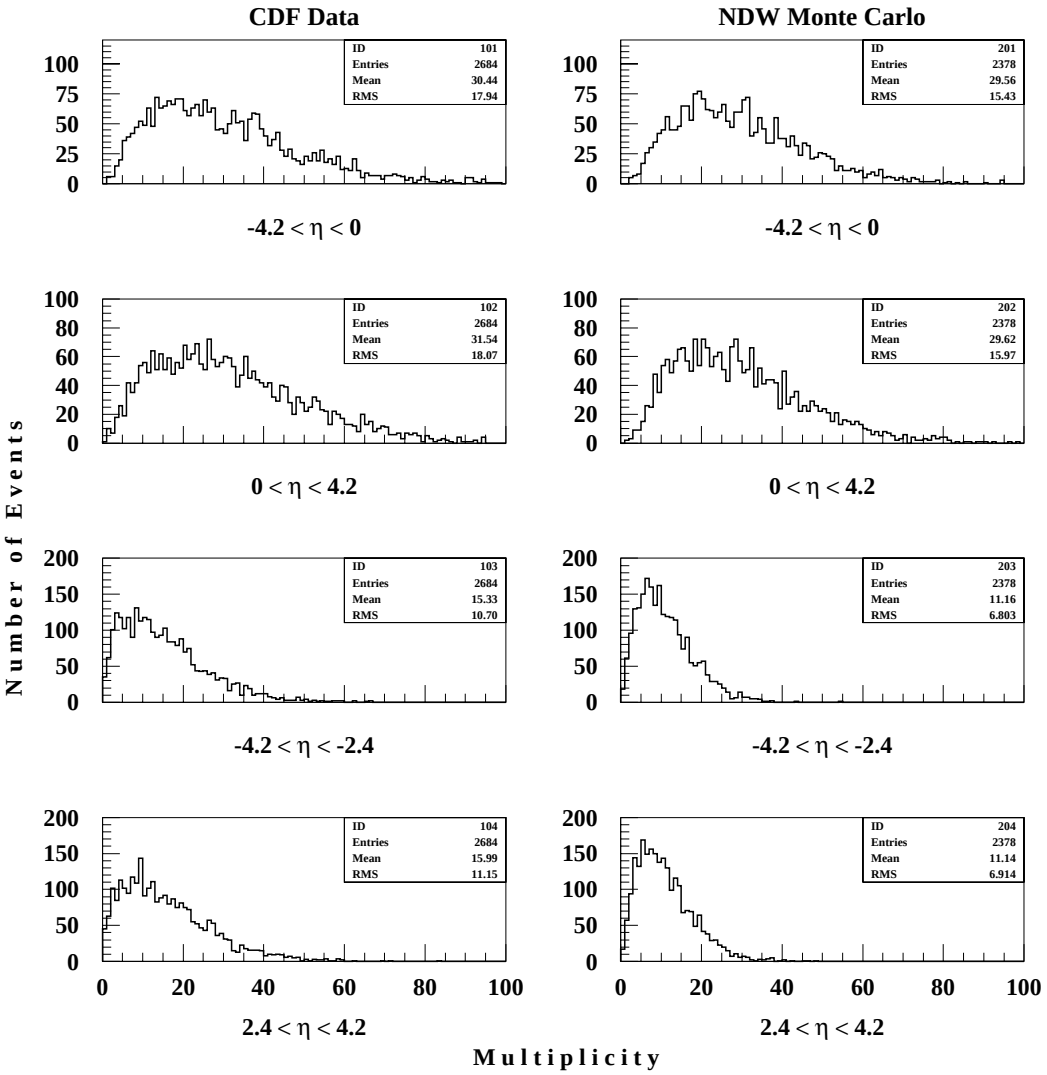

Figure 6.8: *Data (towers) and non-diffractive Monte Carlo (particles) multiplicity distributions.*

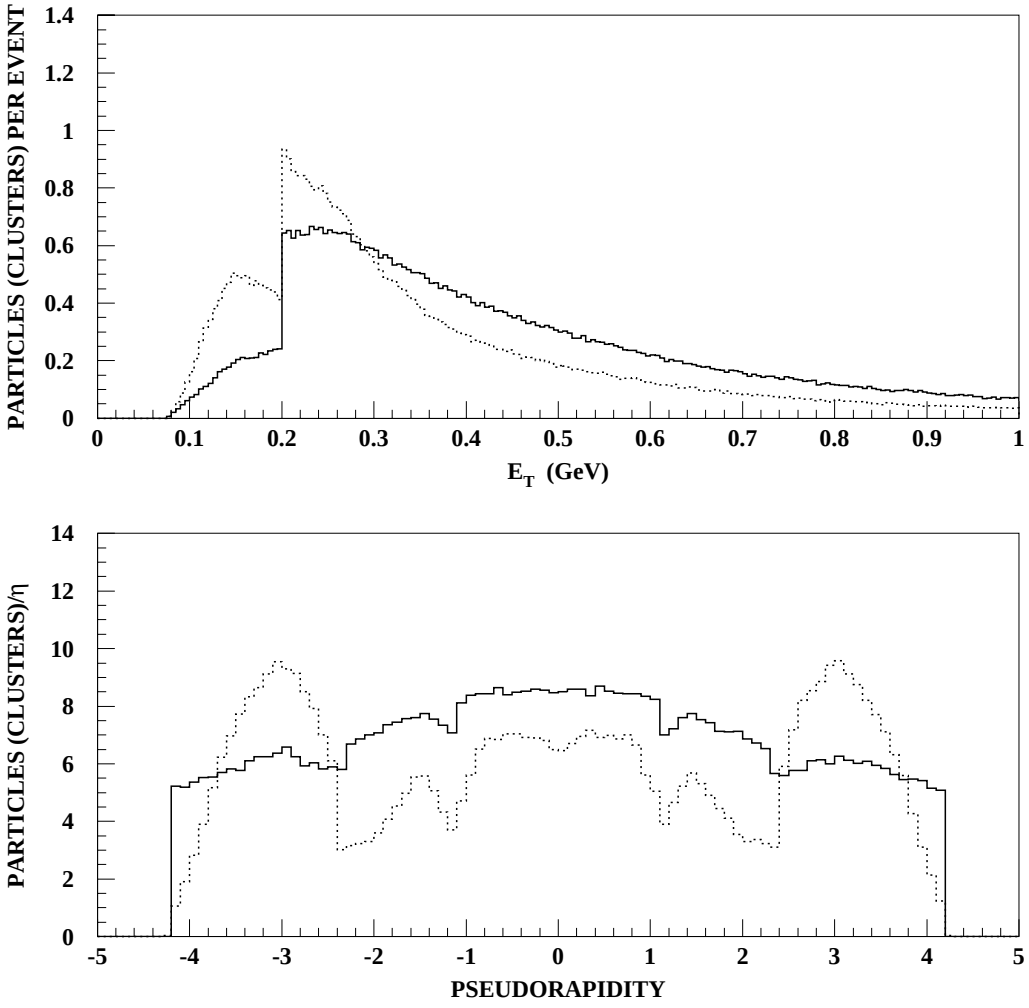

Figure 6.9: *E_T and $dn/d\eta$ distributions for data tower clusters (dotted) and MC particles (solid).*

E_T, $dn/d\eta$ and multiplicity distributions for data tower clusters and MC particles. As seen, the distributions still do not match.

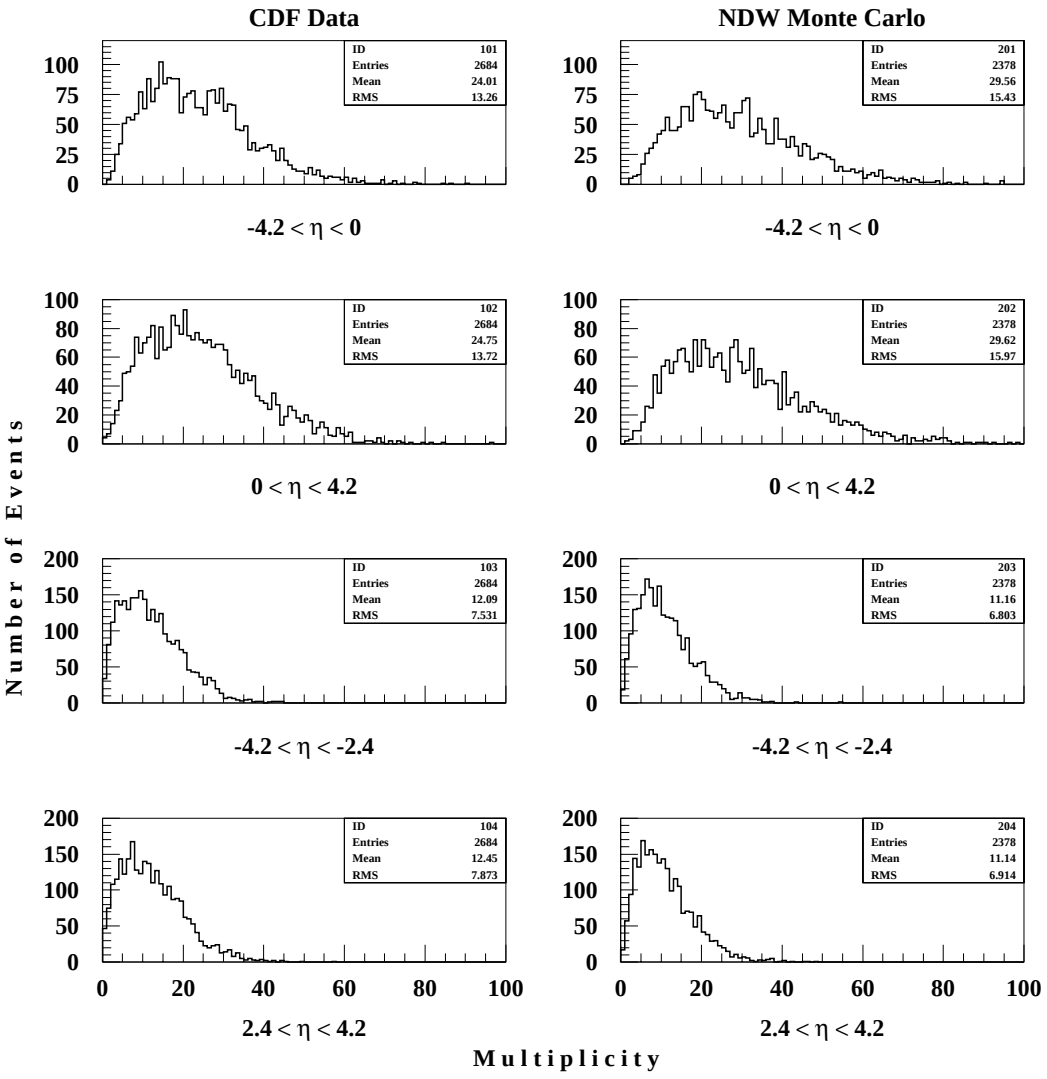

Figure 6.10: *Data (tower clusters) and non-diffractive MC (particles) multiplicity distributions.*

Simulation of Calorimeter Response to Low-P_T Particles

To correct the MC P_T spectrum for detector effects at low E_T, we argue that the reason why the clustered-tower E_T spectra, after noise subtraction, are

still sharper than the MC generated spectra is that the detector energy is shifted downwards either by non-linearities or by energy leakage, particularly near the cracks between calorimeters. In so arguing, we assume that the MC generates the correct P_T spectrum and believe that this is a rather safe and non-controversial assumption. The simplest way to correct for these effects is to multiply the MC generated P_T by a coefficient, C, and compare the resulting energy spectrum with the E_T spectrum of the data, then change C and compare again until a match is achieved. In looking for a good match, we also take into account how well the total integrated multiplicity matches. This procedure was applied as a function of η for bins of size $\Delta\eta = 0.1$. We obtained good matches for all η-bins, except for the bins corresponding to the forward calorimeter, where we had to introduce an offset S in addition to the factor C.

The next three Figures, 6.11, 6.12 and 6.13, illustrate how well this procedure works. In each figure, the transverse energy spectrum is shown for (a) the data (dotted) and unmodified MC (solid), (b) the modified MC, (c) the noise, and (d) the data and the modified MC+noise. Using the modified MC+noise, we then check how well it represents the E_T, $dn/d\eta$, and the clustered multiplicity distributions of the data. Figure 6.14 displays the E_T and $dn/d\eta$ distributions for data tower clusters and MC particles after correcting the MC for energy loss and detector noise. The multiplicity distributions in Figure 6.15 now match both in the average value and in the width. The particle P_T correction coefficients and offsets are presented in Table 6.4.

We note here that this correction procedure is valid for the low P_T region only. It cannot be continued to the high-P_T region, as the way this would happen depends on the η-region, e.g. it would be different for the center of a detector, where the effect is due to non-linearity, or for the edge of a detector, where both

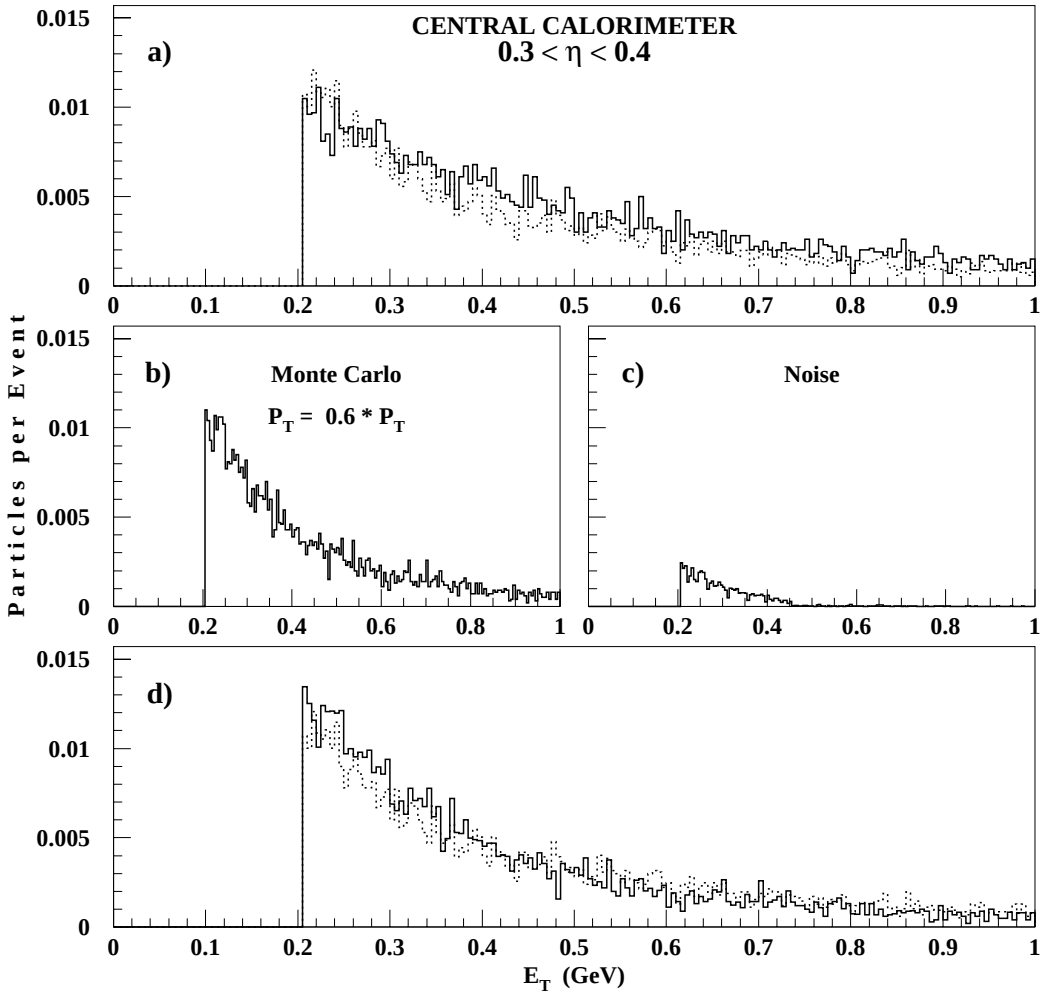

Figure 6.11: *Comparison of Monte Carlo (particles, solid line) and data (tower clusters, dotted line) E_T-distributions in the central calorimeter region: (a) before MC correction; (b) after correction applied to MC; (c) noise added to MC; (d) data versus corrected MC including noise.*

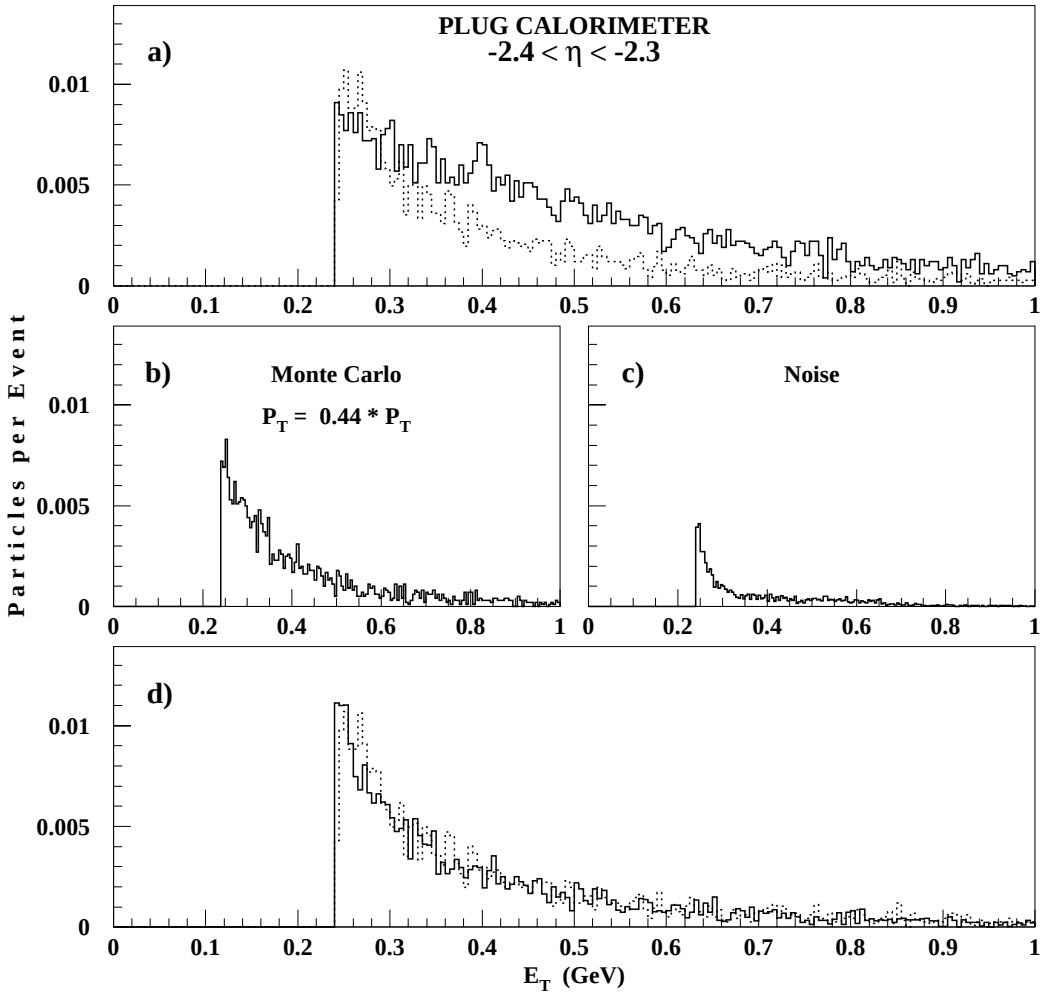

Figure 6.12: *Comparison of Monte Carlo (particles, solid line) and data (tower clusters, dotted line) E_T-distributions in the plug calorimeter region: (a) before MC correction; (b) after correction applied to MC; (c) noise added to MC; (d) data versus corrected MC including noise.*

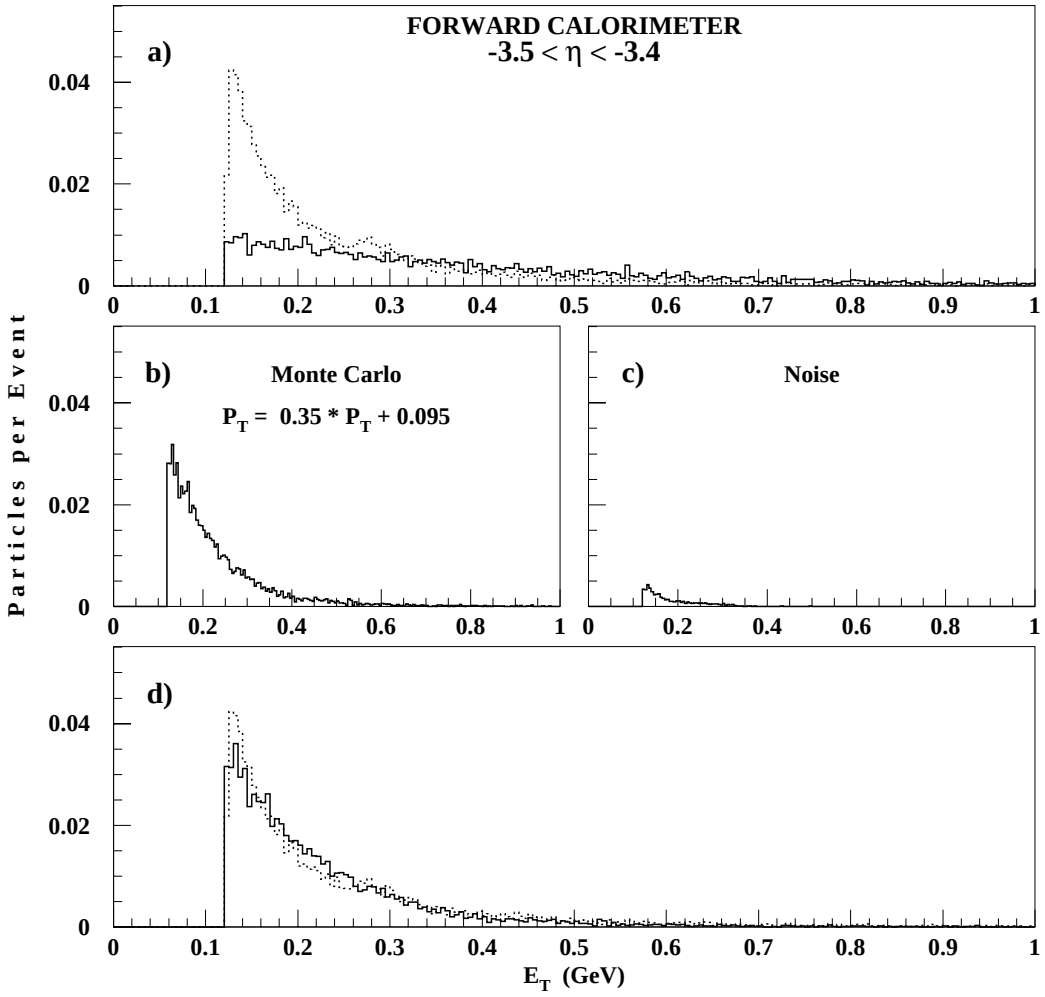

Figure 6.13: *Comparison of Monte Carlo (particles, solid line) and data (tower clusters, dotted line) E_T-distributions in the forward calorimeter region: (a) before MC "correction"; (b) correction applied to MC; (c) noise added to MC; (d) data versus corrected MC including noise.*

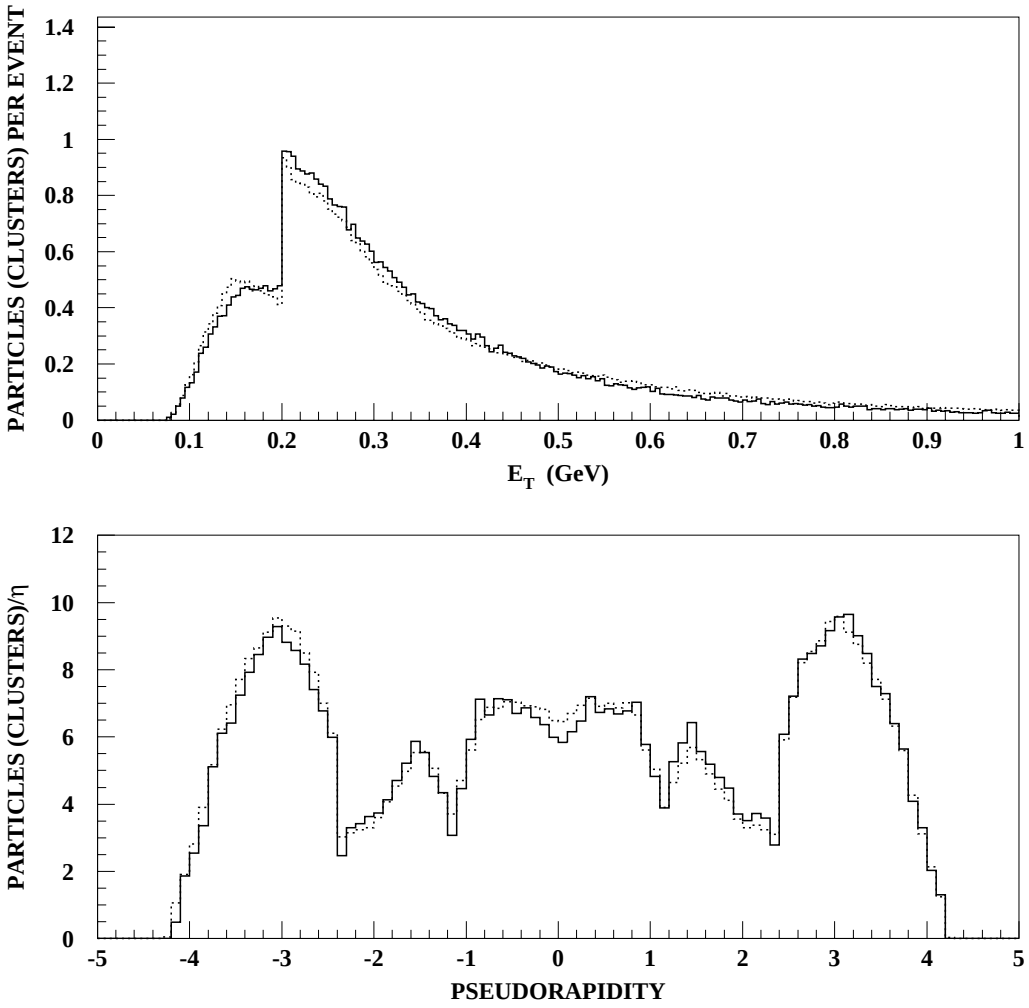

Figure 6.14: *Comparison of Monte Carlo (particles, solid line) and data (tower clusters, dotted line)* E_T *and* $dn/d\eta$ *distributions after correcting the MC for energy loss and detector noise.*

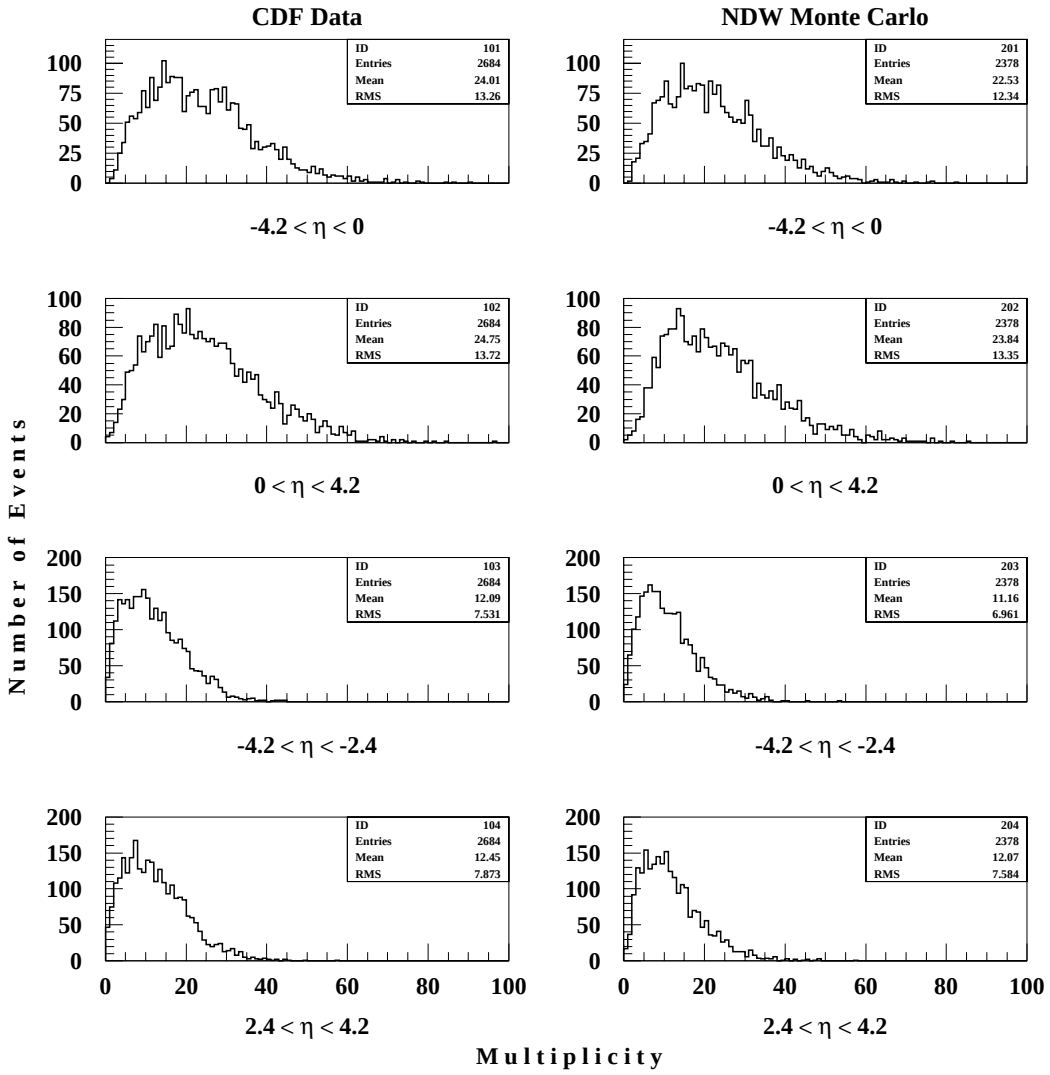

Figure 6.15: *Multiplicity distributions for data (tower clusters) and MC (particles) after P_T correction.*

No.	C	S	No.	C	S
1	0.10	0.000	43	0.49	0.000
2	0.21	0.000	44	0.49	0.000
3	0.28	0.000	45	0.54	0.000
4	0.25	0.030	46	0.60	0.000
5	0.31	0.055	47	0.54	0.000
6	0.29	0.075	48	0.57	0.000
7	0.36	0.080	49	0.58	0.000
8	0.35	0.095	50	0.57	0.000
9	0.31	0.110	51	0.63	0.000
10	0.40	0.110	52	0.51	0.000
11	0.47	0.120	53	0.46	0.000
12	0.46	0.125	54	0.52	0.000
13	0.46	0.120	55	0.61	0.000
14	0.50	0.125	56	0.60	0.010
15	0.60	0.120	57	0.56	0.025
16	0.57	0.115	58	0.54	0.025
17	0.61	0.100	59	0.50	0.025
18	0.61	0.080	60	0.46	0.035
19	0.44	0.000	61	0.43	0.035
20	0.43	0.000	62	0.40	0.015
21	0.43	0.000	63	0.40	0.015
22	0.43	0.000	64	0.40	0.025
23	0.46	0.000	65	0.40	0.025
24	0.50	0.000	66	0.46	0.015
25	0.54	0.000	67	0.59	0.095
26	0.59	0.000	68	0.64	0.110
27	0.57	0.025	69	0.57	0.135
28	0.60	0.000	70	0.51	0.135
29	0.58	0.000	71	0.48	0.135
30	0.51	0.000	72	0.51	0.140
31	0.41	0.000	73	0.49	0.135
32	0.41	0.000	74	0.49	0.130
33	0.52	0.000	75	0.48	0.130
34	0.62	0.000	76	0.33	0.110
35	0.58	0.000	77	0.34	0.095
36	0.56	0.000	78	0.32	0.090
37	0.59	0.000	79	0.30	0.080
38	0.58	0.000	80	0.31	0.065
39	0.57	0.000	81	0.28	0.040
40	0.54	0.000	82	0.19	0.040
41	0.51	0.000	83	0.23	0.000
42	0.50	0.000	84	0.16	0.000

Table 6.4: P_T correction coefficients and constant terms for each of the 84 bins in η.

non-linearity and energy leakage play a role.

Finally, the question arises whether the underlying event energy spectra for diffractive and non-diffractive W production are very different, which might put into question the application of this procedure to diffractive W events. Figure 6.16 shows that the two spectra are practically identical.

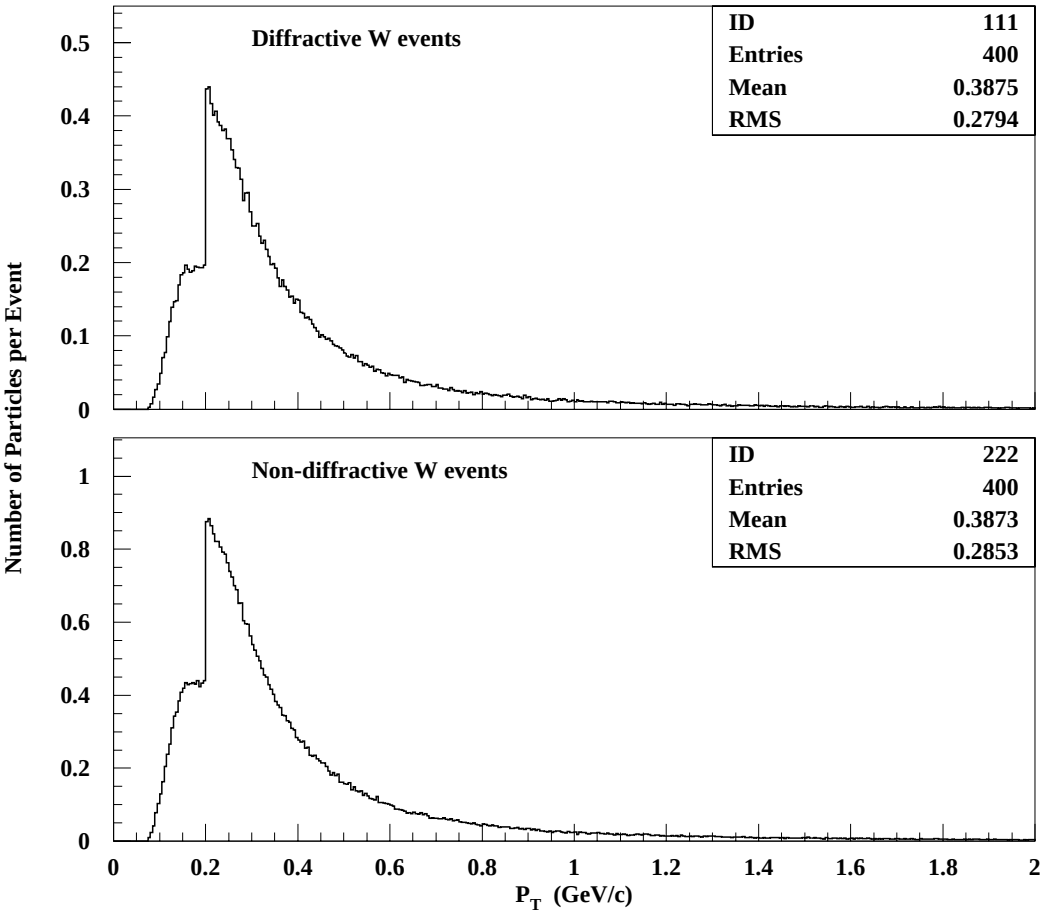

Figure 6.16: *Monte Carlo underlying event P_T spectra for diffractive and non-diffractive W-boson production.*

6.1.4 Extraction of the Signal

The diffractive W signal is extracted from the sample of 8246 W events using the correlation asymmetry analysis described in section 3.1. Diffractive W candidates are tagged by the requirement of a forward "rapidity gap" identified by low particle multiplicity in one of the η-regions $-5.9 < \eta < -3.2$ or $3.2 < \eta < 5.9$, which are covered by the CDF BBC scintillator arrays.

To improve separation of the signal from the non-diffractive background, we also examine the multiplicity distribution of towers above the energy threshold in the forward calorimeter adjacent to a given BBC. There is an overlap of about one unit of η between a BBC and the adjacent forward calorimeter, so that a significant correlation between BBC multiplicity and the forward calorimeter multiplicity is expected.

In Figure 6.17 the BBC multiplicity is plotted versus the adjacent forward calorimeter tower multiplicity for (angle⊗charge)-correlated (a) and (angle⊗charge)-anticorrelated (b) W data events. The accumulation of events at high BBC multiplicities on these plots is caused by saturation due to the coarse BBC segmentation. One can see an excess in the first few bins of the BBC and the forward calorimeter tower multiplicities for the (angle⊗charge)-correlated distribution, which is characteristic of a diffractive W signal (see section 6.1.7). Figure 6.18 shows the observed charge-gap and angle-gap correlations as a function of BBC multiplicity for events with a tower multiplicity, N_{towers}, less than 8 in the forward calorimeter adjacent to a given BBC. This cut on tower multiplicity is imposed to reduce the non-diffractive contribution to the signal on one hand, and to retain a large acceptance for diffractive events on the other hand. Figure 6.18a shows the (angle⊗charge)-correlated (solid) and anti-correlated (dotted) BBC multiplicities. The two distributions agree

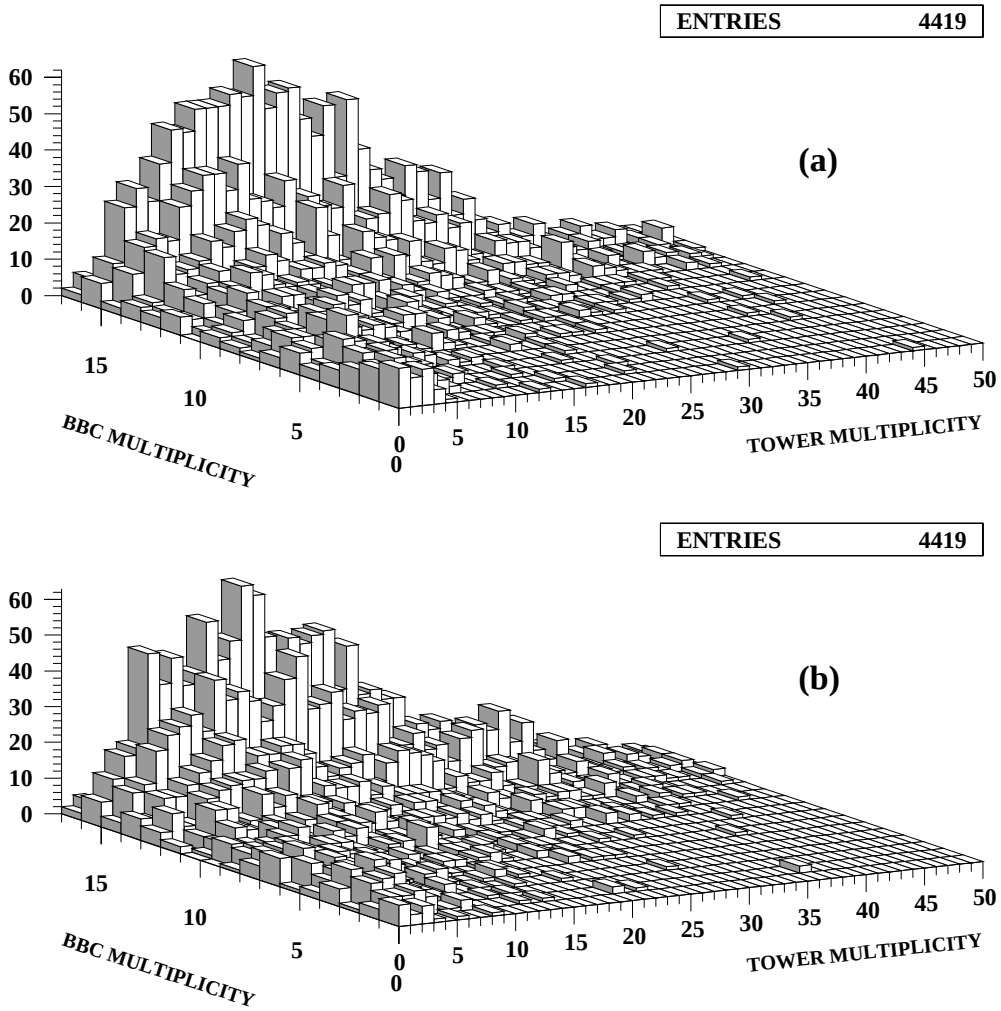

Figure 6.17: *BBC multiplicity versus adjacent forward calorimeter tower multiplicity (a) for (angle⊗charge)-correlated (a) and (b) for (angle⊗charge)-anticorrelated W events.*

well above the first three bins, but the correlated distribution (solid line) has a statistically significant excess in the first bin, consistent with the signature one expects for rapidity gap events from diffractively produced W's. This excess can be seen more clearly in Figure 6.18b, in which we plot the bin-by-bin *asymmetry* (difference divided by sum) of the distributions of Figure 6.18a. As expected for diffraction, the signal is also present in the individual angle-gap and charge-gap asymmetries (Figures 6.18c,d).

6.1.5 The Statistical Significance of the Signal

The statistical significance of the diffractive W signal, which is seen as an excess in the first bin (zero multiplicity) of the angle-gap and charge-gap correlated over anticorrelated BBC multiplicity distributions (see Figure 6.19), is quantified by the smallness of the probability that the observed excess can be caused by a random fluctuation in the non-diffractive distributions, since Monte Carlo simulations show that there is no asymmetry expected between the correlated and anticorrelated distributions in non-diffractive W events.

The probability is evaluated using Poisson statistics. When the expected number for either correlated or for anticorrelated events is μ, the probability to obtain simultaneously more than N_1 correlated and less than N_2 anticorrelated events by random fluctuations is found by maximizing the expression (by varying μ)

$$P(\mu) \equiv P(n \geq N_1; n \leq N_2) = \sum_{n=N_1}^{\infty} \frac{\mu^n e^{-\mu}}{n!} \times \sum_{n=0}^{N_2} \frac{\mu^n e^{-\mu}}{n!} \qquad (6.2)$$

(Angle⊗Charge)-(Anti)Correlated Events

First, we consider the (angle⊗charge) doubly-(anti)correlated distributions, which are shown in Figure 6.19.

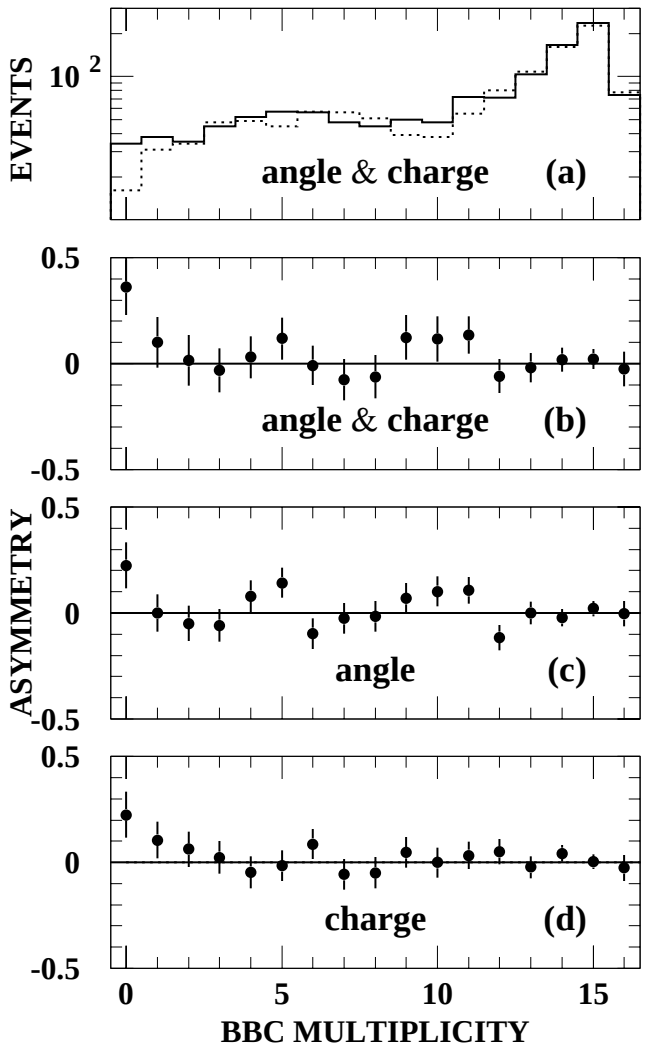

Figure 6.18: *Electron angle and/or charge correlated and anticorrelated distributions (see text) versus BBC multiplicity. In each case shown the asymmetry is defined as the bin-by-bin difference over the sum of the correlated and anticorrelated distributions.*

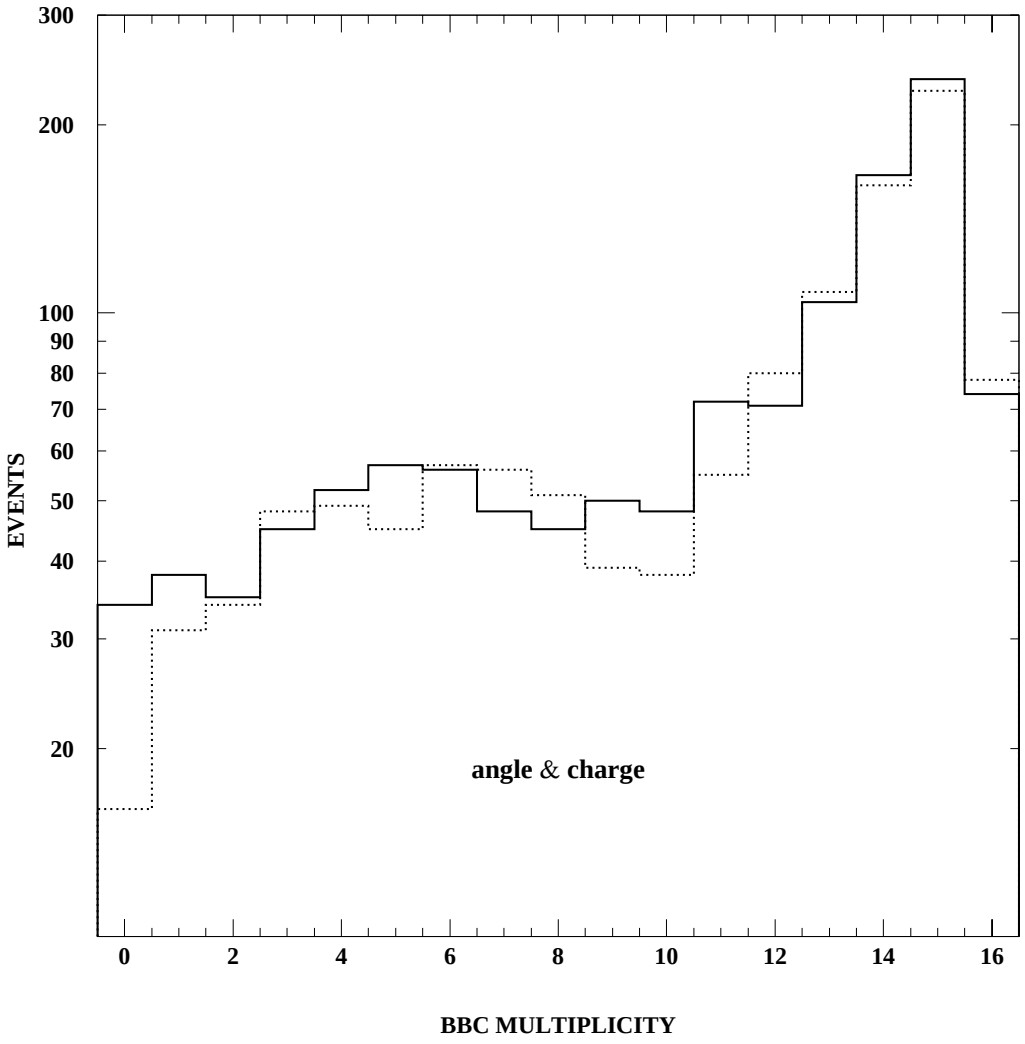

Figure 6.19: *Electron angle-gap and charge-gap doubly-correlated (solid) and anticorrelated (dashed) distributions versus BBC multiplicity.*

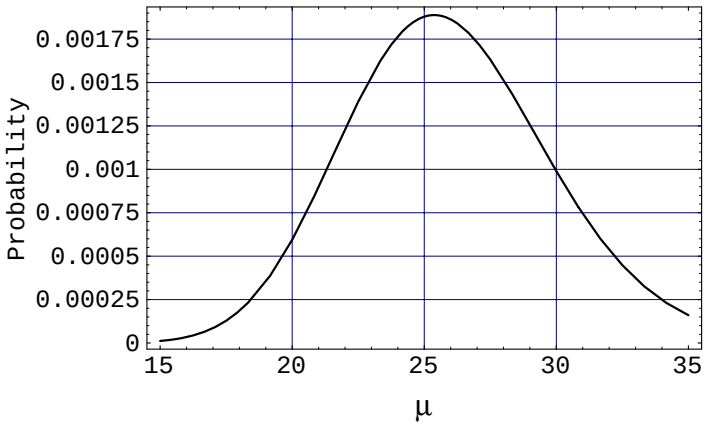

Figure 6.20: *Probability versus μ for (angle⊗charge)-(anti)correlated events.*

For this case, where $N_1 = 34$ and $N_2 = 16$, Figure 6.20 displays the probability evaluated using Eqn. (6.2) as a function of μ. The maximum probability is obtained for $\mu = 25.3$, which, as expected, is close to 25, the average number of correlated and anticorrelated events in the first BBC multiplicity bin. Hence, we find

$$P_{max} = P(25.3) = 1.9 \times 10^{-3},$$

which corresponds to 3.1σ of the normal distribution.

Angle and Charge (Anti)Correlated Events

An excess of correlated gap events is seen also in the individual angle-gap (anti)correlated and charge-gap (anti)correlated distributions (Figure 6.21). The probability that such an excess is due to simultaneous and independent random fluctuations of the corresponding non-diffractive distributions is obtained by maximizing the expression

$$P(\mu) = \sum_{n=N_1^a}^{\infty} \frac{\mu^n e^{-\mu}}{n!} \cdot \sum_{n=0}^{N_2^a} \frac{\mu^n e^{-\mu}}{n!} \times \sum_{n=N_1^c}^{\infty} \frac{\mu^n e^{-\mu}}{n!} \cdot \sum_{n=0}^{N_2^c} \frac{\mu^n e^{-\mu}}{n!} \qquad (6.3)$$

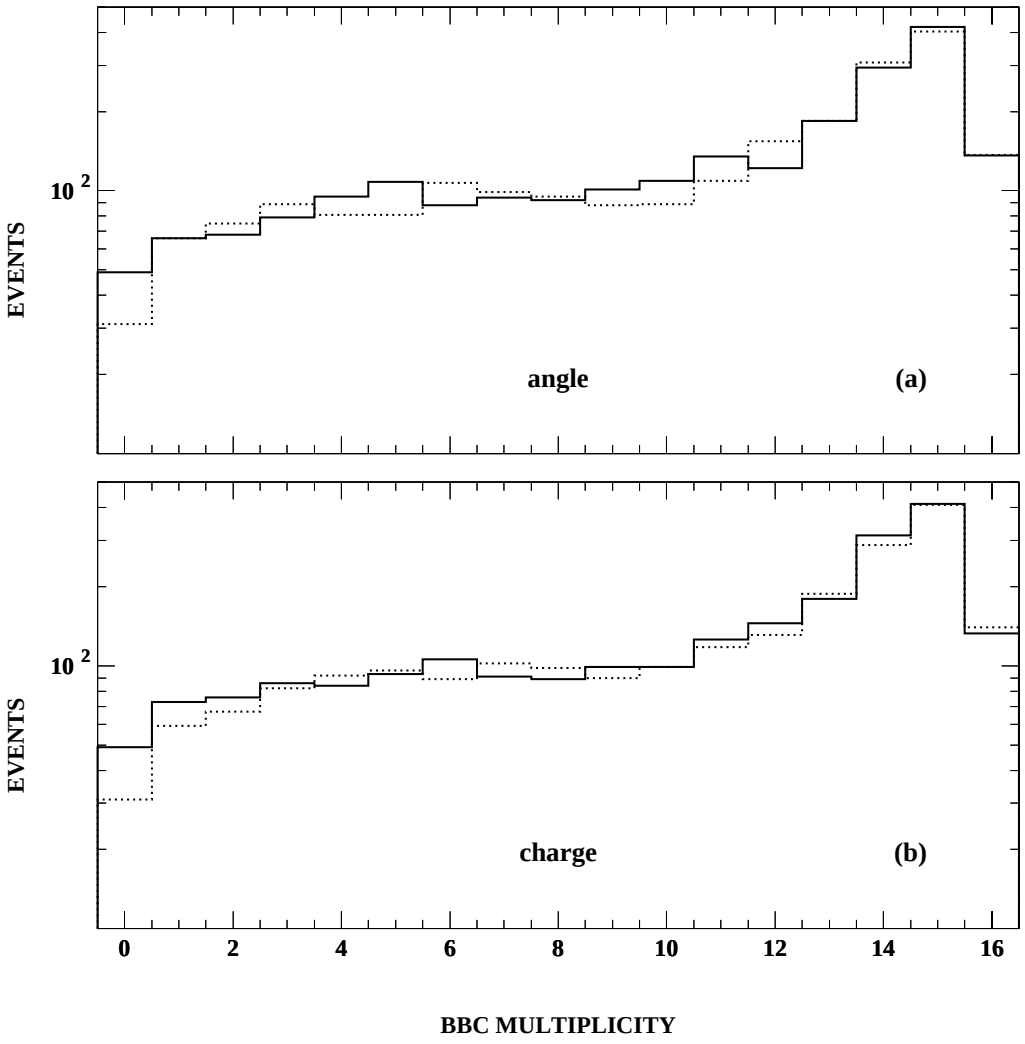

Figure 6.21: *Electron angle-gap and charge-gap correlated (solid) and anticorrelated (dashed) distributions versus BBC multiplicity.*

where N_1^a, N_1^c and N_2^a, N_2^c refer to the number of angle-gap and charge-gap correlated or anticorrelated events, respectively.

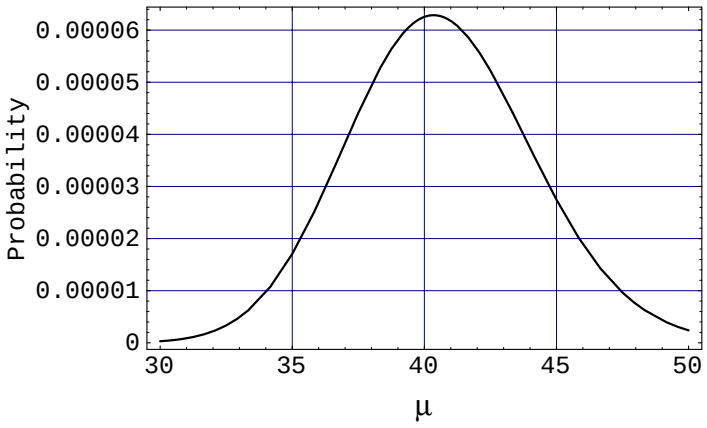

Figure 6.22: *Probability versus μ for angle and charge (anti)correlated events.*

In the first bins of the angle-gap correlated and anticorrelated distributions in Figure 6.21, there are 49 angle-gap correlated and 31 angle-gap anticorrelated events. The same happens to be the case for the charge-gap correlated and anticorrelated distributions. Figure 6.22 shows the probability as a function of μ. Maximizing the expression of Eqn. (6.3) we obtain

$$P_{max} = P(40.5) = 6.2 \times 10^{-5},$$

which corresponds to 4σ of the normal distribution. The value $\mu = 40.5$ that maximizes the probability is close to the average value of (49+31)/2=40 gap events.

This probability increases if the angle and charge of the leptons in non-diffractive events are correlated, even if the rapidity gaps are completely random. Our non-diffractive W MC sample of events with a gap contains 543 angle-gap correlated, 544 charge-gap correlated, and 290 (angle$\otimes$charge)-correlated events. For completely

uncorrelated charge and angle distributions, the number of expected (angle⊗charge)-correlated events would be (544+543)/4=272. The excess of (290-272)=18 events over the 272 expected is $(7 \pm 1.5)\%$. The effect of a 7% correlation can be taken into account in the probability in Eqn. (6.3) by assuming a 7% smaller excess in one of the two (data) distributions, the angle or the charge. This yields

$$P_{max} = 1.1 \times 10^{-4}$$

as the probability that the effect we observe is due to a simultaneous fluctuation in both the charge-gap and an angle-gap correlations of the non-diffractive distributions. This probability corresponds to 3.8σ of the normal distribution.

6.1.6 Ratio of Diffractive to Non-diffractive W-boson Production

In order to check for possible systematic effects due to BBC noise or inefficiencies that could distort the distributions at low BBC multiplicity bins and thereby give an incorrect value for the ratio of diffractive to non-diffractive W production, the ratio R in Eqn. (3.10) is evaluated using all events with a BBC multiplicity upper bound, N_B, and N_B is varied from zero to seven. Figure 6.23a shows the resulting R values, not corrected for BBC occupancy or one-vertex cut efficiency (see section 6.1.7). The fact that the ratio remains rather stable with increasing N_B indicates that the background subtracted at each value of N_B is angle-gap and charge-gap uncorrelated. The amount of the background being subtracted increases with increasing N_B, which results in larger statistical errors. To reduce the sensitivity of the result to the acceptance calculation, we retain as our signal the value

$$R = (1.03 \pm 0.46(stat))\%$$

of the $N_B = 2$ bin, where the acceptance is 81% (see Figure 6.23b) and varies relatively slowly with N_B (see section 6.1.7 for evaluation of the gap acceptance). To verify that the events in the signal region, which are expected to have significant diffractive contribution, are in fact "good" W events, we compared various characteristic distributions for W events from the signal region ($N_B = 2$, $N_{\text{towers}} < 8$) with corresponding distributions for the total W sample. Figure 6.24 shows that there is good agreement within available statistics between characteristics of the (angle⊗charge)-(anti)correlated W events from the signal region with ones from the total W(central electron/positron) sample.

6.1.7 Corrections

Gap Acceptance

The determination of the rate of diffractive W production requires knowledge of the diffractive acceptance, which is model dependent. For this analysis the acceptance is evaluated using POMPYT with a hard-quark pomeron structure, as justified in Chapter 5.

Figure 6.25 shows the correlation between the particle multiplicity in the pseudorapidity region $2.4 < \eta < 4.2$ (forward calorimeter) and in the adjacent BBC region $3.2 < \eta < 5.9$ for (angle⊗charge)-correlated (a) and (angle⊗charge)-anticorrelated (b) diffractive W events generated with POMPYT using a hard-quark structure for the pomeron. A significant difference is observed between the number of (angle⊗charge)-correlated and (angle⊗charge)-anticorrelated events. The signal is concentrated in the first few bins of both BBC and forward calorimeter.

The corresponding lego-plots for non-diffractive PYTHIA W events are presented in Figure 6.26. No difference between the number of (angle⊗charge)-correlated

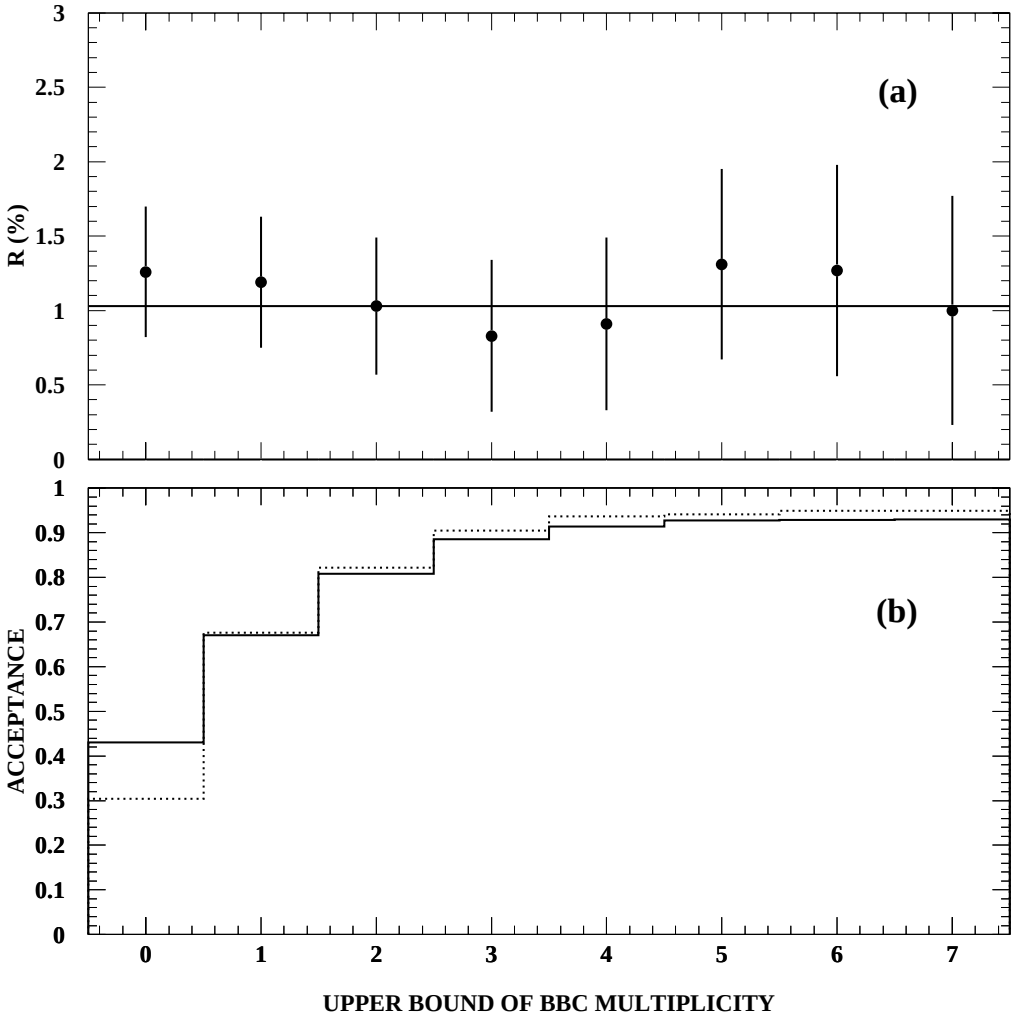

Figure 6.23: *(a) Diffractive to non-diffractive W production ratio, not corrected for BBC occupancy or one-vertex cut efficiency, as a function of upper bound BBC multiplicity, N_B. The solid line is drawn through the $N_B = 2$ point, which is used as the result; (b) Gap acceptance for angle-gap and charge-gap doubly correlated (solid) and anticorrelated (dashed) diffractive events with an electron/positron within $|\eta| < 1.1$.*

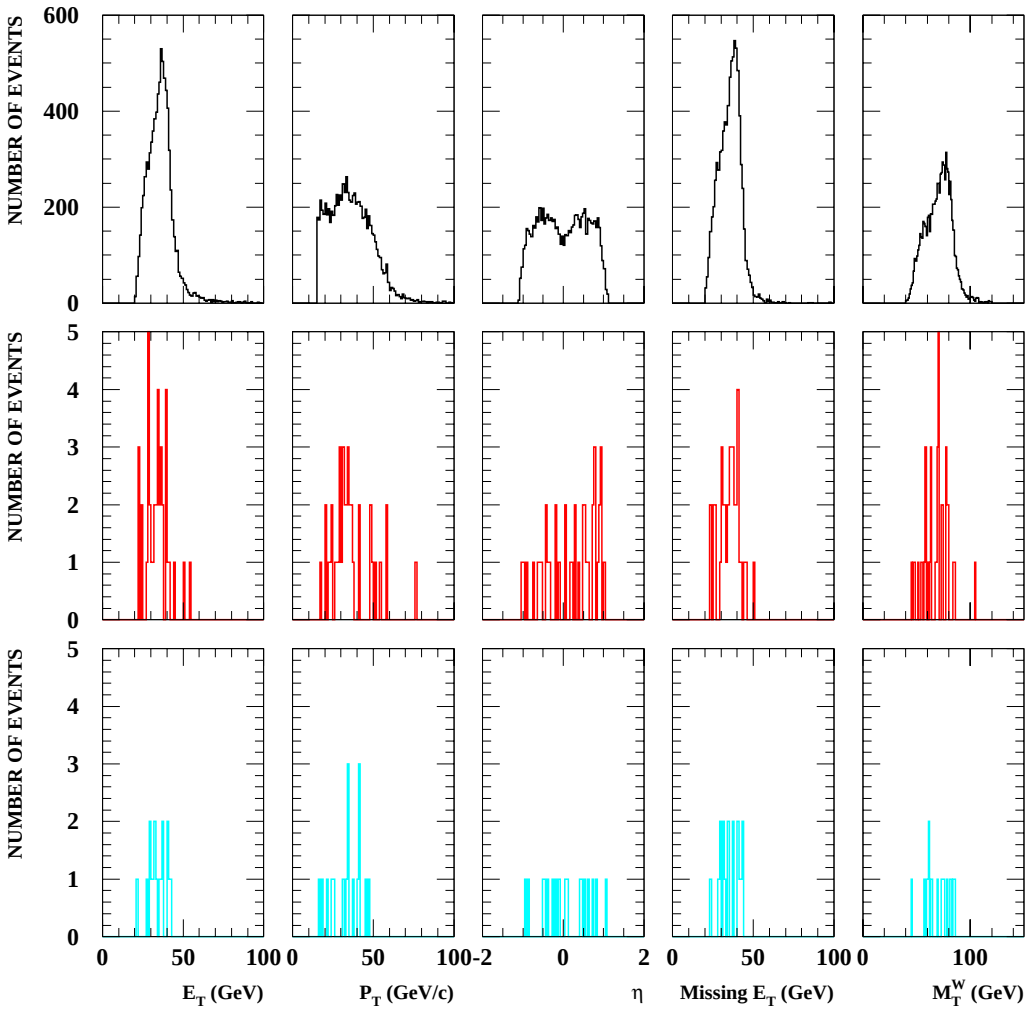

Figure 6.24: *Comparison of W event characteristic distributions: all W events (top row); W events from the signal region ($N_B = 2$ and $N_{\text{tower}} < 8$): (angle⊗charge)-correlated (middle row) and (angle⊗charge)-anticorrelated (bottom row) W events.*

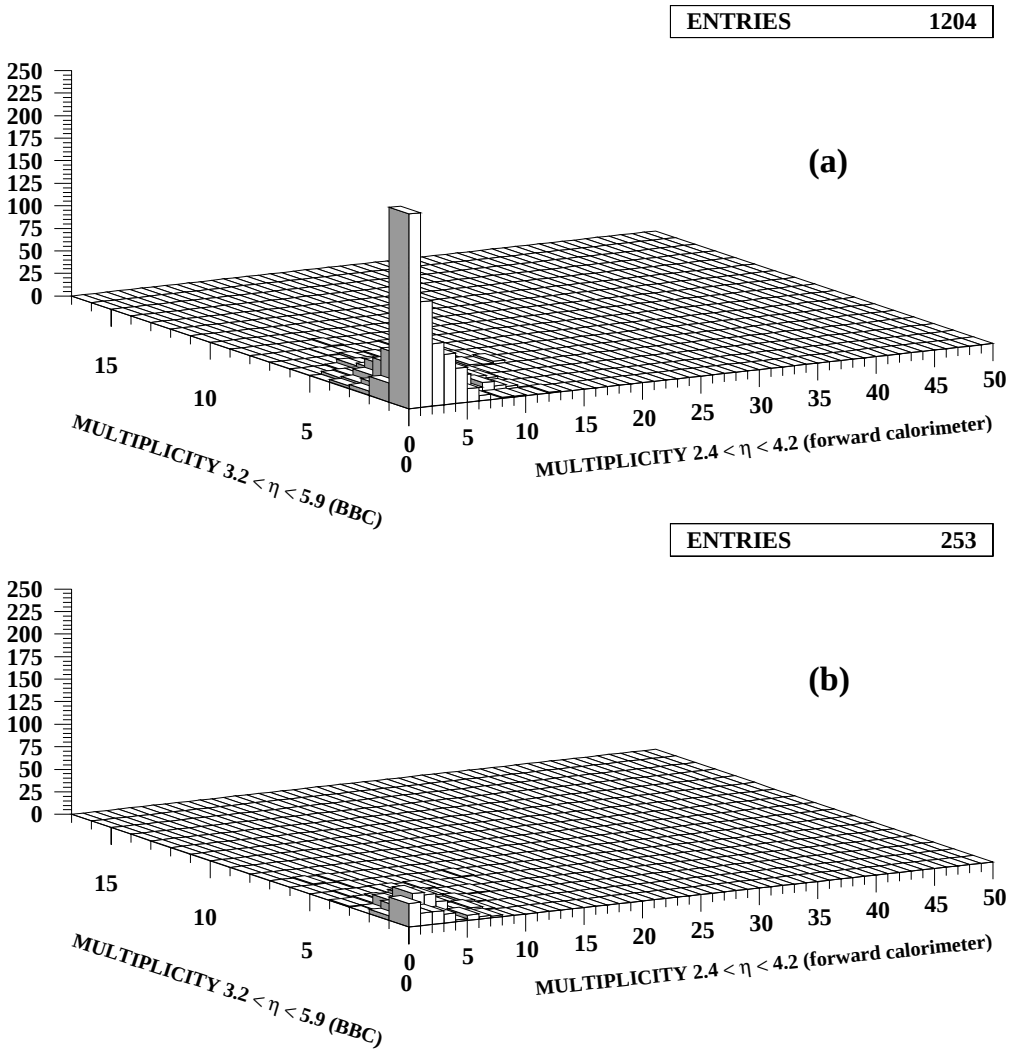

Figure 6.25: *Multiplicity of particles in the pseudorapidity region* $2.4 < \eta < 4.2$ *(forward calorimeter) and in the adjacent BBC region* $3.2 < \eta < 5.9$ *(a) for (angle⊗charge)-correlated and (b) for (angle⊗charge)-anticorrelated diffractive* W *events generated with* POMPYT *using a hard-quark structure for the pomeron.*

(a) and (angle⊗charge)-anticorrelated (b) events is observed in this case.

The gap acceptance for (angle⊗charge)-correlated, $a^{c}_{N_B,7;D}$, and (angle⊗charge)-anticorrelated, $a^{\overline{c}}_{N_B,7;D}$, diffractive W events with a central electron/positron is calculated from the above plots by summing the events within the first 8 bins of the tower multiplicity distributions, $N_{\rm tower} = 0-7$, and (N_B+1) bins of the BBC multiplicity distributions, and dividing the sum by the total number of correlated or anticorrelated events, respectively. Figure 6.23b shows the $a^{c}_{N_B,7;D}$ (solid) and $a^{\overline{c}}_{N_B,7;D}$ (dashed) for diffractive W events with a central electron/positron as a function of N_B. Multiplying $a^{c}_{N_B,7;D}$ ($a^{\overline{c}}_{N_B,7;D}$) by the fraction f^{c}_{D} ($f^{\overline{c}}_{D}$) of (angle⊗charge)-correlated ((angle⊗charge)-anticorrelated) diffractive W events with a central electron/positron and adding the results, we obtain the gap acceptance for the (angle⊗charge)-correlated and (angle⊗charge)-anticorrelated diffractive W events.

$$a^{gap}_{D} = a^{c}_{N_B,7;D}\cdot f^{c}_{D} + a^{\overline{c}}_{N_B,7;D}\cdot f^{\overline{c}}_{D} = \frac{N^{c}_{N_B,7;D} + N^{\overline{c}}_{N_B,7;D}}{N^{ce}_{D}}, \qquad (6.4)$$

where $N^{c}_{N_B,7;D}$ is the number of (angle⊗charge)-correlated and $N^{\overline{c}}_{N_B,7;D}$ is the number of (angle⊗charge)-anticorrelated diffractive W events in the signal region, and N^{ce}_{D} is the number of diffractive W events with a central electron/positron.

The fraction of events with a central electron/positron, f^{ce}_{D} (f^{ce}_{ND}), was found to be 0.26 ± 0.01 (0.25 ± 0.01) for diffractive (non-diffractive) W Monte Carlo events.

BBC Livetime Efficiency

The BBC livetime efficiency was measured by studying the sample of trigger-unbiased events with no reconstructed primary vertex, as described in section 6.1.2. A sample of such events from run 1A collected during the same runs as the events of the W sample was analysed by applying the same requirements to the BBC multiplicity as for the analysis of the W sample. The BBC livetime efficiency was calculated

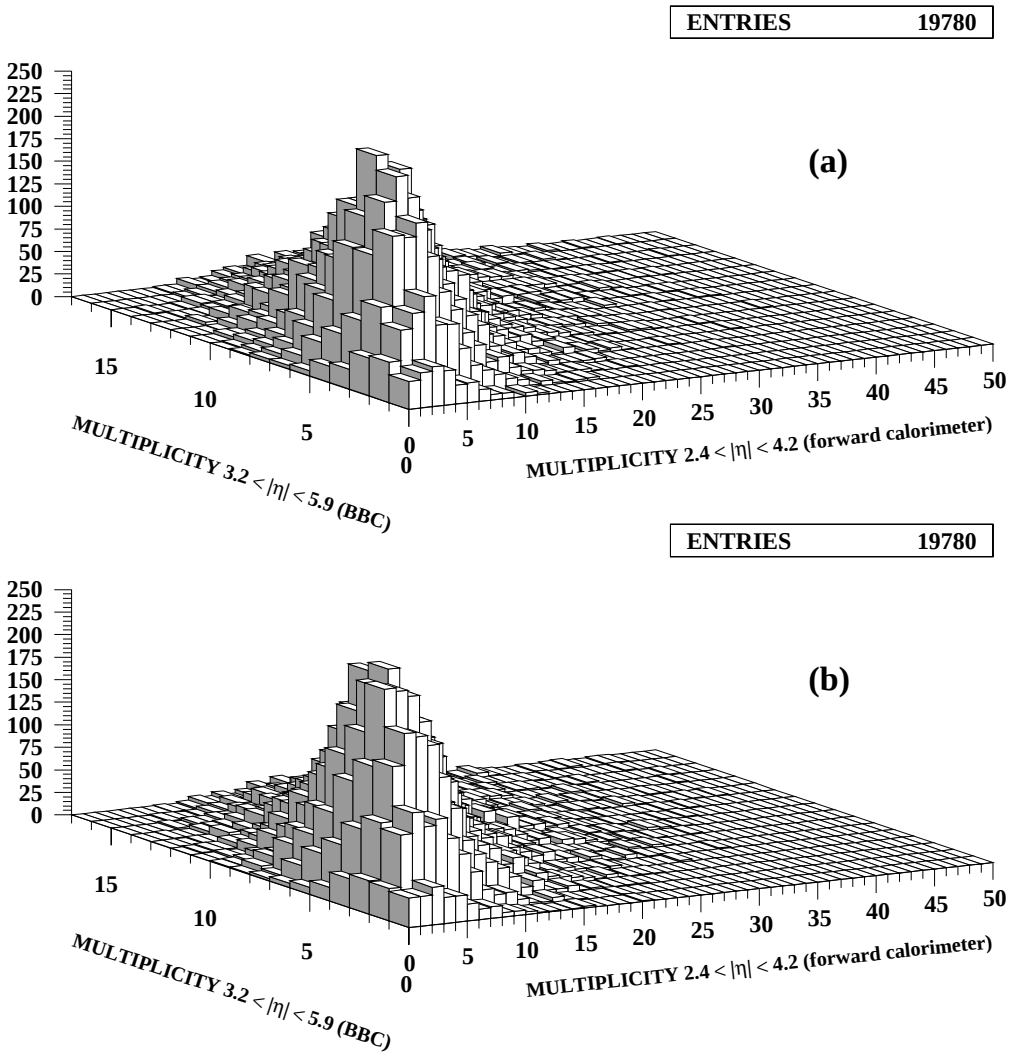

Figure 6.26: *Multiplicity of particles in the pseudorapidity region* $2.4 < |\eta| < 4.2$ *(forward calorimeter) and in the adjacent BBC region* $3.2 < |\eta| < 5.9$ *(a) for (angle⊗charge)-correlated and (b) for (angle⊗charge)-anticorrelated (b) non-diffractive* W *events generated with* PYTHIA.

as a fraction of $N_{BBC} \leq N_B$. The result is shown in Figure 6.27.

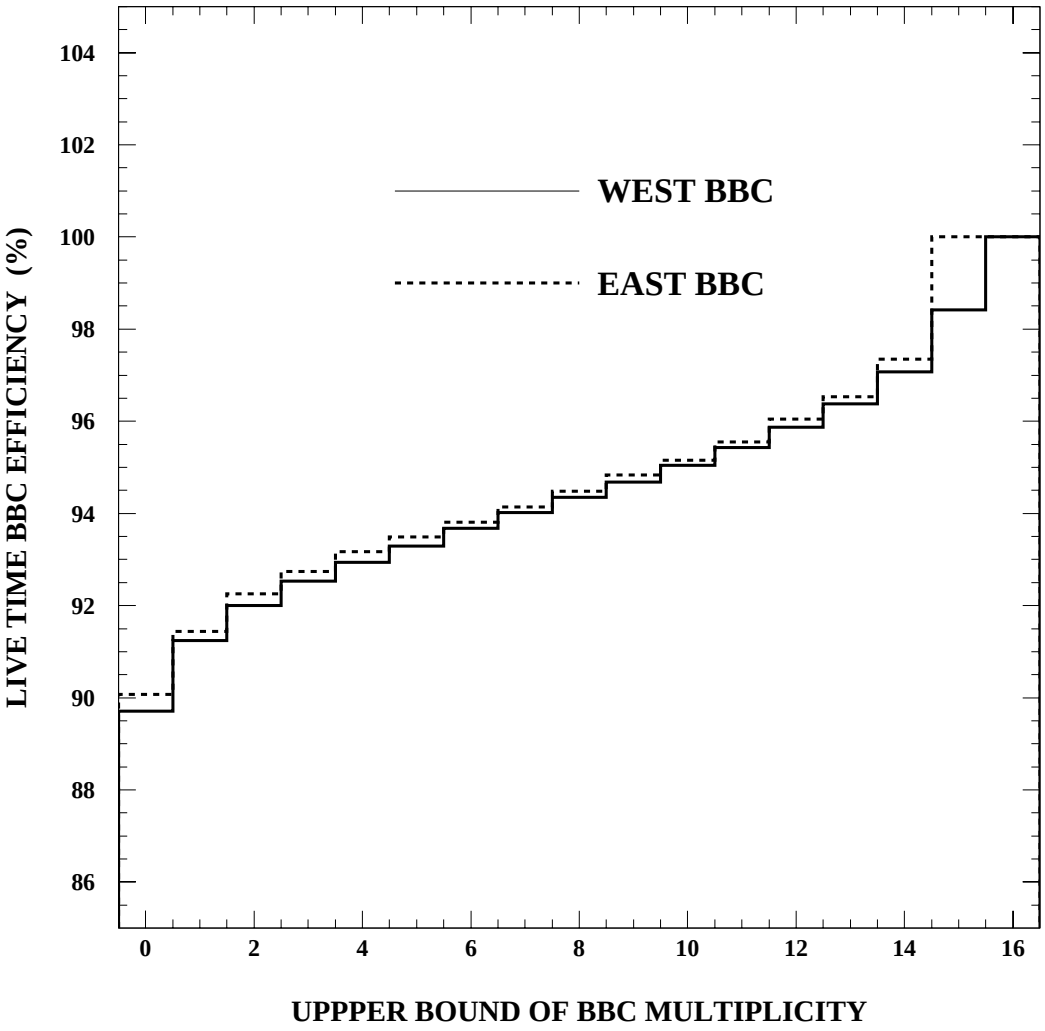

Figure 6.27: *The BBC livetime efficiency as a function of the upper bound of BBC multiplicity, N_B, for the run 1A data.*

The run 1B data were collected with the BBC trigger requirement activated, therefore it was not possible to create an appropriate trigger-unbiased no-vertex sample. The BBC livetime efficiency for run 1B was evaluated by scaling the BBC livetime efficiency for run 1A by the ratio of the average luminosities in runs 1B and

1A. The resulting probability of finding more than two hits in a BBC for data from both runs is $(15 \pm 2)\%$, corresponding to a BBC livetime acceptance of 0.85 ± 0.02 by which we divide R.

Single-Vertex Cut Correction

The one-vertex requirement, aimed to exclude events with multiple interactions in a beam crossing, may reject also some single-interaction W events. This happens due to confusion in the vertex reconstruction, which leads to extra reconstructed vertices, in particular in the events with high track multiplicity. Since, in general, non-diffractive events have higher particle activity than diffractive ones, the efficiency of the one-vertex cut for non-diffractive events is expected to be lower.

The one-vertex cut efficiency is defined as the number of events with one primary vertex divided by the number of single-interaction events. In order to evaluate the number of single-interaction events, first we calculate the mean number of minimum bias interactions per bunch crossing, which is given by

$$\bar{n} = \frac{L \cdot \sigma_{\mathrm{mb}}}{f} \tag{6.5}$$

where L is the instantaneous luminosity in units of 10^{30}, σ_{mb} is the minimum bias cross section in mb, and $f = 286.28$ is the frequency of the bunch crossings. Using this number, the probability of zero minimum bias interactions per bunch crossing is calculated using Poisson statistics. This probability, which is $e^{-\bar{n}}$, determines the fraction of W events without an overlapping minimum bias event, i.e. the number of single-interaction W events.

From a study of the rate of W events versus instantaneous luminosity we estimate that the one-vertex cut efficiency for non-diffractive W events, which constitute the bulk of the W sample, is ≈ 0.9. For diffractive W events, the single-vertex

cut efficiency is expected to be higher, somewhere within the range 0.9 – 1.0. Hence, we estimate that a correction of $0.95 \pm 0.05(syst)$, which is the relative efficiency of the one-vertex cut for diffractive and non-diffractive W events, must be applied to the value of R.

6.1.8 Result

The value of R obtained in section 6.1.6 is multiplied by $0.95 \pm 0.05(syst)$, the correction due to single-vertex requirement, and divided by 0.85, the BBC live-time efficiency, yielding

$$R_W = [1.15 \pm 0.51(stat)]\%$$

for the ratio of diffractive to non-diffractive W production.

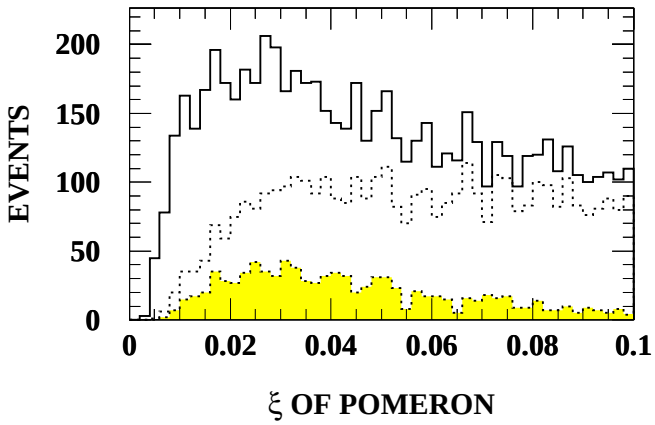

Figure 6.28: *Pomeron ξ-distribution for all Monte Carlo generated diffractive W events (solid line), for events with a central electron/positron (dotted line), and for events with a central electron/positron which are (angle⊗charge)-correlated with a BBC of multiplicity zero, one or two hits and $N_{\text{towers}} < 8$ (shaded histogram).*

The diffractive W signal is concentrated at small t, since we integrate over

t, and at ξ-values approximately in the range 0.01-0.05 (see Figure 6.28).

6.1.9 Systematic Uncertainties

As a ratio, R is insensitive to lepton selection cuts or inefficiencies and to the uncertainty in the luminosity.

As a systematic uncertainty in the gap-acceptance calculation we assign $\pm 13\%$, which is one half of the difference between the acceptances for $N_B = 1$ and $N_B = 3$ divided by the acceptance for $N_B = 2$.

In deriving the ratio R we assumed that the non-diffractive contributions to the correlated and anticorrelated distributions in Figure 6.18a are identical. This assumption is justified by the excellent matching of the two distributions for $N_B > 3$. A possible mismatch of the distributions within the available statistics introduces a systematic uncertainty, which was evaluated as follows. We made a straight line fit to the asymmetry of bins 4-10 of Figure 6.18b, and extrapolated the fit into bins 1-3. For each of the bins 1-3, we multiplied the extrapolated asymmetry and its error by twice the number of anticorrelated events, since the average number of non-diffractive correlated and anticorrelated events is expected to be the same, and added up the results for the three bins. Treating the sum as a signal yields a diffractive to non-diffractive ratio of $(0.01 \pm 0.11)\%$, which is consistent with zero. We treat the error of $\pm 0.11\%$ as a systematic uncertainty in our measured value of R and add it in quadrature to the gap-acceptance uncertainty to obtain a combined systematic uncertainty of $\pm 0.18\%$.

Including systematic uncertainties, the ratio of diffractive to non-diffractive W-boson production is

$$R_W = [1.15 \pm 0.51(stat) \pm 0.20(syst)]\%.$$

6.2 Jets in Diffractive W Events

The mechanism of diffractive W-boson production from gluons in the pomeron, illustrated in Figure 3.2, provides a tool for distinguishing between quarks and gluons in the pomeron. As was mentioned in Chapter 3, for a hard-gluon dominated pomeron with a structure of the form (3.1), diffractive Ws are produced always in association with a jet. Therefore, independent of the production rate, one can probe the pomeron structure by comparing the number of $W + Jet$ events in the sample of diffractive W candidate events with expectations from diffractive production assuming a hard-quark or a hard-gluon structure for the pomeron. Here we use (angle⊗charge)-correlated and (angle⊗charge)-anticorrelated events in the signal region and study the fraction of events with jets above a certain E_T^j threshold. The signal region is defined by zero multiplicity in the BBC and less than 8 towers above the energy threshold in the adjacent to a BBC forward calorimeter (see Figure 6.17). The analysis proceeds in the following steps: (i) the number of diffractive and non-diffractive W events in the signal region is evaluated; (ii) the correspondence between the jet E_T cut in data and MC is established; (iii) the fractions of W events with a jet above a given jet E_T threshold in the signal region are obtained from non-diffractive W MC and from diffractive W MC assuming a hard-quark or a hard-gluon structure for the pomeron; (iv) the number of observed $W + Jet$ events in the signal region in data is compared with the expected number obtained from the non-diffractive W MC and from the diffractive W MC assuming a hard-quark or a hard-gluon pomeron structure.

6.2.1 Signal versus Background

First, we evaluate the level of the non-diffractive background in the signal region. For the (angle⊗charge)-correlated and (angle⊗charge)-anticorrelated events one can write

$$\frac{N_D^c + N_{ND}^c}{N_D^{\bar{c}} + N_{ND}^{\bar{c}}} = \frac{N_{\rm data}^c}{N_{\rm data}^{\bar{c}}}, \tag{6.6}$$

where

N_D^c is the number of (angle⊗charge)-correlated diffractive W events,

N_{ND}^c is the number of (angle⊗charge)-correlated non-diffractive W events,

$N_D^{\bar{c}}$ is the number of (angle⊗charge)-anticorrelated diffractive W events,

$N_{ND}^{\bar{c}}$ is the number of (angle⊗charge)-anticorrelated non-diffractive W events,

$N_{\rm data}^c$ is the number of (angle⊗charge)-correlated data W events, and

$N_{\rm data}^{\bar{c}}$ is the number of (angle⊗charge)-anticorrelated data W events.

Transforming (6.6) and dividing by N_D^c, we obtain

$$N_{\rm data}^{\bar{c}} \left(1 + \frac{N_{ND}}{N_D^c}\right) = N_{\rm data}^c \left(\frac{N_D^{\bar{c}}}{N_D^c} + \frac{N_{ND}}{N_D^c}\right)$$

and

$$\frac{N_{ND}}{N_D^c} = \frac{N_{\rm data}^{\bar{c}} - N_{\rm data}^c \left(N_D^{\bar{c}}/N_D^c\right)}{N_{\rm data}^c - N_{\rm data}^{\bar{c}}},$$

where we have used $N_{ND}^c = N_{ND}^{\bar{c}} = N_{ND}$, which is justified from the study of non-diffractive W MC events (see Figure 6.26).

There are $N_{\rm data}^c = 34$ (angle⊗charge)-correlated and $N_{\rm data}^{\bar{c}} = 16$ (angle⊗charge)-anticorrelated W events confined within the first BBC-multiplicity bin and the first 8 bins of the forward calorimeter multiplicity. Thus,

$$\frac{N_{ND}}{N_D^c} = \frac{16 - 34\ \left(N_D^{\bar{c}}/N_D^c\right)}{18}$$

The value of $N_D^{\bar{c}}/N_D^c$ can be determined from the diffractive W Monte Carlo. Two samples of diffractive W events were generated using the POMPYT Monte Carlo, one

assuming a full hard-quark and the other a hard-gluon structure for the pomeron of the type (3.1), and the value of $N_D^{\bar{c}}/N_D^c$ was evaluated for these samples.

Hard-quark pomeron: For 518 (angle⊗charge)-correlated and 77 (angle⊗charge)-anticorrelated events in the signal region generated by POMPYT with full hard-quark structure function for the pomeron we obtain

$$\left[\frac{N_D^{\bar{c}}}{N_D^c}\right]_{\rm hq} = 0.149 \pm 0.015.$$

Therefore

$$\frac{N_{ND}}{N_D^c} = 0.61 \pm 0.03.$$

Using this value, the expected numbers of (angle⊗charge)-correlated, (angle⊗charge)-anticorrelated diffractive and non-diffractive W events are

$$\left.\begin{array}{rcrcl} N_D^c & + & N_{ND}^c & = & 34 \\ N_D^{\bar{c}} & + & N_{ND}^{\bar{c}} & = & 16 \\ N_{ND}^c & = & N_{ND}^{\bar{c}} & = & N_{ND} \end{array}\right\} \Longrightarrow \left\{\begin{array}{rcl} N_D^c & = & 21 \pm 2.8 \\ N_D^{\bar{c}} & = & 3 \pm 1.6 \\ N_{ND} & = & 13 \pm 2.8 \end{array}\right.$$

Hard-gluon pomeron: From the distributions obtained using the diffractive Monte Carlo with a full hard-gluonic pomeron structure, for 659 (angle⊗charge)-correlated and 89 (angle⊗charge)-anticorrelated diffractive W events, we calculate

$$\left[\frac{N_D^{\bar{c}}}{N_D^c}\right]_{\rm hg} = 0.135 \pm 0.013$$

$$\frac{N_{ND}}{N_D^c} = 0.63 \pm 0.03$$

$$\begin{array}{rcl} N_D^c & = & 21 \pm 2.8 \\ N_D^{\bar{c}} & = & 3 \pm 1.5 \\ N_{ND} & = & 13 \pm 2.8 \end{array}$$

The results from the two diffractive Monte Carlo simulations show that the hard-quark and hard-gluon pomeron structures of the form (3.1) lead to the same number

of expected diffractive and non-diffractive W events in the data sample and to the same (angle⊗charge) correlation asymmetry for diffractive W events.

6.2.2 Jets in the Control Region

In order to examine the relationship between the jet E_T cut in the data and Monte Carlo, we compared data with non-diffractive Monte Carlo W events in a control region defined by BBC multiplicity greater than 7, which ensures the absence of diffractive events, and calorimeter tower multiplicity less than 8.

Figure 6.29 shows the jet E_T distributions for (angle⊗charge)-correlated and (angle⊗charge)-anticorrelated data W events in the control region. The jet clustering was performed using a cone of radius 0.7.

Table 6.5 contains the number and fraction of events with jets above various jet E_T cuts for (angle⊗charge)-correlated and (angle⊗charge)-anticorrelated data W events in the control region. The corresponding distributions of the jet E_T

E_T^j CUT	NUMBER OF EVENTS		FRACTION	
(GeV)	correlated	anticorrelated	correlated	anticorrelated
NONE	867	836	1.0	1.0
1	564	571	0.65 ± 0.02	0.68 ± 0.02
2	507	518	0.58 ± 0.02	0.62 ± 0.02
3	424	431	0.49 ± 0.02	0.52 ± 0.02
4	349	368	0.40 ± 0.02	0.44 ± 0.02
5	**297**	**308**	$\mathbf{0.34 \pm 0.02}$	$\mathbf{0.37 \pm 0.02}$
6	246	249	0.28 ± 0.02	0.30 ± 0.02
7	207	211	0.24 ± 0.01	0.25 ± 0.02
8	169	180	0.19 ± 0.01	0.22 ± 0.01

Table 6.5: *The number and fraction of events with jets above various jet E_T cuts for data W events in the control region.*

for (angle⊗charge)-correlated and (angle⊗charge)-anticorrelated non-diffractive W Monte Carlo events in the control region are shown in Figure 6.30. Although the

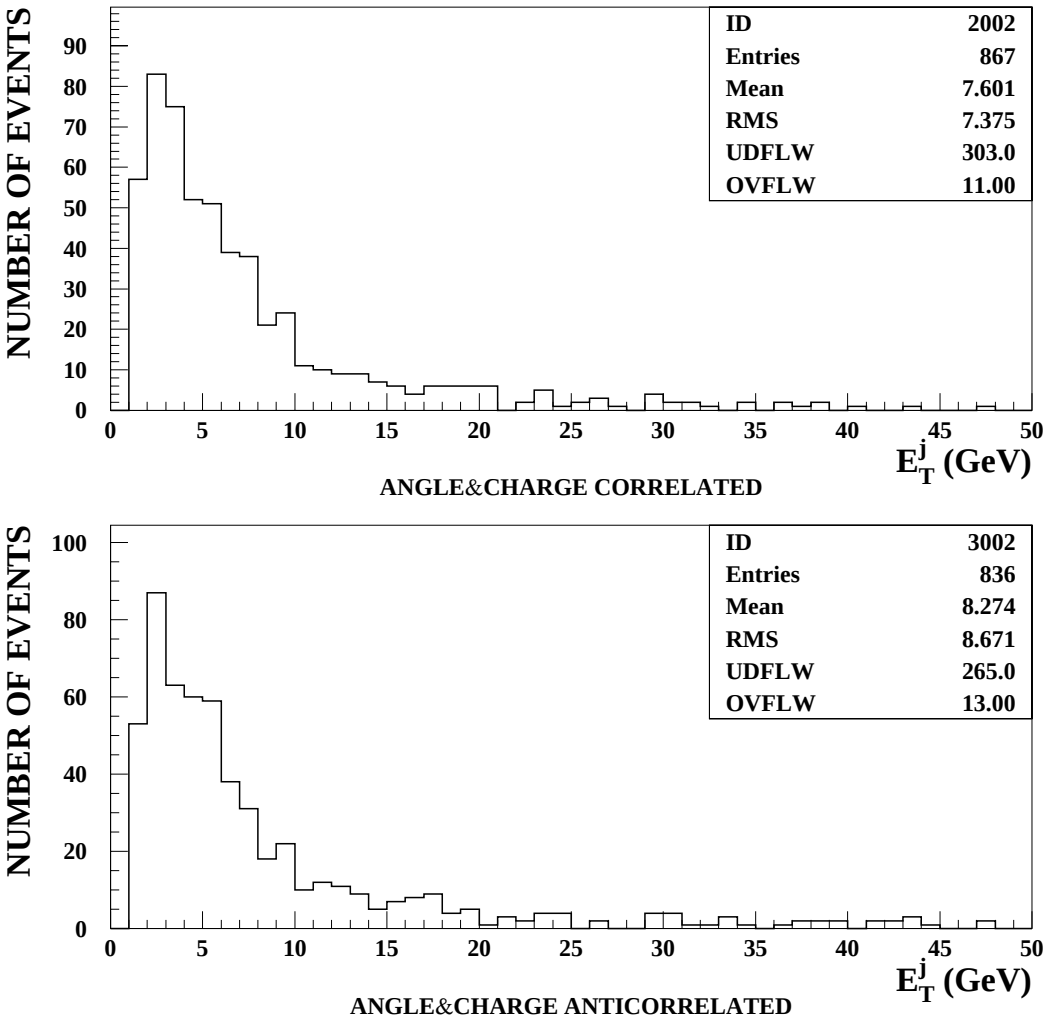

Figure 6.29: *Jet E_T distributions for (angle⊗charge)-correlated (top) and (angle⊗charge)-anticorrelated (bottom) data W events in the control sample.*

QFL detector simulation has been applied to MC events, the MC jet E_T spectra are slightly harder than the data distributions, because no jet energy correction was applied to the the data sample. The number and fraction of events with jets above

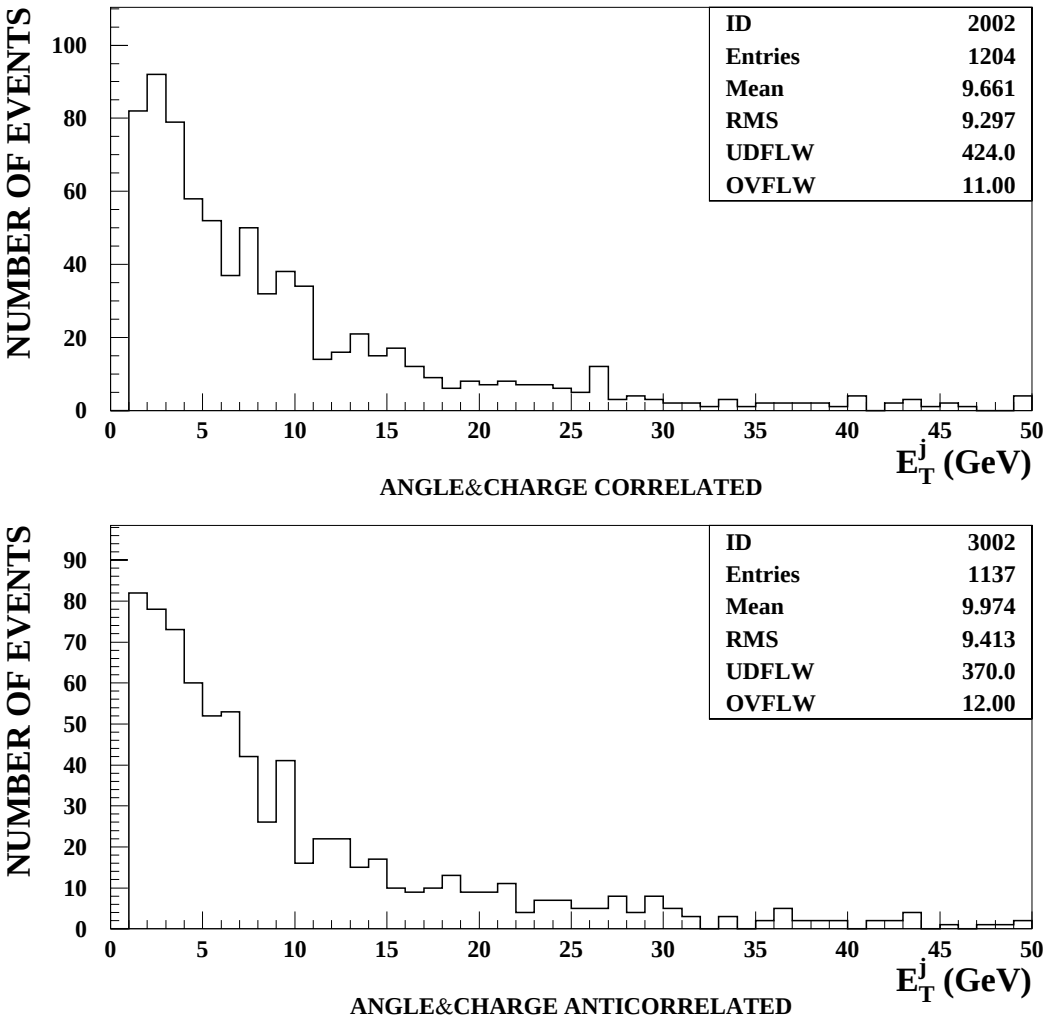

Figure 6.30: *Jet E_T distributions for (angle⊗charge)-correlated (top) and (angle⊗charge)-anticorrelated (bottom) non-diffractive W Monte Carlo events in the control sample.*

different jet E_T cuts for (angle⊗charge)-correlated and (angle⊗charge)-anticorrelated non-diffractive W Monte Carlo events in the control sample are shown in Table 6.6.

From a comparison of fractions of events with jets in tables 6.5 and 6.6, we find that

E_T^j CUT	NUMBER OF EVENTS		FRACTION	
(GeV)	correlated	anticorrelated	correlated	anticorrelated
NONE	1204	1137	1.0	1.0
1	780	767	0.65 ± 0.01	0.67 ± 0.01
2	698	685	0.58 ± 0.01	0.65 ± 0.01
3	606	607	0.50 ± 0.01	0.53 ± 0.01
4	527	534	0.45 ± 0.01	0.47 ± 0.01
5	469	474	0.39 ± 0.01	0.42 ± 0.01
6	**417**	**422**	$\mathbf{0.35 \pm 0.01}$	$\mathbf{0.37 \pm 0.01}$
7	380	369	0.32 ± 0.01	0.32 ± 0.01
8	330	327	0.27 ± 0.01	0.29 ± 0.01
9	298	301	0.25 ± 0.01	0.26 ± 0.01
10	260	260	0.22 ± 0.01	0.23 ± 0.01
11	226	244	0.19 ± 0.01	0.21 ± 0.01
12	212	222	0.18 ± 0.01	0.20 ± 0.01
13	196	200	0.16 ± 0.01	0.18 ± 0.01
14	175	185	0.15 ± 0.01	0.16 ± 0.01

Table 6.6: *The number and fraction of events with jets above different jet E_T cuts for non-diffractive W Monte Carlo events in the control region.*

the 5 GeV jet E_T cut in the data sample corresponds to a 6 GeV cut in the Monte Carlo. A 7 GeV jet E_T cut in the data gives the same fraction of events with jets as a 9 GeV cut in the Monte Carlo, and the fraction of events with jets above 10 GeV can be reproduced by a 14 GeV cut in the Monte Carlo.

6.2.3 Jets in the Signal Region

After establishing the correspondence between the jet E_T cuts in MC and data, we compare fractions of W events with jets above a certain E_T^j cut in the signal region for the data sample and for MC generated events. Figure 6.31 shows the jet E_T distributions for data (angle⊗charge)-correlated and (angle⊗charge)-anticorrelated W events in the signal region. The number and fraction of events with jets for

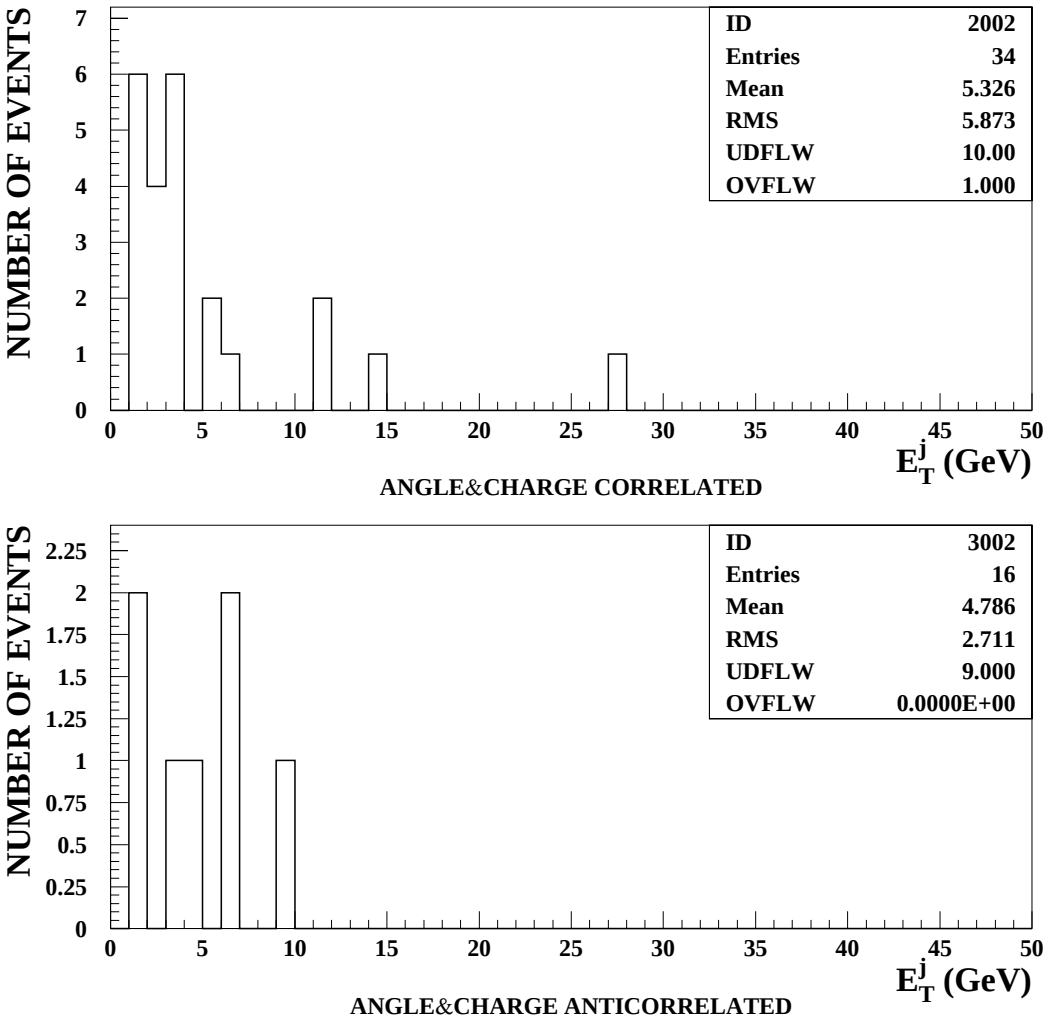

Figure 6.31: *Jet E_T distributions for (angle⊗charge)-correlated (top) and (angle⊗charge)-anticorrelated (bottom) data W events in the signal region.*

various jet E_T cuts for (angle⊗charge)-correlated and (angle⊗charge)-anticorrelated data W events in the signal region is presented in Table 6.7. Figure 6.32 shows the

E_T^j CUT	NUMBER OF EVENTS		FRACTION	
(GeV)	correlated	anticorrelated	correlated	anticorrelated
NONE	34	16	1.0	1.0
1	24	7	0.71 ± 0.08	0.44 ± 0.12
2	18	5	0.53 ± 0.09	0.31 ± 0.12
3	14	5	0.41 ± 0.08	0.31 ± 0.12
4	8	4	0.24 ± 0.07	0.25 ± 0.11
5	**8**	**3**	$\mathbf{0.24 \pm 0.07}$	$\mathbf{0.19 \pm 0.10}$
6	6	3	0.18 ± 0.07	0.19 ± 0.10
7	5	1	0.15 ± 0.06	0.06 ± 0.06
8	5	1	0.15 ± 0.06	0.06 ± 0.06

Table 6.7: *The number and fraction of events with jets above different jet E_T cuts for data W events in the signal region.*

jet E_T distributions for (angle⊗charge)-correlated and (angle⊗charge)-anticorrelated non-diffractive W Monte Carlo events in the signal region. The number and fraction of events with jets for various jet E_T cuts for (angle⊗charge)-correlated and (angle⊗charge)-anticorrelated non-diffractive W Monte Carlo events in the signal region are presented in Table 6.8. As is seen, the jet E_T spectra for the data and non-diffractive W MC events in the signal region differ rather significantly. However, the jet E_T distributions and the fractions of W events with jets above a certain E_T cut for the non-diffractive W MC events remains practically unchanged when moving from the control region to the signal region.

6.2.4 Jets in Diffractive W Monte Carlo Events

Hard-quark pomeron: Table 6.9 shows the number and fraction of events with jets for various jet E_T cuts for (angle⊗charge)-correlated and (angle⊗charge)-anticorrelated diffractive W Monte Carlo events in the signal region, generated using a full hard-

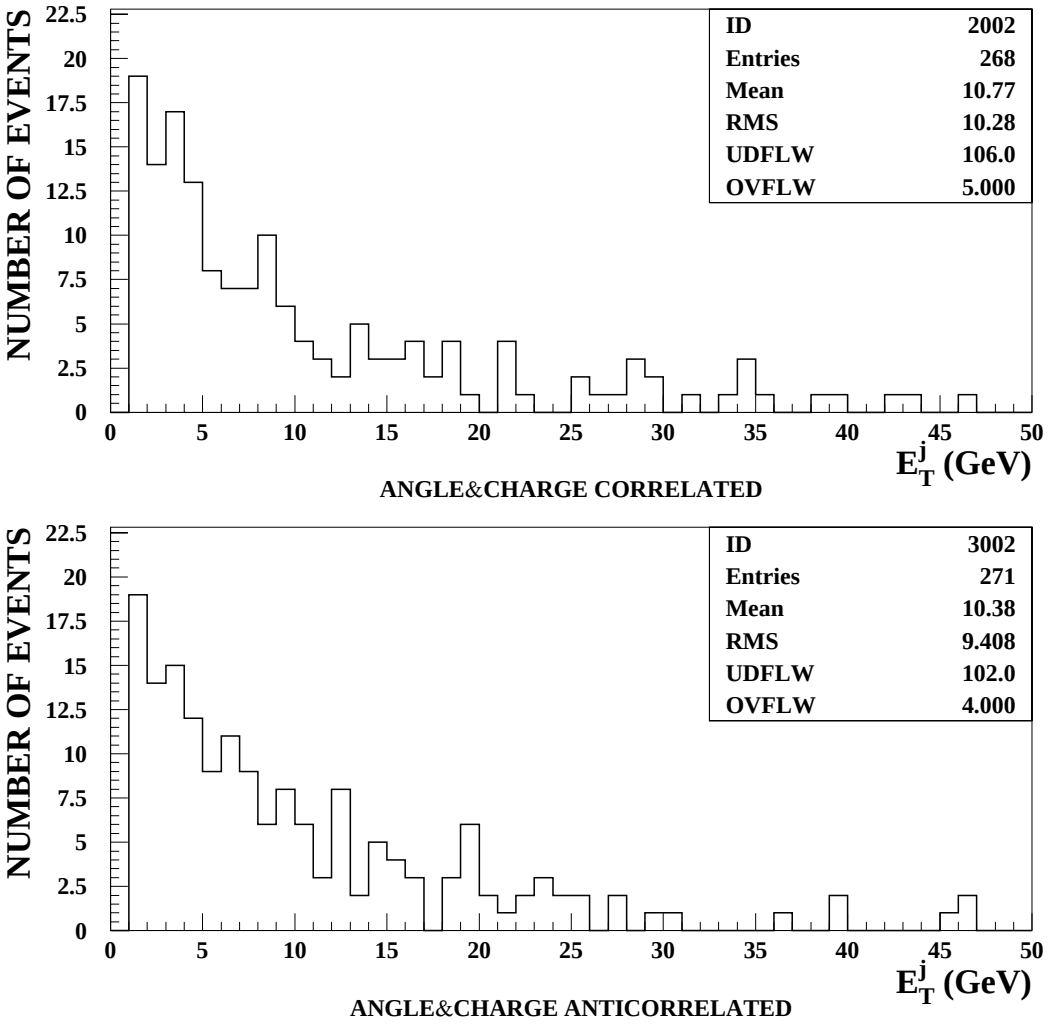

Figure 6.32: *Jet E_T distributions for (angle⊗charge)-correlated (top) and (angle⊗charge)-anticorrelated (bottom) non-diffractive W Monte Carlo events in the signal region.*

E_T^j CUT	NUMBER OF EVENTS		FRACTION	
(GeV)	correlated	anticorrelated	correlated	anticorrelated
NONE	268	271	1.0	1.0
1	162	169	0.60 ± 0.03	0.62 ± 0.03
2	143	150	0.53 ± 0.03	0.55 ± 0.03
3	129	136	0.48 ± 0.03	0.50 ± 0.03
4	112	121	0.42 ± 0.03	0.45 ± 0.03
5	99	109	0.37 ± 0.03	0.40 ± 0.03
6	**91**	**100**	$\mathbf{0.34 \pm 0.03}$	$\mathbf{0.37 \pm 0.03}$
7	84	89	0.31 ± 0.03	0.33 ± 0.03
8	77	80	0.29 ± 0.03	0.30 ± 0.03
9	67	74	0.25 ± 0.03	0.27 ± 0.03
10	61	66	0.23 ± 0.03	0.24 ± 0.03
11	57	60	0.21 ± 0.02	0.22 ± 0.03
12	54	57	0.20 ± 0.02	0.21 ± 0.02
13	52	49	0.19 ± 0.02	0.18 ± 0.02
14	47	47	0.18 ± 0.02	0.17 ± 0.02

Table 6.8: *The number and fraction of events with jets above different jet E_T cuts for non-diffractive W Monte Carlo events in the signal region.*

quark structure for the pomeron.

Hard-gluon pomeron: Table 6.10 shows the number and fraction of events with jets for various jet E_T cuts for (angle⊗charge)-correlated and (angle⊗charge)-anticorrelated diffractive W Monte Carlo events in the signal region, generated using a pure hard-gluonic structure for the pomeron.

6.2.5 Result

Multiplying the fractions of W events with jets obtained from the diffractive and non-diffractive Monte Carlo simulations by the corresponding numbers of events calculated in section 6.2.1, we obtain the expected numbers of W events with jets for a hard-quark and a hard-gluon pomeron structure. Table 6.11 shows the expected

E_T^j CUT	NUMBER OF EVENTS		FRACTION	
(GeV)	correlated	anticorrelated	correlated	anticorrelated
NONE	518	77	1.0	1.0
1	237	48	0.46 ± 0.02	0.62 ± 0.06
2	202	41	0.39 ± 0.02	0.53 ± 0.06
3	173	34	0.33 ± 0.02	0.44 ± 0.06
4	150	34	0.29 ± 0.02	0.44 ± 0.06
5	128	28	0.25 ± 0.02	0.36 ± 0.05
6	**103**	**26**	$\mathbf{0.20 \pm 0.02}$	$\mathbf{0.34 \pm 0.05}$
7	93	26	0.18 ± 0.02	0.34 ± 0.05
8	78	21	0.15 ± 0.02	0.27 ± 0.05
9	66	19	0.13 ± 0.01	0.25 ± 0.05
10	55	18	0.11 ± 0.01	0.23 ± 0.05
11	50	16	0.10 ± 0.01	0.21 ± 0.05
12	44	13	0.08 ± 0.01	0.17 ± 0.04
13	40	11	0.08 ± 0.01	0.14 ± 0.04
14	34	11	0.07 ± 0.01	0.14 ± 0.04

Table 6.9: *The number and the fraction of events with jets above various jet E_T cuts for diffractive W Monte Carlo events in the signal region, generated using a full hard-quark structure for the pomeron.*

E_T^j CUT	NUMBER OF EVENTS		FRACTION	
(GeV)	correlated	anticorrelated	correlated	anticorrelated
NONE	659	89	1.0	1.0
1	603	79	0.92 ± 0.01	0.89 ± 0.03
2	592	78	0.90 ± 0.01	0.88 ± 0.03
3	564	76	0.86 ± 0.01	0.85 ± 0.04
4	518	72	0.79 ± 0.02	0.81 ± 0.04
5	483	64	0.73 ± 0.02	0.72 ± 0.05
6	**438**	**57**	$\mathbf{0.66 \pm 0.02}$	$\mathbf{0.64 \pm 0.05}$
7	406	53	0.62 ± 0.02	0.60 ± 0.05
8	372	48	0.56 ± 0.02	0.54 ± 0.05
9	339	45	0.51 ± 0.02	0.51 ± 0.05
10	314	41	0.48 ± 0.02	0.46 ± 0.05
11	291	37	0.44 ± 0.02	0.42 ± 0.05
12	263	34	0.40 ± 0.02	0.38 ± 0.05
13	239	33	0.36 ± 0.02	0.37 ± 0.05
14	217	32	0.33 ± 0.02	0.36 ± 0.05

Table 6.10: *The number and the fraction of events with jets above various jet E_T cuts for diffractive W Monte Carlo events in the signal region, generated using a full hard-gluon structure for the pomeron.*

and observed numbers of W events with jets.

E_T^j CUT (GeV)	HARD-QUARK POMERON		HARD-GLUON POMERON		OBSERVED	
	corr.	anticorr.	corr.	anticorr.	corr.	anticorr.
5	10.1 ± 2.6	6.3 ± 2.0	20.1 ± 2.7	7.4 ± 1.9	8.0 ± 2.8	4.0 ± 2.0
6	$\mathbf{8.8 \pm 2.5}$	$\mathbf{5.8 \pm 1.9}$	$\mathbf{18.4 \pm 2.8}$	$\mathbf{6.7 \pm 1.9}$	$\mathbf{8.0 \pm 2.8}$	$\mathbf{3.0 \pm 1.7}$
8	6.9 ± 2.3	4.7 ± 1.8	15.5 ± 2.8	5.5 ± 1.9	6.0 ± 2.4	3.0 ± 1.7
9	6.0 ± 2.2	4.3 ± 1.8	14.0 ± 2.8	5.0 ± 1.8	5.0 ± 2.2	1.0 ± 1.0
11	4.8 ± 2.0	3.5 ± 1.7	12.0 ± 2.7	4.1 ± 1.7	5.0 ± 2.2	1.0 ± 1.0

Table 6.11: *Expected and observed numbers of W events with jets.*

The numbers of expected (angle$\otimes$charge)-correlated diffractive W events with a jet above a 6 GeV E_T^j cut from hard-quark and hard-gluon pomeron MC, including systematics, are $8.8 \pm 2.5^{+1.3}_{-1.0}$ and $18.4 \pm 2.8^{+1.7}_{-1.3}$, respectively. The systematics due to uncertainty in the matching of the jet E_T cut in data and Monte Carlo was evaluated by varying the MC jet E_T cut by 1 GeV.

The observed number of 8 ± 2.8 events with a jet agrees with the hard-quark MC prediction and disagrees with the hard-gluon prediction.

Chapter 7

Discussion of the Results

7.1 Quark-Gluon Content of the Pomeron

Below we compare our results with POMPYT predictions and with results from other experiments. The predictions depend on the assumed pomeron structure function and on the form and normalization of the pomeron flux factor, $f_{I\!P/p}(\xi,t)$. We first use the "standard" flux factor, defined in (2.17). For a two (three) flavor hard-quark pomeron structure of the form $\sim \beta(1-\beta)$ we obtain R_W^{hq}=24% (16%), while for a hard-gluon structure of the same form, $R_W^{hg} = 1.1\%$. Our measured ratio, $R_W = (1.15 \pm 0.55)\%$, favors a purely gluonic pomeron, which however is incompatible with the low fraction of diffractive $W + Jet$ events we observe. The HERA experiments probing the pomeron structure through diffractive DIS [10, 12] at $8.5 < Q^2 < 65$ GeV^2 report a quark component of the pomeron structure function which is flat in β, rises slowly with Q^2 at any given fixed β, and accounts for a fraction of about one third of the momentum of the pomeron, assuming the standard pomeron flux. Independent of the pomeron flux normalization, by combining diffractive dijet photoproduction and diffractive DIS results, the ZEUS collaboration

reports [13] an integrated hard-quark momentum fraction of $0.2 < f_q < 0.7$, while the H1 collaboration [11], from a QCD analysis of diffractive DIS, obtains $f_q \approx 0.2$ at $Q^2 \sim 60$ GeV^2. Using a pomeron with a hard-quark fraction of 0.2 and a hard-gluon fraction of 0.8, POMPYT predicts ratios R_W of 5.7% (4.1%) for two (three) quark flavors, which are larger than our measured value of $(1.15 \pm 0.55)\%$ by more than eight (five) standard deviations.

The hard-quark and(or) hard-gluon component of the pomeron structure can be determined independently of the pomeron flux normalization from a comparison of the present measurement of diffractive W-boson production with the diffractive dijet production rate of $R_{JJ} = (0.75 \pm 0.05(stat) \pm 0.09(syst)\%$ recently measured at CDF [52]. Assuming that only hard partons carrying a fraction of the total pomeron momentum participate in diffractive W and dijet production, the momentum fraction of hard partons in the pomeron can be evaluated as a function of the gluon fraction, f_g, of the hard component of the pomeron by comparing the measured rates with the MC predictions. Figure 7.1 presents curves of the momentum fraction of hard partons in the pomeron versus f_g corresponding to the $\pm 1\ \sigma$ values obtained from the measured rates and the corresponding MC predictions with the standard pomeron flux. The $\pm 1\ \sigma$ limits from the W measurement are shown as dotted (solid) lines for two (three) light quark flavors in the pomeron. The dashed lines show the UA8 result [46] and the dashed-dotted lines the ZEUS result [13]. The CDF more precise measurement of diffractive dijet production is in agreement with the UA8 result. From the hatched diamond-shaped region in Figure 7.1, confined by the CDF dijet and W measurements, we evaluate the gluon fraction of the hard pomeron component to be $f_g = 0.7 \pm 0.2$. This gluon fraction, which does not depend on the pomeron flux normalization or the validity of the momentum sum rule for the pomeron, agrees with the ZEUS result of $0.3 < f_g < 0.8$. However, the momentum fraction (0.18 ± 0.04)

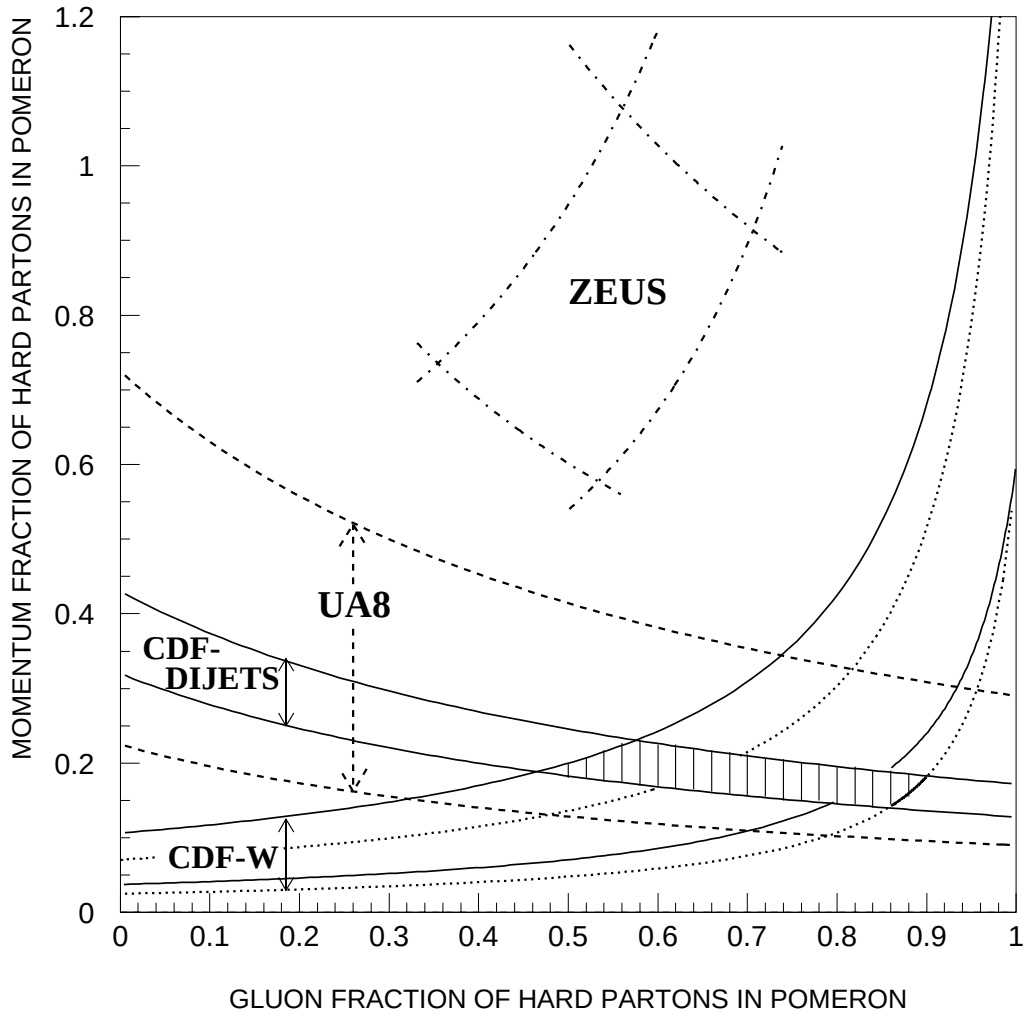

Figure 7.1: *Momentum fraction versus gluon fraction of hard partons in the pomeron evaluated by comparing measured diffractive rates with MC predictions based on the standard (see text) pomeron flux and assuming that only hard partons in the pomeron participate in the diffractive process considered. Results are shown for ZEUS (dashed-dotted), UA8 (dashed) and the CDF-DIJETS and CDF-W measurements. The CDF-W result is shown for two (dotted) or three (solid) light quark flavors in the pomeron. The shaded region is used in the text to extract the quark to gluon fraction of the pomeron and the standard flux discrepancy factor.*

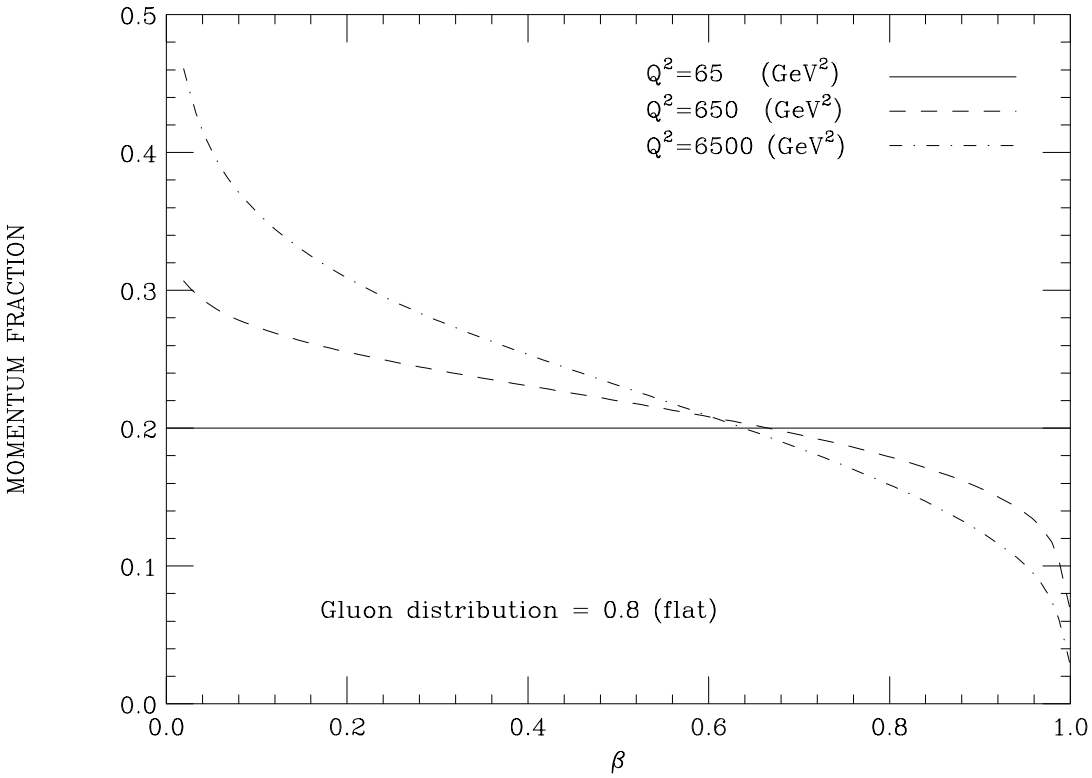

Figure 7.2: *Effect of DGLAP Q^2 evolution on the quark component of the pomeron structure. (solid line) input quark distribution, taken to be flat in β at Q^s=65 GeV^2; (dashed line) quark distribution at Q^2=650 GeV^2; (dashed-dotted line) quark distribution at Q^2=6500 GeV^2.*

we measure is well below the range $0.4 - 1.6$ reported by ZEUS. This discrepancy cannot be attributed to the Q^2 evolution of the pomeron structure function. We estimate that the effect on the quark and gluon fractions of the Q^2 evolution of the pomeron structure function from $Q^2 = 60$ GeV^2 to $Q^2 = M_W^2$ proposed by H1 is of $\mathcal{O}(10\%)$ (see Figure 7.2). Thus, the observed discrepancy implies a breakdown of factorization as used in [7] and in POMPYT, which could be due to a decrease of the pomeron flux at the Tevatron energy.

We now compare our results with POMPYT predictions using the "renormalized" pomeron flux proposed in Ref. [45], and defined as the standard flux nor-

malized, if its integral exceeds unity, to one pomeron per nucleon. The normalization factor is ≈ 9 at $\sqrt{s} = 1.8$ TeV (CDF) and ≈ 1 at HERA (see [45]). The predictions for R_W become 2.7% (1.8%) for a two (three) flavor pure hard-quark and 0.12% for a pure hard-gluon pomeron structure. Based on these predictions, our R_W value of $(1.15 \pm 0.55)\%$ implies hard-quark fractions of $f_q = 0.4 \pm 0.2$ (0.6 ± 0.3) for two (three) quark flavors. These fractions are consistent with the ZEUS and H1 results of $0.2 < f_q < 0.7$ and $f_q \approx 0.2$, respectively, and with the gluon fraction obtained from the comparison with diffractive dijet rate. Assuming the validity of the momentum sum rule for the pomeron, $f_q + f_g = 1$, the predicted fractional gluon contribution to R_W is $(0.12\%)(1-f_q)/[(0.12\%)(1-f_q)+Af_q]$, where A=2.7% (1.8%) for two (three) quark flavors. From our values of f_q, the gluon contribution to R_W is predicted to be 6.6% (4.2%) for two (three) quark flavors, which can explain the low fraction of $W + Jet$ events we observe.

7.2 Conclusions

The first observation of diffractively produced W-bosons in $\bar{p}p$ collisions at $\sqrt{s} = 1.8$ TeV is presented using data from the Collider Detector at Fermilab. In a sample of $W \rightarrow e\nu$ events an excess of events with a forward rapidity gap is found, which is attributed to diffraction. The probability that this excess is consistent with non-diffractive production is 1.1×10^{-4} (3.8σ).

The diffractive to non-diffractive W-boson production ratio is measured to be

$$R_W = (1.15 \pm 0.55)\%.$$

The relatively low fraction of observed diffractive $W + Jet$ events implies that mainly quarks from the pomeron, which mediates diffraction, participate in

diffractive W-boson production.

Assuming a hard gluon and quark pomeron structure of the form $\sim \beta(1-\beta)$, and comparing the present result on diffractive W-boson production with the diffractive dijet production rate and Monte Carlo predictions, the hard-gluon component of the pomeron is determined to be $f_g = 0.7 \pm 0.2$. This result, which is independent of the pomeron flux normalization or of the momentum sum rule for the pomeron, is consistent with results from the ZEUS and H1 experiments and also agrees with the hard-quark fraction of the pomeron structure, $f_q = 0.4 \pm 0.2$ (0.6 ± 0.3) for two (three) quark flavors, obtained in the present analysis from the comparison of the measured W-boson production rate with Monte Carlo predictions using the "renormalized" pomeron flux.

CDF COLLABORATION

F. Abe,[16] H. Akimoto,[35] A. Akopian,[30] M. G. Albrow,[7] S. R. Amendolia,[26] D. Amidei,[19] J. Antos,[32] S. Aota,[35] G. Apollinari,[30] T. Asakawa,[35] W. Ashmanskas,[17] M. Atac,[7] F. Azfar,[25] P. Azzi-Bacchetta,[24] N. Bacchetta,[24] W. Badgett,[19] S. Bagdasarov,[30] M. W. Bailey,[21] J. Bao,[38] P. de Barbaro,[29] A. Barbaro-Galtieri,[17] V. E. Barnes,[28] B. A. Barnett,[15] M. Barone,[26] E. Barzi,[9] G. Bauer,[18] T. Baumann,[11] F. Bedeschi,[26] S. Behrends,[3] S. Belforte,[26] G. Bellettini,[26] J. Bellinger,[37] D. Benjamin,[34] J. Benlloch,[18] J. Bensinger,[3] D. Benton,[25] A. Beretvas,[7] J. P. Berge,[7] J. Berryhill,[5] S. Bertolucci,[9] B. Bevensee,[25] A. Bhatti,[30] K. Biery,[7] M. Binkley,[7] D. Bisello,[24] R. E. Blair,[1] C. Blocker,[3] A. Bodek,[29] W. Bokhari,[18] V. Bolognesi,[2] G. Bolla,[24] D. Bortoletto,[28] J. Boudreau,[27] L. Breccia,[2] C. Bromberg,[20] N. Bruner,[21] E. Buckley-Geer,[7] H. S. Budd,[29] K. Burkett,[19] G. Busetto,[24] A. Byon-Wagner,[7] K. L. Byrum,[1] J. Cammerata,[15] C. Campagnari,[7] M. Campbell,[19] A. Caner,[26] W. Carithers,[17] D. Carlsmith,[37] A. Castro,[24] D. Cauz,[26] Y. Cen,[29] F. Cervelli,[26] P. S. Chang,[32] P. T. Chang,[32] H. Y. Chao,[32] J. Chapman,[19] M. -T. Cheng,[32] G. Chiarelli,[26] T. Chikamatsu,[35] C. N. Chiou,[32] L. Christofek,[13] S. Cihangir,[7] A. G. Clark,[10] M. Cobal,[26] E. Cocca,[26] M. Contreras,[5] J. Conway,[31] J. Cooper,[7] M. Cordelli,[9] C. Couyoumtzelis,[10] D. Crane,[1] D. Cronin-Hennessy,[6] R. Culbertson,[5] T. Daniels,[18] F. DeJongh,[7] S. Delchamps,[7] S. Dell'Agnello,[26] M. Dell'Orso,[26] R. Demina,[7] L. Demortier,[30] M. Deninno,[2] P. F. Derwent,[7] T. Devlin,[31] J. R. Dittmann,[6] S. Donati,[26] J. Done,[33] T. Dorigo,[24] A. Dunn,[19] N. Eddy,[19] K. Einsweiler,[17] J. E. Elias,[7] R. Ely,[17] E. Engels, Jr.,[27] D. Errede,[13] S. Errede,[13] Q. Fan,[29] G. Feild,[38] C. Ferretti,[26] I. Fiori,[2] B. Flaugher,[7] G. W. Foster,[7] M. Franklin,[11] M. Frautschi,[34] J. Freeman,[7] J. Friedman,[18] H. Frisch,[5] Y. Fukui,[16]

S. Funaki,[35] S. Galeotti,[26] M. Gallinaro,[24] O. Ganel,[34] M. Garcia-Sciveres,[17] A. F. Garfinkel,[28] C. Gay,[11] S. Geer,[7] D. W. Gerdes,[15] P. Giannetti,[26] N. Giokaris,[30] P. Giromini,[9] G. Giusti,[26] L. Gladney,[25] D. Glenzinski,[15] M. Gold,[21] J. Gonzalez,[25] A. Gordon,[11] A. T. Goshaw,[6] Y. Gotra,[24] K. Goulianos,[30] H. Grassmann,[26] L. Groer,[31] C. Grosso-Pilcher,[5] G. Guillian,[19] R. S. Guo,[32] C. Haber,[17] E. Hafen,[18] S. R. Hahn,[7] R. Hamilton,[11] R. Handler,[37] R. M. Hans,[38] F. Happacher,[26] K. Hara,[35] A. D. Hardman,[28] B. Harral,[25] R. M. Harris,[7] S. A. Hauger,[6] J. Hauser,[4] C. Hawk,[31] E. Hayashi,[35] J. Heinrich,[25] K. D. Hoffman,[28] M. Hohlmann,[5] C. Holck,[25] R. Hollebeek,[25] L. Holloway,[13] A. Hölscher,[14] S. Hong,[19] G. Houk,[25] P. Hu,[27] B. T. Huffman,[27] R. Hughes,[22] J. Huston,[20] J. Huth,[11] J. Hylen,[7] H. Ikeda,[35] M. Incagli,[26] J. Incandela,[7] G. Introzzi,[26] J. Iwai,[35] Y. Iwata,[12] H. Jensen,[7] U. Joshi,[7] R. W. Kadel,[17] E. Kajfasz,[24] H. Kambara,[10] T. Kamon,[33] T. Kaneko,[35] K. Karr,[36] H. Kasha,[38] Y. Kato,[23] T. A. Keaffaber,[28] L. Keeble,[9] K. Kelley,[18] R. D. Kennedy,[7] R. Kephart,[7] P. Kesten,[17] D. Kestenbaum,[11] R. M. Keup,[13] H. Keutelian,[7] F. Keyvan,[4] B. Kharadia,[13] B. J. Kim,[29] D. H. Kim,[7a] H. S. Kim,[14] S. B. Kim,[19] S. H. Kim,[35] Y. K. Kim,[17] L. Kirsch,[3] P. Koehn,[29] K. Kondo,[35] J. Konigsberg,[8] S. Kopp,[5] K. Kordas,[14] A. Korytov,[8] W. Koska,[7] E. Kovacs,[7a] W. Kowald,[6] M. Krasberg,[19] J. Kroll,[7] M. Kruse,[29] T. Kuwabara,[35] S. E. Kuhlmann,[1] E. Kuns,[31] A. T. Laasanen,[28] S. Lammel,[7] J. I. Lamoureux,[3] T. LeCompte,[1] S. Leone,[26] J. D. Lewis,[7] P. Limon,[7] M. Lindgren,[4] T. M. Liss,[13] N. Lockyer,[25] O. Long,[25] C. Loomis,[31] M. Loreti,[24] J. Lu,[33] D. Lucchesi,[26] P. Lukens,[7] S. Lusin,[37] J. Lys,[17] K. Maeshima,[7] A. Maghakian,[30] P. Maksimovic,[18] M. Mangano,[26] J. Mansour,[20] M. Mariotti,[24] J. P. Marriner,[7] A. Martin,[38] J. A. J. Matthews,[21] R. Mattingly,[18] P. McIntyre,[33] P. Melese,[30] A. Menzione,[26] E. Meschi,[26] S. Metzler,[25] C. Miao,[19] T. Miao,[7] G. Michail,[11] R. Miller,[20] H. Minato,[35] S. Miscetti,[9] M. Mishina,[16] H. Mitsushio,[35] T. Miyamoto,[35] S. Miyashita,[35] N. Moggi,[26]

Y. Morita,[16] J. Mueller,[27] A. Mukherjee,[7] T. Muller,[4] P. Murat,[26] H. Nakada,[35] I. Nakano,[35] C. Nelson,[7] D. Neuberger,[4] C. Newman-Holmes,[7] C.-Y. Ngan,[18] M. Ninomiya,[35] L. Nodulman,[1] S. H. Oh,[6] K. E. Ohl,[38] T. Ohmoto,[12] T. Ohsugi,[12] R. Oishi,[35] M. Okabe,[35] T. Okusawa,[23] R. Oliveira,[25] J. Olsen,[37] C. Pagliarone,[2] R. Paoletti,[26] V. Papadimitriou,[34] S. P. Pappas,[38] N. Parashar,[26] S. Park,[7] A. Parri,[9] J. Patrick,[7] G. Pauletta,[26] M. Paulini,[17] A. Perazzo,[26] L. Pescara,[24] M. D. Peters,[17] T. J. Phillips,[6] G. Piacentino,[2] M. Pillai,[29] K. T. Pitts,[7] R. Plunkett,[7] L. Pondrom,[37] J. Proudfoot,[1] F. Ptohos,[11] G. Punzi,[26] K. Ragan,[14] D. Reher,[17] A. Ribon,[24] F. Rimondi,[2] L. Ristori,[26] W. J. Robertson,[6] T. Rodrigo,[26] S. Rolli,[26] J. Romano,[5] L. Rosenson,[18] R. Roser,[13] W. K. Sakumoto,[29] D. Saltzberg,[5] A. Sansoni,[9] L. Santi,[26] H. Sato,[35] P. Schlabach,[7] E. E. Schmidt,[7] M. P. Schmidt,[38] A. Scribano,[26] S. Segler,[7] S. Seidel,[21] Y. Seiya,[35] G. Sganos,[14] M. D. Shapiro,[17] N. M. Shaw,[28] Q. Shen,[28] P. F. Shepard,[27] M. Shimojima,[35] M. Shochet,[5] J. Siegrist,[17] A. Sill,[34] P. Sinervo,[14] P. Singh,[27] J. Skarha,[15] K. Sliwa,[36] F. D. Snider,[15] T. Song,[19] J. Spalding,[7] T. Speer,[10] P. Sphicas,[18] F. Spinella,[26] M. Spiropulu,[11] L. Spiegel,[7] L. Stanco,[24] J. Steele,[37] A. Stefanini,[26] K. Strahl,[14] J. Strait,[7] R. Ströhmer,[7a] D. Stuart,[7] G. Sullivan,[5] A. Soumarokov,[32] K. Sumorok,[18] J. Suzuki,[35] T. Takada,[35] T. Takahashi,[23] T. Takano,[35] K. Takikawa,[35] N. Tamura,[12] B. Tannenbaum,[21] F. Tartarelli,[26] W. Taylor,[14] P. K. Teng,[32] Y. Teramoto,[23] S. Tether,[18] D. Theriot,[7] T. L. Thomas,[21] R. Thun,[19] M. Timko,[36] P. Tipton,[29] A. Titov,[30] S. Tkaczyk,[7] D. Toback,[5] K. Tollefson,[29] A. Tollestrup,[7] W. Trischuk,[14] J. F. de Troconiz,[11] S. Truitt,[19] J. Tseng,[18] N. Turini,[26] T. Uchida,[35] N. Uemura,[35] F. Ukegawa,[25] G. Unal,[25] J. Valls,[7a] S. C. van den Brink,[27] S. Vejcik, III,[19] G. Velev,[26] R. Vidal,[7] M. Vondracek,[13] D. Vucinic,[18] R. G. Wagner,[1] R. L. Wagner,[7] J. Wahl,[5] N. B. Wallace,[26] A. M. Walsh,[31] C. Wang,[6] C. H. Wang,[32] J. Wang,[5] M. J. Wang,[32] Q. F. Wang,[30] A. Warburton,[14] T. Watts,[31] R. Webb,[33] C. Wei,[6] C. Wendt,[37]

H. Wenzel,[17] W. C. Wester, III,[7] A. B. Wicklund,[1] E. Wicklund,[7] R. Wilkinson,[25] H. H. Williams,[25] P. Wilson,[5] B. L. Winer,[22] D. Winn,[19] D. Wolinski,[19] J. Wolinski,[20] S. Worm,[21] X. Wu,[10] J. Wyss,[24] A. Yagil,[7] W. Yao,[17] K. Yasuoka,[35] Y. Ye,[14] G. P. Yeh,[7] P. Yeh,[32] M. Yin,[6] J. Yoh,[7] C. Yosef,[20] T. Yoshida,[23] D. Yovanovitch,[7] I. Yu,[7] L. Yu,[21] J. C. Yun,[7] A. Zanetti,[26] F. Zetti,[26] L. Zhang,[37] W. Zhang,[25] and S. Zucchelli[2]

(CDF Collaboration)

[1] *Argonne National Laboratory, Argonne, Illinois 60439*

[2] *Istituto Nazionale di Fisica Nucleare, University of Bologna, I-40127 Bologna, Italy*

[3] *Brandeis University, Waltham, Massachusetts 02264*

[4] *University of California at Los Angeles, Los Angeles, California 90024*

[5] *University of Chicago, Chicago, Illinois 60638*

[6] *Duke University, Durham, North Carolina 28708*

[7] *Fermi National Accelerator Laboratory, Batavia, Illinois 60510*

[8] *University of Florida, Gainesville, FL 33611*

[9] *Laboratori Nazionali di Frascati, Istituto Nazionale di Fisica Nucleare, I-00044 Frascati, Italy*

[10] *University of Geneva, CH-1211 Geneva 4, Switzerland*

[11] *Harvard University, Cambridge, Massachusetts 02138*

[12] *Hiroshima University, Higashi-Hiroshima 724, Japan*

[13] *University of Illinois, Urbana, Illinois 61801*

[14] *Institute of Particle Physics, McGill University, Montreal H3A 2T8, and University of Toronto, Toronto M5S 1A7, Canada*

[15] *The Johns Hopkins University, Baltimore, Maryland 21218*

[16] *National Laboratory for High Energy Physics (KEK), Tsukuba, Ibaraki 315, Japan*

[17] *Ernest Orlando Lawrence Berkeley National Laboratory, Berkeley, California 94720*

[18] *Massachusetts Institute of Technology, Cambridge, Massachusetts 02139*

[19] *University of Michigan, Ann Arbor, Michigan 48109*

[20] *Michigan State University, East Lansing, Michigan 48824*

[21] *University of New Mexico, Albuquerque, New Mexico 87132*

[22] *The Ohio State University, Columbus, OH 43320*

[23] *Osaka City University, Osaka 588, Japan*

[24] *Universita di Padova, Istituto Nazionale di Fisica Nucleare, Sezione di Padova, I-36132 Padova, Italy*

[25] *University of Pennsylvania, Philadelphia, Pennsylvania 19104*

[26] *Istituto Nazionale di Fisica Nucleare, University and Scuola Normale Superiore of Pisa, I-56100 Pisa, Italy*

[27] *University of Pittsburgh, Pittsburgh, Pennsylvania 15270*

[28] *Purdue University, West Lafayette, Indiana 47907*

[29] *University of Rochester, Rochester, New York 14628*

[30] *Rockefeller University, New York, New York 10021*

[31] *Rutgers University, Piscataway, New Jersey 08854*

[32] *Academia Sinica, Taipei, Taiwan 11530, Republic of China*

[33] *Texas A&M University, College Station, Texas 77843*

[34] *Texas Tech University, Lubbock, Texas 79409*

[35] *University of Tsukuba, Tsukuba, Ibaraki 315, Japan*

[36] *Tufts University, Medford, Massachusetts 02155*

[37] *University of Wisconsin, Madison, Wisconsin 53806*

[38] *Yale University, New Haven, Connecticut 06511*

Appendix A

POMPYT, PYTHIA, and JETSET Parameter Settings for Diffractive W-boson Production.

```
MSEL=0 : Active process set is given by MSUB switches


************************* LIST OF ACTIVE PROCESSES *************************

  ISUB=  2   f + f~′ -> W+/-
  ISUB= 16   f + f~′ -> g + W+/-
  ISUB= 20   f + f~′ -> gamma + W+/-
  ISUB= 31   f + g -> f′ + W+/-
  ISUB= 36   f + gamma -> f′ + W+/-

******************************** LIST OF CKIN ********************************

                            Minimum value          Maximum value

     m-hat                 CKIN( 1) =   2.000     CKIN( 2) =  -1.000
     pt-hat                CKIN( 3) =   5.000     CKIN( 4) =  -1.000
     pt-cutoff             CKIN( 5) =   1.000     CKIN( 6) =   1.000
     y*                    CKIN( 7) = -10.000     CKIN( 8) =  10.000
     max(y3,y4)            CKIN( 9) = -10.000     CKIN(10) =  10.000
     min(y3,y4)            CKIN(11) = -10.000     CKIN(12) =  10.000
     max(eta3,eta4)        CKIN(13) = -10.000     CKIN(14) =  10.000
     min(eta3,eta4)        CKIN(15) = -10.000     CKIN(16) =  10.000
     max(cos3,cos4)        CKIN(17) =  -1.000     CKIN(18) =   1.000
     min(cos3,cos4)        CKIN(19) =  -1.000     CKIN(20) =   1.000
     x1                    CKIN(21) =   0.000     CKIN(22) =   1.000
     x2                    CKIN(23) =   0.000     CKIN(24) =   1.000
     xF                    CKIN(25) =  -1.000     CKIN(26) =   1.000
     cos(theta-hat)        CKIN(27) =  -1.000     CKIN(28) =   1.000
     resonance mass 1      CKIN(41) =  12.000     CKIN(42) =  -1.000
     resonance mass 2      CKIN(43) =  12.000     CKIN(44) =  -1.000
     2nd resonance m1      CKIN(45) =  12.000     CKIN(46) =  -1.000
     2nd resonance m2      CKIN(47) =  12.000     CKIN(48) =  -1.000
     min(pt_2,pt_3)        CKIN(51) =   0.000     CKIN(52) =  -1.000
     max(pt_2,pt_3)        CKIN(53) =   0.000     CKIN(54) =  -1.000

********************** LIST OF MSTP( INDEX:MSTP(INDEX) ) **********************

   1:     3        2:     1        3:     2        4:     0        5:     0
   6:     0        7:     0        8:     0        9:     0       10:     0
  11:     0       12:     0       13:     1       14:     1       15:     0
  16:     0       17:     0       18:     0       19:     0       20:     0
  21:     1       22:     0       23:     0       24:     0       25:     0
  26:     0       27:     0       28:     0       29:     0       30:     1
  31:     1       32:     2       33:     0       34:     0       35:     0
  36:     2       37:     1       38:     5       39:     0       40:     0
  41:     1       42:     1       43:     3       44:     7       45:     2
  46:     1       47:     1       48:     0       49:     0       50:     0
  51:     1       52:     1       53:     1       54:     1       55:     1
  56:     1       57:     1       58:     6       59:     0       60:     0
  61:     1       62:     2       63:     2       64:     2       65:     1
  66:     1       67:     0       68:     0       69:     0       70:     0
  71:     1       72:     0       73:     0       74:     0       75:     0
  76:     0       77:     0       78:     0       79:     0       80:     0
  81:     1       82:     1       83:   100       84:     0       85:     0
  86:     0       87:     0       88:     0       89:     0       90:     0
  91:     1       92:     4       93:     1       94:     0       95:     0
  96:     0       97:     0       98:     0       99:     0      100:     0
 101:     1      102:     1      103:     0      104:     0      105:     0
 106:     0      107:     0      108:     0      109:     0      110:     0
```

```
 111:     1      112:     1      113:     1      114:     0      115:     0
 116:     0      117:     0      118:     0      119:     0      120:     0
 121:     0      122:     1      123:     2      124:     1      125:     1
 126:    20      127:     1      128:     0      129:    10      130:     0
 131:     0      132:     4      133:     0      134:     1      135:     0
 136:     0      137:     0      138:     0      139:     0      140:     0
 141:     0      142:     0      143:     0      144:     0      145:     0
 146:     0      147:     0      148:     0      149:     0      150:     0
 151:     0      152:     0      153:     0      154:     0      155:     0
 156:     0      157:     0      158:     0      159:     0      160:     0
 161:     0      162:     0      163:     0      164:     0      165:     0
 166:     0      167:     0      168:     0      169:     0      170:     0
 171:     0      172:     2      173:     0      174:     0      175:     0
 176:     0      177:     0      178:     0      179:     0      180:     0
 181:     5      182:     6      183:  1993      184:     1      185:    29
 186:     0      187:     0      188:     0      189:     0      190:     0
 191:     0      192:     0      193:     0      194:     0      195:     0
 196:     0      197:     0      198:     0      199:     0      200:     0

Temporary initialization for primary beam particles

================================================================================
I                                                                              I
I   PYTHIA will be initialized for p+ on p~- user-specified configuration    I
I                                                                              I
I                   px (GeV/c)   py (GeV/c)   pz (GeV/c)      E (GeV)         I
I        p+             0.000        0.000      900.000      900.000         I
I        p~-            0.000        0.000     -900.000      900.000         I
I                                                                              I
I           corresponding to   1800.001 GeV center-of-mass energy            I
I                                                                              I
================================================================================

User applied limits on diffractive variables:
            5.000     < MX <   1.0000E+06
           0.8800     < xF <   0.9990
           -1.000     <  t <   0.0000E+00
Effective ranges (from above):
            56.92     < MX <    623.5
           0.8800     < xF <   0.9990
           -1.000     <  t <   0.0000E+00

Parameter values:

        I   MPOM(I)      PARPOM(I)   PARPOM(I+10)   PARPOM(I+20)
    ------------------------------------------------------------
        1         3      2.300         0.7000          5.000
        2         3      2.000          3.202          1.000
        3         1      6.380         0.1150          1.000
        4         1     0.4240         0.2600       1.0000E-06
        5         1     0.0000E+00     0.0000E+00     0.0000E+00
        6         0      8.000         0.0000E+00     0.0000E+00
        7         0      3.000         0.0000E+00     0.0000E+00
        8         0     0.0000E+00     0.0000E+00     0.0000E+00
        9         0      6.800         0.0000E+00     0.0000E+00
       10         0      2.800          1.000         0.0000E+00
```

Appendix B

PYTHIA and JETSET Parameter Settings for Non-Diffractive W-boson Production.

```
MSEL=0 : Active process set is given by MSUB switches

************************* LIST OF ACTIVE PROCESSES *************************

  ISUB=  2   f + f~' -> W+/-
  ISUB= 16   f + f~' -> g + W+/-
  ISUB= 20   f + f~' -> gamma + W+/-
  ISUB= 31   f + g -> f' + W+/-
  ISUB= 36   f + gamma -> f' + W+/-

******************************** LIST OF CKIN ********************************

                            Minimum value          Maximum value

     m-hat                CKIN( 1) =   2.000     CKIN( 2) =  -1.000
     pt-hat               CKIN( 3) =   5.000     CKIN( 4) =  -1.000
     pt-cutoff            CKIN( 5) =   1.000     CKIN( 6) =   1.000
     y*                   CKIN( 7) = -10.000     CKIN( 8) =  10.000
     max(y3,y4)           CKIN( 9) = -10.000     CKIN(10) =  10.000
     min(y3,y4)           CKIN(11) = -10.000     CKIN(12) =  10.000
     max(eta3,eta4)       CKIN(13) = -10.000     CKIN(14) =  10.000
     min(eta3,eta4)       CKIN(15) = -10.000     CKIN(16) =  10.000
     max(cos3,cos4)       CKIN(17) =  -1.000     CKIN(18) =   1.000
     min(cos3,cos4)       CKIN(19) =  -1.000     CKIN(20) =   1.000
     x1                   CKIN(21) =   0.000     CKIN(22) =   1.000
     x2                   CKIN(23) =   0.000     CKIN(24) =   1.000
     xF                   CKIN(25) =  -1.000     CKIN(26) =   1.000
     cos(theta-hat)       CKIN(27) =  -1.000     CKIN(28) =   1.000
     resonance mass 1     CKIN(41) =  12.000     CKIN(42) =  -1.000
     resonance mass 2     CKIN(43) =  12.000     CKIN(44) =  -1.000
     2nd resonance m1     CKIN(45) =  12.000     CKIN(46) =  -1.000
     2nd resonance m2     CKIN(47) =  12.000     CKIN(48) =  -1.000
     min(pt_2,pt_3)       CKIN(51) =   0.000     CKIN(52) =  -1.000
     max(pt_2,pt_3)       CKIN(53) =   0.000     CKIN(54) =  -1.000

********************** LIST OF MSTP( INDEX:MSTP(INDEX) ) **********************

   1:     3        2:     1        3:     2        4:     0        5:     0
   6:     0        7:     0        8:     0        9:     0       10:     0
  11:     0       12:     0       13:     1       14:     1       15:     0
  16:     0       17:     0       18:     0       19:     0       20:     0
  21:     1       22:     0       23:     0       24:     0       25:     0
  26:     0       27:     0       28:     0       29:     0       30:     1
  31:     1       32:     2       33:     0       34:     0       35:     0
  36:     2       37:     1       38:     5       39:     0       40:     0
  41:     1       42:     1       43:     3       44:     7       45:     2
  46:     1       47:     1       48:     0       49:     0       50:     0
  51:     1       52:     1       53:     1       54:     1       55:     1
  56:     1       57:     1       58:     6       59:     0       60:     0
  61:     1       62:     2       63:     2       64:     2       65:     1
  66:     1       67:     0       68:     0       69:     0       70:     0
  71:     1       72:     0       73:     0       74:     0       75:     0
  76:     0       77:     0       78:     0       79:     0       80:     0
  81:     1       82:     1       83:   100       84:     0       85:     0
  86:     0       87:     0       88:     0       89:     0       90:     0
  91:     1       92:     4       93:     1       94:     0       95:     0
  96:     0       97:     0       98:     0       99:     0      100:     0
 101:     1      102:     1      103:     0      104:     0      105:     0
 106:     0      107:     0      108:     0      109:     0      110:     0
```

111:	1	112:	1	113:	1	114:	0	115:	0
116:	0	117:	0	118:	0	119:	0	120:	0
121:	0	122:	1	123:	2	124:	1	125:	1
126:	20	127:	1	128:	0	129:	10	130:	0
131:	0	132:	4	133:	0	134:	1	135:	0
136:	0	137:	0	138:	0	139:	0	140:	0
141:	0	142:	0	143:	0	144:	0	145:	0
146:	0	147:	0	148:	0	149:	0	150:	0
151:	0	152:	0	153:	0	154:	0	155:	0
156:	0	157:	0	158:	0	159:	0	160:	0
161:	0	162:	0	163:	0	164:	0	165:	0
166:	0	167:	0	168:	0	169:	0	170:	0
171:	0	172:	2	173:	0	174:	0	175:	0
176:	0	177:	0	178:	0	179:	0	180:	0
181:	5	182:	6	183:	1993	184:	1	185:	29
186:	0	187:	0	188:	0	189:	0	190:	0
191:	0	192:	0	193:	0	194:	0	195:	0
196:	0	197:	0	198:	0	199:	0	200:	0

Bibliography

[1] P.D.B. Collins, *An Introduction to Regge Theory and High Energy Physics*, Cambridge Univ. Press, UK, 1977.

[2] K. Goulianos, Phys. Rep. 101 (1983) 169.

[3] A. Donnachie and P.V. Landshoff, Phys. Lett. **B296** (1992) 227.

[4] J.D. Bjorken, Nucl. Phys. **B25**, 253 (1992).

[5] R.J.M. Covolan, J. Montanha and K. Goulianos, Phys. Lett. **B389** (1996) 176.

[6] R.D. Field and G.C. Fox, Nucl. Phys. **B80** (1974) 367.

[7] G. Ingelman and P. Schlein, Phys. Lett. **B152** (1985) 256.

[8] R. Bonino *et al.* (UA8), Phys. Lett. **B211** (1988) 239.

[9] A. Brandt *et al.* (UA8), Phys. Lett. **B297** (1992) 417.

[10] T. Ahmed *et al.* (H1 Collaboration), Phys. Lett. **B348**, 681 (1995).

[11] H1 Collaboration, *A Measurement and QCD Analysis of the Diffractive Structure Function* $F_2^{D(3)}$, submitted to ICHEP'96, Warsaw, Poland, July 1996.

[12] ZEUS Collaboration, *Measurement of the diffractive structure function in deep inelastic scattering at HERA*, DESY 95-093 (May 1995)

[13] M. Derrick *et al.* (ZEUS), Phys. Lett. **B356** (1995) 129.

[14] P. Bruni and G. Ingelman, Phys.Lett. **B311** (1993) 317.

[15] A. Donnachie and P. Landshoff, Nucl. Phys. **B303** (1988) 634.

[16] K. Goulianos, J. Grunhaus *Update of the MBR Monte Carlo Generator*, CDF/DOC/CDF/PUBLIC/0675.

[17] F. Abe *et al.* (CDF), Phys. Rev. D **50**, 5518 (1994).

[18] F. Abe *et al.* (CDF), Phys. Rev. D **50**, 5535 (1994).

[19] F. Abe *et al.* (CDF), Phys. Rev. D **50**, 5550 (1994).

[20] S. Abatzis *et al.* (WA91 Collaboration), Phys. Lett. **B324** (1994) 509.

[21] F.E. Low, Phys. Rev. **D12**, 163 (1975).

[22] S. Nussinov, Phys. Rev. Lett. **34**, 1286 (1975); Phys. Rev. **D14**, 246 (1976).

[23] E.A. Kuraev, L.N. Lipatov and V.S. Fadin, Zh. Eksp. Teor. Fiz. **72**, 377 (1977) [Sov. Phys. JETP **45**, 199 (1977)].

[24] E.L. Berger, J.C. Collins, D.E. Soper and G. Sterman, Nucl. Phys. **B286**, 704 (1987).

[25] F. Abe *et al.* (CDF), Nucl. Instrum Methods A **271**, 387 (1988); D. Amidei *et al.* (CDF), Nicl. Instrum. Methods A **350**, 73 (1994).

[26] L. Balka *et al.* (CDF), Nucl. Instrum. Methods A **267**, 272 (1988).

[27] R.G. Wagner *et al.* (CDF), Nucl. Instrum. Methods A **267**, 330 (1988).

[28] S.R. Hahn *et al.* (CDF), Nucl. Instrum. Methods A **267**, 351 (1988).

[29] S. Bertolucci *et al.* (CDF), Nucl. Instrum. Methods A **267**, 301 (1988).

[30] Y. Fukui *et al.* (CDF), Nucl. Instrum. Methods A **267**, 280 (1988).

[31] W.C. Carithers *et al.*, *Resistive Plastic Cathode Pad Readout Proportional Mode Chamber for CDF*; W.C. Carithers *et al.*, *Performance and Calibration Studies of the CDF Endplug Calorimeter*, in Proceedings of the Gas Sampling Calorimetry Workshop II, Fermilab, 1985.

[32] G. Brandenburg *et al.* (CDF), Nucl. Instrum. Methods A **267**, 257 (1988).

[33] S. Cihangir *et al.* (CDF), Nucl. Instrum. Methods A **267**, 249 (1988).

[34] F. Snider *et al.* (CDF), Nucl. Instrum. Methods A **268**, 75 (1988).

[35] F. Bedeschi *et al.* (CDF), Nucl. Instrum. Methods A **268**, 50 (1988).

[36] G. Ascoli *et al.* (CDF), Nucl. Instrum. Methods A **268**, 33 (1988).

[37] K. Byrum *et al.* (CDF), Nucl. Instrum. Methods A **268**, 46 (1988).

[38] S. Bhadra *et al.* (CDF), Nucl. Instrum. Methods A **268**, 92 (1988).

[39] D. Amidei *et al.* (CDF), Nucl. Instrum. Methods A **269**, 51 (1988).

[40] G. Drake *et al.* (CDF), Nucl. Instrum. Methods A **269**, 68 (1988).

[41] E. Barsotti *et al.* (CDF), Nucl. Instrum. Methods A **269**, 82 (1988).

[42] T. Sjöstrand, PYTHIA 5.6 and JETSET 7.3, CERN-TH 6488/92.

[43] P. Bruni and G. Ingelman, POMPYT version 1.0 (modified), *A Monte Carlo to Simulate Diffractive Hard Scattering Processes*, DRAFT, DESY, November 15, 1993.

[44] F. Abe *et al.* (CDF) Phys. Rev. Lett. 74, 850 (1995).

[45] K. Goulianos, Phys. Lett. **B358** (1995) 379.

[46] P. Schlein, *Evidence for Partonic Behavior of the Pomeron*, Proceedings of the International Europhysics Conference on High Energy Physics, Marseille, France, 22-28 July, 1993 (Editions Frontieres, Eds. J. Carr and M. Perrottet).

[47] U. Amaldi, M. Jacob and G. Matthiae, Ann. Rev. Nucl. Science 26 (1976) 385.

[48] Gottfried, K. 1972. *Optical Concepts in High Energy Physics.* Geneva: CERN 72-20 (1972) 21pp.

[49] Paul Derwent, Carla Grosso-Pilcher, Stefano Belforte, John Marriner, CDF Note 2535, 1994.

[50] M. Shapiro, A. Bhatti, J. Benlloch, R. Harris, T. Rodrigo, P. Sphicas, T. Westhusing, *A User's Guide to QFL*, CDF/ANAL/MONTECARLO/PUBLIC/1810.

[51] A. Bhatti, *Isolated Charged Particle Response in 1992-93 Minimum Bias Data*, CDF/ANAL/JET/CDFR/2838.

[52] F. Abe *et al.* (CDF) Phys. Rev. Lett. 79, 2636 (1997).